

A homogeneous spectroscopic analysis of a *Kepler* legacy sample of dwarfs for gravity-mode asteroseismology

Sarah Gebruers^{1,2}, Ilya Straumit^{1,3}, Andrew Tkachenko¹, Joey S. G. Mombarg¹, May G. Pedersen^{1,4}, Timothy Van Reeth¹, Gang Li^{5,6}, Patricia Lampens⁷, Ana Escorza^{1,8}, Dominic M. Bowman¹, Peter De Cat⁷, Lore Vermeyleen⁷, Julia Bodensteiner¹, Hans-Walter Rix², and Conny Aerts^{1,2,9}

¹ Institute of Astronomy, KU Leuven, Celestijnenlaan 200D, 3001 Leuven, Belgium
e-mail: sarah.gebruers@kuleuven.be

² Max Planck Institute for Astronomy, Königstuhl 17, 69117 Heidelberg, Germany

³ Department of Astronomy, The Ohio State University, Columbus, OH 43210, USA

⁴ Kavli Institute for Theoretical Physics, University of California, Santa Barbara, CA 93106, USA

⁵ Sydney Institute for Astronomy (SfA), School of Physics, University of Sydney, NSW 2006, Australia

⁶ Stellar Astrophysics Centre, Department of Physics and Astronomy, Aarhus University, Ny Munkegade 120, 8000 Aarhus C, Denmark

⁷ Koninklijke Sterrenwacht van België, Ringlaan 3, 1180 Brussel, Belgium

⁸ European Southern Observatory, Alonso de Córdova 3107, Vitacura, Casilla 19001, Santiago, Chile

⁹ Department of Astrophysics, IMAPP, Radboud University Nijmegen, PO Box 9010, 6500 GL Nijmegen, The Netherlands

Received 1 February 2021 / Accepted 8 April 2021

ABSTRACT

Context. Asteroseismic modelling of the internal structure of main-sequence stars born with a convective core has so far been based on homogeneous analyses of space photometric *Kepler* light curves of four years in duration, to which most often incomplete inhomogeneously-deduced spectroscopic information was added to break degeneracies.

Aims. Our goal is twofold: (1) to compose an optimal sample of gravity-mode pulsators observed by the *Kepler* space telescope for joint asteroseismic and spectroscopic stellar modelling, and (2) to provide spectroscopic parameters for its members, deduced in a homogeneous way.

Methods. We assembled HERMES high-resolution optical spectroscopy at the 1.2 m Mercator telescope for 111 dwarfs, whose *Kepler* light curves allowed for the determination of their near-core rotation rates. Our spectroscopic information offers additional observational input to also model the envelope layers of these non-radially pulsating dwarfs.

Results. We determined stellar parameters and surface abundances from atmospheric analysis with spectrum normalisation based on a new machine-learning tool. Our results suggest a systematic overestimation of metallicity ([M/H]) in the literature for the studied F-type dwarfs, presumably due to normalisation limitations caused by the dense line spectrum of these rotating stars. CNO surface abundances were found to be uncorrelated with the rotation properties of the F-type stars. For the B-type stars, we find a hint of deep mixing from C and O abundance ratios; N abundance uncertainties are too great to reveal a correlation of N with the rotation of the stars.

Conclusions. Our spectroscopic stellar parameters and abundance determinations allow for the future joint spectroscopic, astrometric (*Gaia*), and asteroseismic modelling of this legacy sample of gravity-mode pulsators, with the aim of improving our understanding of transport processes in the core-hydrogen burning phase of stellar evolution.

Key words. asteroseismology – stars: variables: general – stars: oscillations – stars: fundamental parameters – stars: abundances – techniques: spectroscopic

1. Introduction

Space asteroseismology has made stellar interiors accessible for observational investigation across stellar evolution. Its current status is broadly summarised in various review papers, to which we refer the reader for a wealth of information (Hekker & Christensen-Dalsgaard 2017; García & Ballot 2019; Corsico et al. 2019; Bowman 2020; Aerts 2021). As highlighted in these reviews, most focus of asteroseismic modelling has so far been put on low-mass main-sequence stars and stellar remnants across the Hertzsprung-Russell diagram (HRD), because these types of stars were predominantly observed by time-series photometric space telescopes. Moreover, the internal structure of low-mass main-sequence stars resembles that of the Sun,

implying that their pulsation mode excitation is the same. It concerns stochastic excitation of pressure (p) modes in the extensive convective envelopes of these stars. Low-mass stars are slow rotators due to magnetic braking, such that the Coriolis and centrifugal forces are typically negligible as restoring forces for asteroseismology. Hence, the basic diagnostic observables and modelling techniques developed in the context of helioseismology (Christensen-Dalsgaard 2002) could easily be transformed for the stellar modelling of large samples of low-mass pulsators. In addition to the space photometry, spectroscopy was also used to deliver the effective temperature and metallicity as constraints (e.g. Lebreton & Goupil 2014; Mazumdar et al. 2014; Silva Aguirre et al. 2017; Bellinger 2019, 2020; Verma et al. 2019; Angelou et al. 2020).

The possibilities of gravity-mode (g -mode hereafter) asteroseismology of dwarf stars only became apparent after the first detection of period spacing patterns in B-type pulsators observed with the CoRoT space mission (Auvergne et al. 2009) about a decade ago (Degroote et al. 2010; Pápics et al. 2012; Neiner et al. 2012). While the CoRoT mission was a pioneer to show the potential of this branch of asteroseismology, it took until the release of the four-year *Kepler* light curves for the g -mode asteroseismic modelling to see its first light. Indeed, the frequency precision of the modes scales as the inverse of the total time base of the light curve (see e.g. Montgomery & O'Donoghue 1999) and this has to be of the order of years to achieve sufficient g -mode probing power in order to evaluate the theory of stellar interiors (e.g. Aerts et al. 2018).

The initial studies of stellar modelling based on *Kepler* g -mode asteroseismology were done for individual targets belonging to the two classes of g -mode pulsators: the late-A- to early-F-type dwarfs called γ Doradus (γ Dor) stars (Kurtz et al. 2014; Saio et al. 2015; Murphy et al. 2016; Ouazzani et al. 2017) and the slowly pulsating B (SPB) stars (Moravveji et al. 2015, 2016; Szewczuk & Daszyńska-Daszkiewicz 2018; Wu & Li 2019; Wu et al. 2020). These pulsators all have a convective core and reveal high-radial-order low-degree g modes excited by the flux blocking mechanism for γ Dor stars with a thin convective envelope (Guzik et al. 2000; Dupret et al. 2005), and by the heat-engine mechanism acting in the iron–nickel opacity bump for SPB stars with a radiative envelope (Dziembowski et al. 1993; Szewczuk & Daszyńska-Daszkiewicz 2017). The γ Dor stars have masses between 1.3 and 1.9 M_{\odot} and effective temperatures between 6700 and 7900 K, while the dwarf SPB stars cover the mass range from 3 to 9 M_{\odot} and have effective temperatures between 11 000 and 22 000 K (see Chap. 3, Aerts et al. 2010, for a general review of their properties). Both these types of g -mode pulsators show non-radial g modes with pulsation periods from 0.5 to about 5 days and amplitudes below 15 mmag. Nominal four-year *Kepler* light curves of these stars have allowed for the detection of tens of g modes with amplitudes below 1 mmag, several of which are members of g -mode period spacing patterns. Such patterns are critical observables as they allow us to achieve mode identification, which is a prerequisite for asteroseismic modelling (Aerts 2021).

Dwarfs with g -mode pulsations cover the entire range of rotational velocities between zero and the critical break-up velocity, due to the absence of a convective dynamo and magnetic braking. Their high-radial-order g modes have low frequencies and eigenfunctions with dominant horizontal vector components (cf. Aerts 2021, for a general review). Thanks to these properties, the g modes are well described by the traditional approximation of rotation (TAR), which takes the Coriolis acceleration into account in the equation of motion, while ignoring the vertical component of the rotation vector (Lee & Saio 1987; Townsend 2003; Mathis 2009). In fact, the Coriolis acceleration plays a key role in the modelling of the detected g modes because almost all of them occur in the gravito-inertial regime (Aerts et al. 2017). This implies that the stellar rotation throughout the star is a key ingredient of g -mode asteroseismology of dwarfs. Assessment of the internal structure of those stars in terms of angular momentum and chemical element transport must thus come from ensemble studies covering the entire range of rotation rates and treating the rotational properties as dominant unknowns in the modelling process (Aerts et al. 2019). This makes g -mode asteroseismology considerably more challenging than that of the slowly rotating solar-like p -mode pulsators (García & Ballot 2019). Particularly, g -mode asteroseismology

is subject to strong correlations among the properties of the convective core, convective boundary mixing, and the rotational and pulsational behaviour in the radiative envelope. Moreover, uncertainties for the theoretical predictions occur, as the Sun cannot be used as a calibrator for the most important physical ingredients of the models. While Aerts et al. (2018) developed a method to take these uncertainties and correlations into account in asteroseismic modelling, the addition of spectroscopic information helps to break degeneracies.

Few ensemble studies with g -mode asteroseismology of γ Dor and SPB stars are available. So far, three such studies have been done, covering 37 γ Dor stars and 26 SPB stars (Van Reeth et al. 2016; Mombarg et al. 2019; Pedersen et al. 2021). For none of them surface abundances and surface rotation rates have been included as inputs in the stellar modelling, due to lack of this information or the in-homogeneous treatments to derive those quantities in the literature. Pedersen et al. (2018) showed the potential of adding the surface N abundance for the assessment of mixing in the radiative envelope of SPB stars. These authors found that a combination of g -mode asteroseismology and high-precision spectroscopic measurements of the atmospheric parameters and surface chemical composition offers a powerful route to calibrating stellar interiors in terms of element transport processes. Moreover, Mombarg et al. (2020) investigated the occurrence of microscopic atomic diffusion, including radiative levitation, from g -mode pulsations in two F-type stars. In this study, the spectroscopic effective temperature, surface gravity, and surface abundances were used as extra constraints aside from the g modes in the modelling of two slowly rotating γ Dor pulsators. The authors found strong evidence for signatures of radiative levitation for one of the stars, but not in the other one.

Clearly, a systematic homogeneous spectroscopic analysis of g -mode pulsating dwarfs selected based on their asteroseismic potential would be highly beneficial for the ensemble asteroseismic modelling of these stars. This would allow us to maximally exploit the power of the g modes to probe the deep stellar interior and of the surface abundances to assess the mixing profiles in the radiative envelope. With the exception of Tkachenko et al. (2013), Pápics et al. (2017), and Pedersen et al. (2021), spectroscopic studies of g -mode pulsators were done prior to the availability of any asteroseismic modelling results and only used the brightness of the pulsators or the availability of detected frequencies as selection criteria to compose the samples (e.g. Lehmann et al. 2011; Tkachenko et al. 2012; Niemczura et al. 2015, 2017; Lampens et al. 2018). All these previous studies showed that γ Dor and SPB stars have spectroscopic properties that are not different from those of non-pulsators of the same spectral type. Here, we took a different approach in which we first selected the most promising g -mode pulsators from the point of view of asteroseismic modelling capacity. We focused on g -mode pulsators whose internal rotation frequency (Ω_{core}) was estimated from period spacing patterns thanks to identified g modes of consecutive radial order deduced from the *Kepler* light curves (Van Reeth et al. 2016; Pápics et al. 2017; Li et al. 2020; Pedersen et al. 2021).

For this carefully selected legacy sample of intermediate-mass stars with g -mode pulsations, we added homogeneously analysed high-resolution spectroscopy as complementary information to space photometry to aid future asteroseismic ensemble modelling of *Kepler* g -mode pulsators. We did so by using high-resolution spectroscopy from one optimally suited spectrograph (HERMES, Raskin et al. 2011) and by analysing it using a machine-learning approach. The spectra were analysed with

The Payne (Ting et al. 2019), a spectrum interpolator based upon a neural network that is able to predict stellar parameters of a given spectrum, and that was adapted to also include continuum normalisation. Its advantage is that spectra can be processed fast and homogeneously, which is important for both this work and (future) samples from large spectroscopic surveys. In addition to spectroscopy, *Gaia* distances were considered to provide constraints on the luminosity of the stars. Here we improved estimation of the luminosity from eDR3, while Pedersen et al. (2020) and Li et al. (2020) relied on DR2. We present our results for a *Kepler* asteroseismic legacy sample of *g*-mode pulsators. As discussed in the next section, it consists of 91 γ Dor and 20 SPB *Kepler* stars.

In Sect. 2, we define the sample and describe the available observational data and their reduction process. Section 3 is dedicated to the atmospheric analysis. It also includes a few tests for a new machine-learning technique for stellar parameter determination. The stellar parameters and surface abundances for all stars in the sample are given in Sect. 4 together with a literature comparison. The results are placed in a physical context in Sect. 5, and we conclude in Sect. 6.

2. Sample selection and spectroscopic observations

We searched for an optimal sample of *g*-mode pulsators, defined as stars with period spacing patterns composed of modes with consecutive radial order and identified spherical degree and azimuthal order. Moreover, our selection required the availability of an asteroseismic estimate of the near-core rotation frequency Ω_{core} . For *g*-mode pulsators meeting these two stringent selection criteria, we aim to determine their spectroscopic stellar parameters (effective temperature (T_{eff}), surface gravity ($\log g$), metallicity ($[M/H]$), projected rotational velocity ($v \sin i$), and microturbulent velocity (ξ)) and individual surface abundances in a homogeneous way for the whole selected sample. As a result, future combined spectroscopic-asteroseismic modelling will make it possible to investigate whether the addition of spectroscopic parameters for the whole ensemble improves the current state-of-the-art asteroseismic modelling. We focused on γ Dor and SPB stars with *Gaia* luminosities and published *Kepler* period spacing patterns and Ω_{core} values by Van Reeth et al. (2016), Li et al. (2020), and Pedersen et al. (2020, 2021). All of these *g*-mode pulsators were detected from four-year *Kepler* light curves. The first two studies concern some 650 γ Dor stars, 37 of which also have asteroseismic masses, ages, and core properties from ensemble modelling by Mombarg et al. (2019). The study of Pedersen et al. (2020) concerns 32 SPB pulsators for which period spacing patterns have been detected. Twenty-six of them were asteroseismically modelled, including the estimation of convective boundary mixing as well as envelope mixing.

Out of these nearly 700 *g*-mode pulsators with asteroseismic parameters available in the literature, we distilled a *g*-mode legacy sample. We selected stars for which high-resolution spectroscopic observations were subsequently assembled with intermediate to high signal-to-noise ratios ($S/N \geq 20$), allowing for a homogeneous analysis and study of the atmospheric properties of the sample stars. For this reason, we focused on spectroscopic data taken exclusively with the HERMES échelle spectrograph (Raskin et al. 2011) mounted on the 1.2 m Mercator telescope at Observatorio del Roque de los Muchachos (La Palma, Canary Islands, Spain). HERMES combines two important characteristics for our aim, namely high spectral resolution

($R \sim 85\,000$) and full coverage of the optical wavelength range from 377 to 900 nm. With the above requirements, we ended up with a total of 127 *g*-mode pulsators in our sample, including spectroscopic binaries (see Sect. 3.1 for the final sample of 111 stars, which only consists of single stars and single-lined binaries). Of these, 104 are γ Dor stars taken from Li et al. (2020) including 40 that overlap with Van Reeth et al. (2016), and 23 SPB stars that were studied by Pedersen et al. (2020). An overview of the spectroscopic observations and the S/N values of the combined exposures of each target is given in Tables A.1 and A.2 for the γ Dor and SPB stars, respectively.

The spectra were reduced with version 7.0 of the HERMES reduction pipeline, which includes bias subtraction, cosmic ray removal, wavelength calibration, barycentric correction, order merging, and flat field correction. Every spectrum was also subjected to additional outlier rejection, meaning that cosmic ray hits were removed. For this step, we compared the local flux at every point in the spectrum to the median flux within a surrounding window of 50 pixels ($\sim 1.5 \text{ \AA}$) for γ Dor stars or 100 pixels ($\sim 3 \text{ \AA}$) for SPB stars, where we took a smaller window for the γ Dor stars because these spectra contain many more spectral lines. If the difference between the local and median flux was higher than four times the standard deviation within this window, we replaced the local flux with the median value.

3. Atmospheric analysis

The atmospheric analysis was split into two parts. We used a machine-learning framework, The Payne (Ting et al. 2019, see Sect. 3.2), to determine stellar parameters while the surface abundances were obtained with the spectrum analysis code called Grid Search in Stellar Parameters (GSSP, Tkachenko 2015). Both the stellar parameters and surface abundances are computed using local thermodynamic equilibrium (LTE) models. For the atmospheric analysis and tests described in this section, we considered the wavelength range between 4200 and 5800 \AA , unless stated otherwise. This includes two Balmer lines and a region of metal lines.

3.1. Radial velocity signal-based classification

We started with the classification of our sample of stars according to the radial velocity (RV) information present in their spectra. We computed a discrete 1D cross-correlation function (CCF, Tonry & Davis 1979) where the observed spectrum, preliminary pseudo-normalised by convolution with a Gaussian kernel, is superimposed on a list of delta functions (also termed line mask) and on a grid of RV values, resulting in a correlation function between the observations and the line mask. A line mask represents a set of (typical) atomic lines at their laboratory wavelength's reference frame, and the corresponding line depths predicted from spectral synthesis. In our case, several of those line masks were computed with the GSSP software package (Tkachenko 2015, discussed further in Sects. 3.2.1 and 3.3). We computed such masks for a range of T_{eff} (6500–8000 K with a step of 500 K for γ Dor stars and 10 000–20 000 K with a step of 2000 K for SPB stars), $\log g$ (3.0–5.0 dex with a step of 0.5 dex) and $[M/H]$ (−0.8 to +0.8 dex with a step of 0.2 dex). For each star, the line mask closest to its atmospheric parameters found in the literature was chosen or, when no literature data were available, we used the line mask for a T_{eff} of 7000 K and 16 000 K for γ Dor and SPB stars, respectively, $\log g$ of 4.0 dex, and solar metallicity as the default values. The corresponding cross-correlation

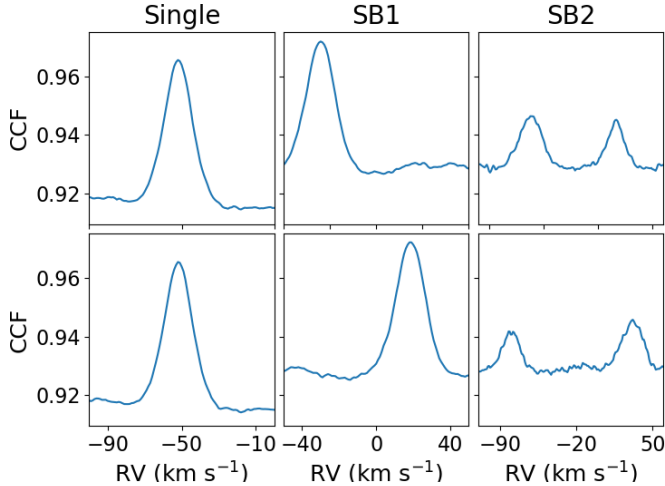


Fig. 1. From left to right: CCFs for a single star (KIC 9751996), a single-lined binary (KIC 6292398) and a double-lined binary (KIC 10080943). Top and bottom rows show CCFs taken at two different observational epochs.

function was obtained for each spectrum of the star separately. The number of spectra for each star are given in the second column of Tables A.1 and A.2.

The CCFs were subject to both visual inspection and inference of RVs, which allowed us to classify stars into three main categories: (1) single stars; (2) spectroscopic single-lined binaries (SB1); and (3) spectroscopic double- (SB2), triple-lined (SB3), or higher-order multiple systems. The last class can be separated from the other two based on a visual inspection of the CCFs, as demonstrated in Fig. 1, provided both (or all) components are of a similar spectral type. Distinguishing between single stars and SB1 systems requires establishing a threshold beyond which RV variations are considered significant, hence pointing to an SB1 binary nature. We computed RVs by fitting a Gaussian to the upper half of the CCF. The maximum of the best-fitting Gaussian gave a first estimate of the RV. By shifting the Gaussian on a RV grid covering the range $\pm 50 \text{ km s}^{-1}$ around this RV value and calculating the χ^2 for each perturbed Gaussian, we obtained a χ^2 distribution. For each spectrum, we took the value with minimal χ^2 as RV and the $3\sigma\chi^2$ level of the distribution as its uncertainty. The detected RV variations were considered as significant whenever the RV difference between two or more spectra exceeded the RV uncertainty. The uncertainty depends on the S/N of the spectrum and the projected rotational velocity. This is because lower S/N spectra or higher velocities broaden the CCF profile, resulting in larger uncertainties. Thus the effect of rotation on the RV accuracy is implicitly taken into account. Gravity-mode pulsations might also distort the wings of line profiles, but our method of RV determination is not sensitive to these changes.

We find that ten of the γ Dor stars are SB2 or possibly higher-order binary systems, 12 stars are SB1s, and the remaining ones are single stars or undetected systems. The RVs are given in the last column of Table A.1, where binaries are indicated appropriately according to their type. Most of the SPBs are single stars, except for two SB2s and one SB1. This is surprising since the binary fraction of OB-type stars in the Milky Way is found to be 0.3–0.5 (Kobulnicky et al. 2014). It is possible that RV variations of some systems are below our detection limit. Many of the SPB spectra have low S/N values, which led to high RV uncertainties. There might also be a selection bias since Pedersen et al.

(2020) excluded potential SPB stars from their sample if they showed periodicities in their light curves matching binary signatures or rotational modulation. For two SPB stars there is only one epoch available, so they are currently treated as single stars. The RVs or binarity information of the SPB sample can be found in Table A.2. Most of the γ Dor and SPB binaries were already identified as such in the literature and corresponding references are included in Tables A.1 and A.2.

The SB2 binaries, including possible higher order multiple systems, were removed from the sample because they require the use of disentangling methods or a combined analysis of the components. We shifted all the spectra to zero RV, and for stars with multiple spectra we added the exposures to obtain a spectrum with a higher S/N value. For four targets, KIC 5254203, KIC 7746984, KIC 9533489, and KIC 9715425, the S/N is too low ($S/N < 20$) for any atmospheric analysis and they were also excluded from the sample. This left us with 111 stars in total (91 γ Dor and 20 SPB pulsators).

3.2. Stellar parameters

The Payne is a machine-learning method that allows for the simultaneous determination of various stellar properties, such as atmospheric parameters and surface abundances, from an observed spectrum (Ting et al. 2019). It uses a neural network (NN) trained on a few thousand model spectra to create a spectral interpolator that can predict a spectrum and its stellar parameters in multi-dimensional space. It can be used to fit an observed spectrum and derive the corresponding parameters. In this work, we use a modified version of the original The Payne algorithm. A brief summary of the modifications is provided in Sect. 3.2.2, while a detailed description is given in Straumit et al. (in prep.) (cf. short description in this paper).

3.2.1. Training sample

A training sample can consist of synthetic-model (e.g. Kovalev et al. 2019) or observed spectra (e.g. Ness et al. 2015; Xiang et al. 2019). Both approaches have their advantages and disadvantages. A data-driven training set contains realistic spectra with noise, but it is restricted to the spectra that are available and the accuracy of their determined parameters. On the other hand, the atmospheric structure and radiative transfer of synthetic spectra are consistently computed and these spectra can cover large parameter ranges. Both approaches are used to derive atmospheric parameters and surface abundances by relying on atmosphere models with specific input physics. The latter can have a variety of approximations, such as 1D versus 3D geometry, an LTE versus non-LTE approximation, a static versus dynamical atmosphere, or a time-dependent versus time-independent treatment of convection.

Since there are not enough B- and F-type stars with accurate stellar parameters deduced from HERMES spectra in a homogeneous way available, we trained NNs with grids of synthetic spectra computed with GSSP. This is an LTE spectrum analysis software package that adopts the SynthV radiative transfer code (Tsymbal 1996) for calculation of synthetic spectra based on a grid of plane-parallel atmosphere models pre-computed with the LLmodels code (Shulyak et al. 2004). The γ Dor and SPB stars require two separate training grids because they span different temperature regimes. We created grids in five dimensions including the most important stellar parameters: T_{eff} , $\log g$, $[M/H]$, $v \sin i$, and ξ . Since our modified version of The Payne code is also aimed for general use, it is impractical to compute

Table 1. Parameter ranges of the training grids.

Parameter	γ Dor	SPB
T_{eff} (K)	6000–10 000	10 000–25 000
$\log g$ (dex)	3–5	3–5
[M/H] (dex)	−0.8–0.8	−0.8–0.8
$v \sin i$ (km s ^{−1})	0–200	0–400
ξ (km s ^{−1})	0–5	2–20

large, computationally expensive grids of synthetic spectra each time the NN needs to be re-trained. Instead, we implement a quasi-random grid, which has the advantage of covering a whole parameter space with fairly few points, while it still has some structure as opposed to a fully random grid that leads to clustering of points (cf. Fig. 14 in Bellinger et al. 2016). The individual synthetic spectra were obtained by generating 5D quasi-random numbers between zero and one using Sobol numbers (Sobol 1967) and mapping the parameter ranges defined in Table 1 onto these Sobol numbers. For each of these quasi-random points, a small grid of 2^5 (=32) models surrounding the grid point was computed with GSSP and linearly interpolated to get the synthetic spectrum at that point.

We tested how large the training sets for γ Dor and SPB stars should be for the NN to predict spectra with sufficient precision. In previous studies, The Payne was mostly used for the analysis of low-resolution (LAMOST) spectra (e.g. Xiang et al. 2019), where the relatively small number of some 1000 training spectra in >10D space proved sufficient because of the limited resolving power in metal line regions. For high-resolution HERMES spectra, however, the NN must be able to handle slowly rotating stars and resolve their many narrow spectral lines. The training sample should therefore be dense enough to differentiate between spectra with quasi-similar parameters. We trained multiple NNs, each with a training sample of different size. For the γ Dor stars, the NNs were trained for grids with 100, 200, 300, 500, 1000, 2000, and 3000 spectra and for SPB stars with 500, 1000, 2500, 4000, 5000, and 7000 spectra. We let each of these NNs predict spectra for certain stellar parameter values and compared them to synthetic spectra computed with GSSP for the same parameters. Comparison was done by means of a merit function based on the sum of the squared differences between the NN-predicted and GSSP-computed spectra, namely $\sum (\text{flux}_{\text{NN}} - \text{flux}_{\text{GSSP}})^2$. We accepted the point where the above merit function reached a plateau as the optimal size of the training set, that is 1000 and 5000 models for γ Dor and SPB stars, respectively (see also Figs. B.1 and B.2). Smaller training samples result in less accurate NN predictions, while larger samples require more computation time and only slightly improve the results. The training sample is larger for the SPB stars than for the γ Dor stars because the former cover a much wider temperature range.

3.2.2. Normalisation

Both grids were used to train a NN as described in Ting et al. (2019). The result is a 5D spectrum interpolator that we used to fit the observed HERMES spectra. The optimal stellar parameters of an observed spectrum can be found via least-squares fitting, which determines the best matching interpolated spectrum with its corresponding stellar parameters. This method can also incorporate the normalisation of the spectrum by adding extra free parameters to the fitting routine. This adaptation of

The Payne that includes normalisation is discussed in Straumit et al. (in prep.), and we give a brief summary of it here.

We assumed that the residual response function of a HERMES spectrum can be represented by a Chebyshev polynomial. We characterised Chebyshev polynomials with coefficients that are treated as free parameters alongside the atmospheric parameters. In each iteration of the fitting routine, the best fitting coefficients are used to construct a polynomial, which is introduced into the synthetic spectrum that is computed for the best fitting atmospheric parameters of that same iteration. This synthetic spectrum, containing now a proxy for the residual response function is compared to the observed HERMES spectrum. The iterations continue until convergence is reached. This way, the normalisation process is not subject to human intervention and is therefore more objective than any kind of manual spectrum normalisation. The latter typically assumes a subjective selection of continuum points and fitting a polynomial or a spline function through them to define the pseudo-continuum of the star. The resulting normalisation, and consequently the stellar parameters, are therefore highly dependent on the choice of the points. Even small offsets in the selected points can change the depth and shape of spectral lines, with the effect being typically more significant for broad hydrogen and helium lines. These are in turn important T_{eff} and $\log g$ diagnostic lines, hence (manual) spectrum normalisation can be a major source of uncertainty for the inferred atmospheric parameters and surface composition of the stars. Instead, our approach of combining stellar parameters and Chebyshev polynomial coefficients into a single vector of unknowns allows for a self-consistent inference of atmospheric properties and pseudo-continuum of the star. Details of our pseudo-normalisation procedure are presented in Straumit et al. (in prep.).

3.2.3. Performance of the neural network

Before applying the machine-learning procedure to observed data, we verified its performance on artificial data and benchmark stars. We computed ten synthetic spectra: four with stellar parameters within the ranges of SPB stars and six with typical values of γ Dor stars. Noise was added to simulate a $S/N \sim 100$ and a response function similar to that of a HERMES spectrum was introduced. For each spectrum, we determined the stellar parameters in three different ways: (1) using the NN approach as described in the previous (sub-)sections, which consists of the simultaneous optimisation of the stellar parameters and pseudo-continuum of the star; (2) making use of the inferred pseudo-continuum of the star, applying it to the original spectrum to obtain a normalised spectrum which is then analysed with GSSP; (3) manually normalising the spectrum by selecting continuum points, fitting a spline through them, and analysing the normalised spectrum with GSSP. The parameters obtained with these three methods were compared to the real values and are given in Table B.1. This test showed that the values for T_{eff} , $v \sin i$, ξ , and [M/H] determined with methods (1) and (2) agree with the real values to within the uncertainties. The $\log g$ values for F-type stars deviate by 0.05–0.1 dex for most of the spectra. It is well known that hydrogen lines in the spectra of F-type stars are insensitive to (small to moderate) $\log g$ variations (Gray 2005, Chaps. 13–14). This means that metal lines have to be used for the inference of $\log g$ of the star, hence degeneracy with [M/H] can be expected. To test the hypothesis that the deviations in the inferred $\log g$ values are due to a [M/H]– $\log g$ correlation, we fixed $\log g$ and ξ to their real values and repeated the analysis with method (2). The resulting [M/H] values are

Table 2. Stellar parameters from literature and the values obtained with The Payne for F-type benchmark stars π^3 Orionis and ι Piscium, and B-type benchmark stars η Ursae Majoris and HD 21071.

Reference	T_{eff} (K)	$\log g$ (dex)	[M/H] (dex)	$v \sin i$ (km s ⁻¹)	ξ (km s ⁻¹)
F-type: π^3 Orionis (S/N ₄₉₇₀ ~ 360)					
1	6420 ⁺²⁶ ₋₄₁	4.24 ^{+0.04} _{-0.07}	-0.02 ^{+0.02} _{-0.01}	–	–
2	6509 ± 81	4.38	+0.17 ± 0.13	18.5	2.22
3	6448 ± 50	4.29 ± 0.02	0.00 ± 0.04	–	–
The Payne	6536 ± 27	4.33 ± 0.06	-0.03 ± 0.02	19.2 ± 1.6	1.96 ± 0.09
F-type: ι Piscium (S/N ₄₉₇₀ ~ 490)					
1	6206 ⁺²⁶ ₋₆₀	4.11 ^{+0.06} _{-0.07}	-0.18 ^{+0.02} _{-0.03}	–	–
2	6177 ± 79	4.08	-0.11 ± 0.07	8.1	1.60
3	6192 ± 50	4.12 ± 0.02	-0.16 ± 0.04	–	–
The Payne	6109 ± 35	3.95 ± 0.06	-0.18 ± 0.02	3.71 ± 0.63	0.98 ± 0.12
B-type: η Ursae Majoris (S/N ₄₉₈₀ ~ 2200)					
4	16 494	4.17	0.0	–	2.0
5	17 783	–	–	161	–
The Payne	16 629 ± 71	4.20 ± 0.02	-0.14 ± 0.04	131.9 ± 4.6	2.64 ± 0.37
B-type: HD 21071 (S/N ₄₉₈₀ ~ 210)					
6	14 355 ± 99	–	–	54	–
7	14 768	4.30	-0.2	58	–
5	13 804	–	–	67	–
The Payne	14 043 ± 79	4.09 ± 0.02	-0.41 ± 0.05	51.0 ± 4.0	4.45 ± 0.53

References. (1) Boeche & Grebel (2016); (2) Luck (2017); (3) Aguilera-Gómez et al. (2018); (4) Gray et al. (2003); (5) Simón-Díaz et al. (2017); (6) Zorec & Royer (2012); (7) Saffe & Levato (2014).

found to be within the uncertainties of the previous ones, which allows us to conclude that the [M/H] determination is done correctly by the NN, but small deviations in the $\log g$ parameter is something to bear in mind. Most of the [M/H] and some of the other parameter results from method (3) are less consistent with the real values and we attribute this to difficulties in the placement of the pseudo-continuum (which is done manually in this case). Manual normalisation assumes that the apparent continuum is at unity. This is not necessarily the case, especially for F-type stars with their dense metal line spectra, and even more so for moderate and fast rotators ($v \sin i \gtrsim 40$ km s⁻¹). Thus, manual normalisation inevitably biases the parameter determination (e.g. Blanco-Cuadros et al. 2015; Giribaldi et al. 2019). For B-type stars, this effect is smaller because there are fewer metal lines present in the spectrum, making continuum normalisation easier.

In addition to the tests with synthetic spectra, we also compared the parameters predicted by the NN with literature values for a couple of F- and B-type standard stars that have been observed with HERMES and for which stellar parameter values are available in the literature. The results are shown in Table 2. These are real observations with real noise and artefacts from the Earth’s atmosphere and the instrument, which makes it more difficult to derive precise parameters. In addition, the literature values were obtained with data from different instruments and various analysis techniques. When taking this into account, the predictions from The Payne are comparable to literature values. Especially T_{eff} and $\log g$ are well determined by The Payne. Deviations in $v \sin i$ and ξ are the result of correlations between these two parameters and the absence of other broadening mechanisms in The Payne, such as macroturbulence.

The NN predictions for [M/H] are generally lower than those in the literature and this couples back to the pseudo-continuum placement.

The tests with artificial data and benchmark stars prove that a good performance is achieved with our NN-based approach. Concretely, we note that: (1) our approach delivers reliable atmospheric parameters which can further be adopted for the inference of elemental abundances; (2) deviations in $\log g$ of F-type stars of 0.05–0.1 dex is something to keep in mind, yet they are smaller than the typical $\log g$ uncertainty of $\gtrsim 0.15$ dex; (3) we expect to observe differences with literature values due to our superior approach of pseudo-normalisation, in particular for the [M/H] parameter.

3.3. Surface abundances

Currently, our version of The Payne that includes normalisation only delivers atmospheric parameters. We did not add surface abundances because it requires complex NNs that can resolve all high-resolution spectral features, and we would need larger training samples, which are very computationally demanding. The surface abundances for all observed spectra were instead derived with GSSP (Tkachenko 2015). This code calculates a grid of synthetic spectra and compares each one of them to the observed spectrum. The χ^2 merit function is used as a measure of the goodness of fit. For every parameter or element abundance of the observed spectrum, the optimal value and its uncertainty are determined by projecting χ^2 values of the entire grid on to the parameter or abundance in question. This allows us to take covariances between parameters/abundances into account when computing uncertainties. A polynomial of third or fourth order is

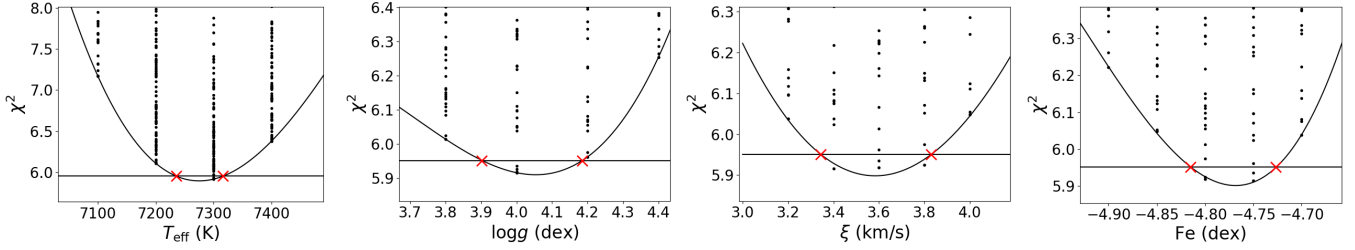


Fig. 2. Projection of the χ^2 hyper surface with respect to T_{eff} , $\log g$, ξ and the Fe abundance for γ Dor star KIC 7365537. The black dots are χ^2 values for all the grid nodes, the black curve is a polynomial fit with the best-fit value as minimum, and the red crosses show the intersection points of this fit with the 1σ χ^2 level (the horizontal line) and give the errors on the best-fit value.

fit to the lowest χ^2 values to search for the global minimum. The errors are given by the intersection of this fit with the 1σ limit in terms of χ^2 . This is illustrated in Fig. 2 for KIC 7365537.

We used the GSSP software package to determine individual elemental abundances for our stars. For every star in the sample, we normalised the observed spectrum by dividing it through the (residual) response function approximated with the Chebyshev coefficients obtained with The Payne algorithm in the previous step. We fixed $[M/H]$ and $v \sin i$ to The Payne values and derived abundances for C, O, Na, Mg, Al, Si, S, Ca, Sc, Ti, V, Cr, Mn, Fe, Co, Ni, Cu, Zn, Sr, Y, Zr, Ba (γ Dor), and He, C, N, O, Ne, Mg, Si, S, Ca, and Fe (SPB). Abundances of elements with many strong lines in the spectrum, such as Fe, Ni, Ti and Cr for γ Dor stars and He for SPB stars, have to be optimised together with T_{eff} , $\log g$, and ξ atmospheric parameters (Gray 2005, Chap. 16). To take this into account, we allowed these parameters to vary in a small interval around the values found with The Payne algorithm. Furthermore, since elemental abundances are optimised one-by-one in GSSP, it is essential to perform abundance analysis in an iterative way to account for the fact that the abundance of the element in question can be influenced by the presence of lines of other elements due to spectral line blending. This is relevant for chemical elements that show numerous lines in the spectrum, and we found that typically two or three iterations are sufficient to achieve the convergence, that is when the abundance value does not deviate more than the typical uncertainty between two consecutive iterations. For chemical elements that display fewer lines in the spectrum, abundances were inferred using small wavelength ranges around positions of the corresponding spectral lines.

The abundance values returned by GSSP are given as $\log(n_X/n_{\text{tot}})$, with n_X the number density of element X and n_{tot} the total number density of all elements. However, abundances in the literature are mostly given relative to solar ones, that is $[X/H]$. The results from GSSP are converted to $[X/H]$ as follows:

$$[X/H] = \log\left(\frac{n_X}{n_H}\right) - \log\left(\frac{n_X}{n_H}\right)_\odot \quad (1)$$

$$= \log\left(\frac{n_X}{n_{\text{tot}}}\right) - \log\left(\frac{n_H}{n_{\text{tot}}}\right) - \log\left(\frac{n_X}{n_H}\right)_\odot \quad (2)$$

$$= \log\left(\frac{n_X}{n_{\text{tot}}}\right) - \log\left(\frac{n_H}{n_{\text{tot}}}\right) - \log \epsilon_{X,\odot} + 12. \quad (3)$$

The first term in Eq. (3) is the GSSP output, for the second term we use the same value for all stars ($\log(n_H/n_{\text{tot}}) = -0.036$, Asplund et al. 2005) since the sample has a relatively small $[M/H]$ range, and the third term ($\log \epsilon_{X,\odot}$) is the solar value for element X (in 12 scale) from Asplund et al. (2005). The $[X/H]$ notation is the one used in the abundance tables of this paper.

The values are converted to 12 scale ($\log \epsilon_X = \log\left(\frac{n_X}{n_H}\right) + 12$) by adding the value for $\log \epsilon_{X,\odot}$.

Figure 3 shows part of the relatively low S/N spectrum ($S/N = 60$) of a slowly rotating γ Dor star in the top row and the high S/N spectrum ($S/N = 170$) of a fast rotating γ Dor star in the bottom row. In Fig. 4, the spectrum of an SPB star with typical S/N of the SPB sample is plotted. All the spectra are over-plotted by their best fitting synthetic spectrum and zoomed in on the Balmer lines and a region with metal lines to demonstrate the quality of the fits we typically obtained for the whole sample. For every star in the sample, we made similar diagnostic plots to visually check the quality of the fit.

4. Results

The stellar parameters and surface abundances we obtained for the γ Dor stars are given in Tables C.1, C.2, and C.3. The results of the SPB stars can be found in Tables D.1 and D.2. For all five parameters, we report the values and uncertainties from the fitting routine with the NN in Cols. 2–6. Additionally, in Cols. 7–9 we give the values for T_{eff} , $\log g$ and ξ determined with GSSP after optimising the abundances of elements with many spectral lines. The abundances in the tables are given in the $[X/H]$ format, and the uncertainties on the solar values of Asplund et al. (2005) are taken into account.

Typical uncertainties (although this depends on S/N) for the γ Dor sample are $\Delta T_{\text{eff}} \sim 65$ K, $\Delta \log g \sim 0.2$ dex, $\Delta[M/H] \sim 0.05$ dex, $\Delta v \sin i \sim 4$ km s $^{-1}$, and $\Delta \xi \sim 0.3$ km s $^{-1}$. For the SPB stars, the uncertainties are larger with typical values of $\Delta T_{\text{eff}} \sim 700$ K, $\Delta \log g \sim 0.15$ dex, $\Delta[M/H] \sim 0.15$ dex, $\Delta v \sin i \sim 13$ km s $^{-1}$, and $\Delta \xi \sim 3$ km s $^{-1}$. This is expected since most of the SPB spectra have lower S/N values and B-type stars have much fewer spectral lines (see Fig. 4), which complicates the parameter determination. Non-LTE effects on stellar parameters also become increasingly important at higher temperatures (Przybilla et al. 2011), but these are not taken into account in the current analysis because we specifically chose to perform a homogeneous analysis for all the stars in this legacy sample, treating both F- and B-type stars in the same way.

4.1. γ Dor stars

Distributions of the final stellar parameters and some element abundances for the γ Dor stars are shown in Fig. 5. On top of each panel, the mean value and standard deviation of that parameter is given. Most of the γ Dor stars have a temperature within the expected range, which is 6700–7900 K (Aerts et al. 2010), but there are a few hotter stars with a temperature around 8000 K. This is further discussed in Sect. 5.1. There is a wide spread in

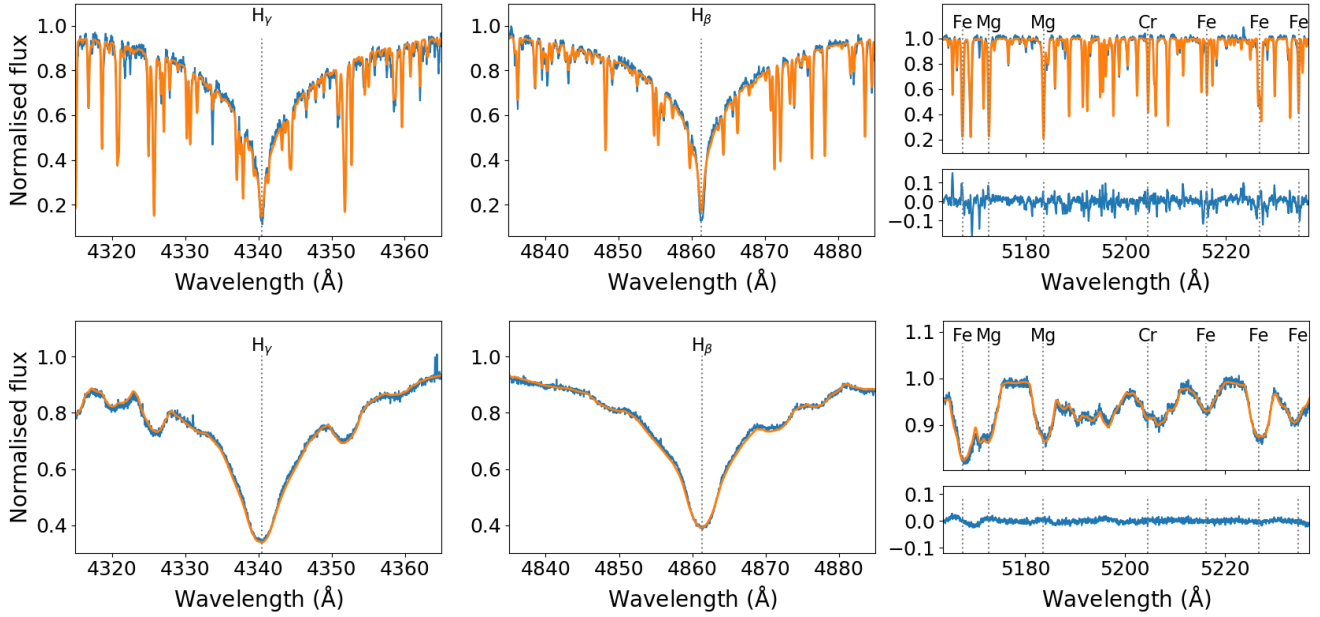


Fig. 3. *Top:* spectrum of γ Dor star KIC 9751996 ($S/N=50$) with $T_{\text{eff}}=7139$ K, $\log g=3.66$ dex, $v \sin i=12.1$ km s $^{-1}$, $\xi=3.38$ km s $^{-1}$ and $[M/H]=+0.12$ dex in blue and best fitting synthetic spectrum in orange. *Bottom:* same for KIC 7365537 ($S/N=170$) with $T_{\text{eff}}=7274$ K, $\log g=4.02$ dex, $v \sin i=148.3$ km s $^{-1}$, $\xi=3.59$ km s $^{-1}$ and $[M/H]=-0.23$ dex. The bottom parts of the right panels show the residuals.

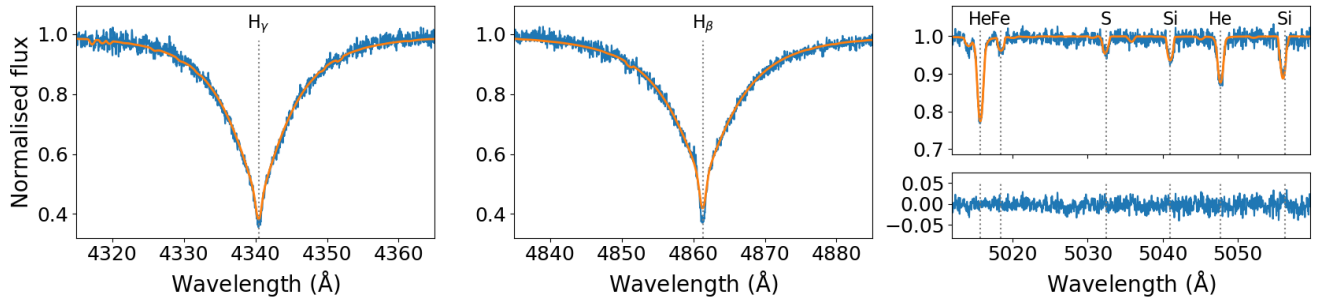


Fig. 4. Spectrum of SPB star KIC 3756031 ($S/N=90$) with $T_{\text{eff}}=15947$ K, $\log g=3.69$ dex, $v \sin i=31.7$ km s $^{-1}$, $\xi < 3.9$ km s $^{-1}$ and $[M/H]=-0.44$ dex in blue and best fitting synthetic spectrum in orange. The bottom part of the right panel shows the residuals.

$\log g$ and some targets have values close to 3 dex, implying that they are close to or even beyond the end of the main sequence. They cover a $v \sin i$ range from 0 to 200 km s $^{-1}$, and ξ is distributed around 3 km s $^{-1}$. There is one outlier, KIC 7215607, for which only an upper bound on ξ could be determined, thus we fixed its value to 2 km s $^{-1}$ in the further analysis. We note that the $[M/H]$ and $v \sin i$ distributions shown in Fig. 5 are the results obtained with the NN, while the distributions of T_{eff} , $\log g$, ξ , and the C and O abundances are those from the final GSSP analysis. This is due to the abundances being optimised along with T_{eff} , $\log g$, and ξ as explained in Sect. 3.3.

The $[M/H]$ distribution peaks at around a value of -0.21 ± 0.12 dex with some outliers at both ends. This value is slightly sub-solar and is lower than what is found in other literature studies for this sample of γ Dor stars, as shown in Fig. 6. In this figure, we compare our NN values of T_{eff} , $\log g$, $v \sin i$, and $[M/H]$ with values from catalogue studies that determined spectroscopic stellar parameters for most of the stars in our sample. We used the NN values and not the final GSSP results in this comparison since they were determined before the optimisation of individual abundances, as was the case in the literature studies. The error bars are the propagated uncertainties derived from the NN application and those reported in the literature. Frasca et al. (2016) and Qian et al. (2019) used LAMOST

spectra, which have a resolution of only ~ 1800 (Zhao et al. 2012). The studies by Niemczura et al. (2015), Tkachenko et al. (2013), and Van Reeth et al. (2015) analysed HERMES data and the latter two also used the GSSP code. For some stars, our T_{eff} and $\log g$ deviate from these literature values and our $v \sin i$ is consistent when taking the uncertainties into account. But the $[M/H]$ we find is systematically ~ 0.2 dex lower. We also compared our $[M/H]$ distribution to that of a different sample of γ Dor stars from Bruntt et al. (2008). The latter consists of 18 stars with a mean $[M/H]$ of -0.03 ± 0.23 dex. The two distributions largely overlap within the uncertainties, but the majority of stars analysed here have $[M/H]$ values at the lower end of the distribution in Bruntt et al. (2008), with some stars being more metal poor. For most of these literature studies it is unclear which solar composition is adopted to compute $[M/H]$, but the largest possible difference in solar metallicity is about 0.1 dex, thus the literature metallicities are still systematically lower than those in this work. Other reasons for the $[M/H]$ offset could be different model atmospheres used in the literature, different analysis methods, or differing data quality (high- versus low-resolution). From our tests in Sect. 3.2.3, we conclude that the $[M/H]$ offset between our results and literature values is not an underestimation by the NN, since it predicts correct metallicities and other parameters for synthetic spectra. Instead, we hypothesise that the T_{eff} , $\log g$

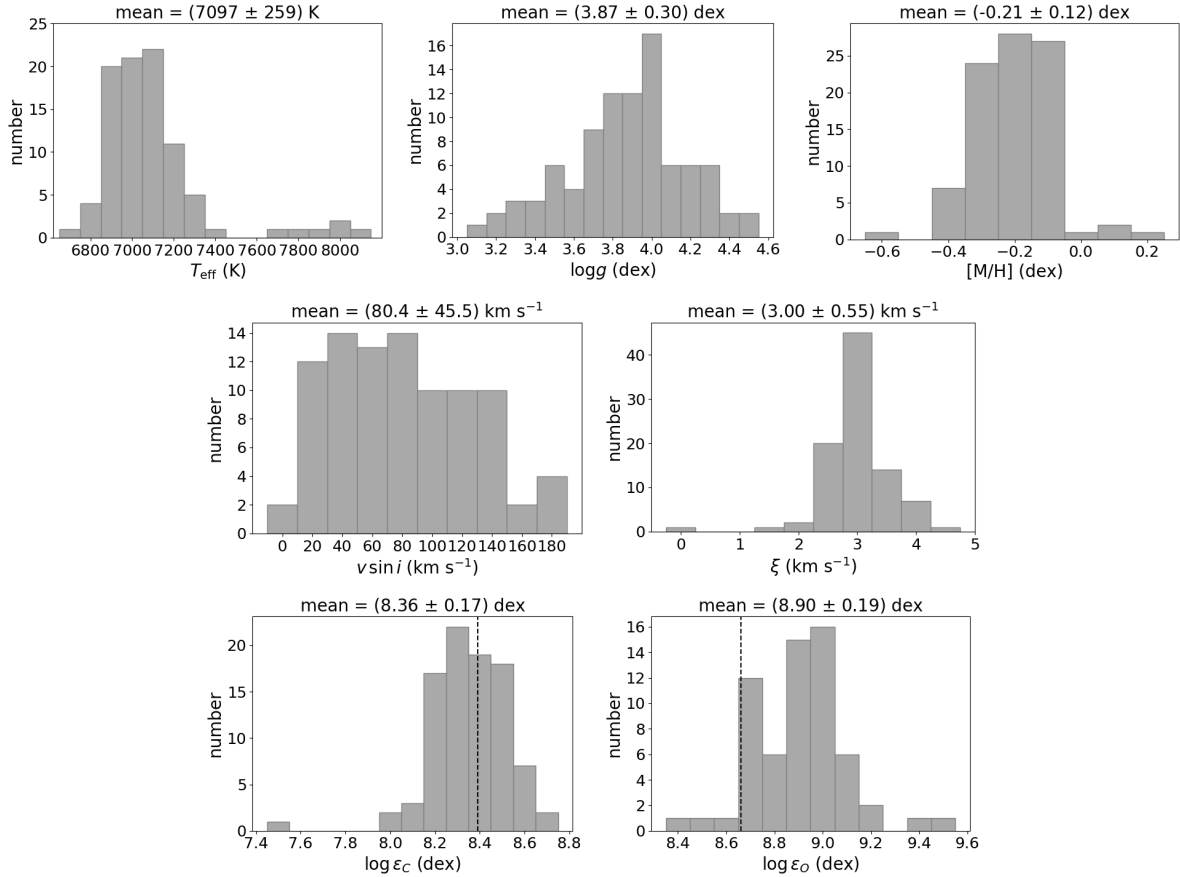


Fig. 5. Histograms of T_{eff} , $\log g$, $[M/H]$, $v \sin i$, ξ , and the abundances of C and O in 12 scale for the sample of γ Dor stars. The $[M/H]$ and $v \sin i$ values are the results from the NN, while T_{eff} , $\log g$, ξ , and the C and O abundances are those obtained with GSSP. Solar values of the abundances are indicated with a black dashed line.

and $[M/H]$ differences are caused by the manual normalisation of the spectra done in mentioned literature papers, which resulted in different placement of the continuum. T_{eff} is determined by the shape and depth of the hydrogen lines, while $\log g$ only depends on their inner core strength and on metal lines. Small differences in normalisation of the hydrogen lines result in different T_{eff} and $\log g$ values. This has an effect on $[M/H]$, since this parameter has to compensate for the T_{eff} changes and normalisation differences in the metal line regions. If the pseudo-continuum of the observed spectrum is placed higher, the spectrum is pulled down and this correspond to higher opacities in the stellar atmospheres and thus higher $[M/H]$ values. The amount by which the parameters differ depends on the wavelength regions and the number of hydrogen lines used in the atmospheric analysis. Furthermore, we expect larger deviations when the analysis includes global continuum scaling, which in the case of F-type stars shifts the continuum downwards, increasing $[M/H]$.

We were able to verify this normalisation statement by comparing our NN normalised spectra with manually normalised HERMES spectra that are available for the 37 stars in the sample of [Van Reeth et al. \(2015\)](#). These authors used a wavelength range between 4700 and 5800 Å for the atmospheric analysis and normalised the spectra by consecutively fitting a cubic and a linear spline to the continuum. We plotted both normalisations on top of each other for each of the 37 γ Dor stars and found that the manual normalisations are systematically shifted downwards with respect to the NN normalisations. We demonstrate this in Fig. 7 for part of the spectrum of KIC 7023122, where we over-plot each spectrum with its best fitting synthetic

spectrum. The $[M/H]$ determined for this star by [Van Reeth et al. \(2015\)](#) is $+0.04 \pm 0.08$ dex, while we found a value of -0.34 ± 0.03 dex. There is also a difference of more than 100 K in T_{eff} and 0.46 dex in $\log g$. Additionally, in Fig. 6 we observed similar patterns in the offsets of T_{eff} , $\log g$ and $[M/H]$, proving the connection between the derivation of these parameters. The various literature studies used different wavelength regions and some of them adopted a global continuum scaling. This explains why the values are different for all literature works. The largest discrepancies are found for the $[M/H]$ values of [Van Reeth et al. \(2015\)](#), who used global continuum scaling and obtained higher $[M/H]$ values than the other studies and the NN results.

This confirms that the small T_{eff} and $\log g$ offsets and the $[M/H]$ inconsistency of ~ 0.2 dex is actually due to normalisation of the continuum level. We point out that this process is highly dependent on the positioning of points to which a polynomial or spline is fitted in order to define the continuum. Often, points are selected in the upper part of the noise level, while the NN normalisation fits a synthetic spectrum to the centre of the noise. From our analysis, we are not able to tell which normalisation and corresponding parameters are correct. Independent, non-spectroscopic parameters are needed to lift the normalisation- (T_{eff} , $\log g$, $[M/H]$) degeneracy.

Apart from the global metallicity, the individual abundances are also affected. We derived the surface abundances of some elements from the manually normalised spectra with the same method as explained in Sect. 3.3 and compared the results with the values in Tables C.2 and C.3. The average differences and

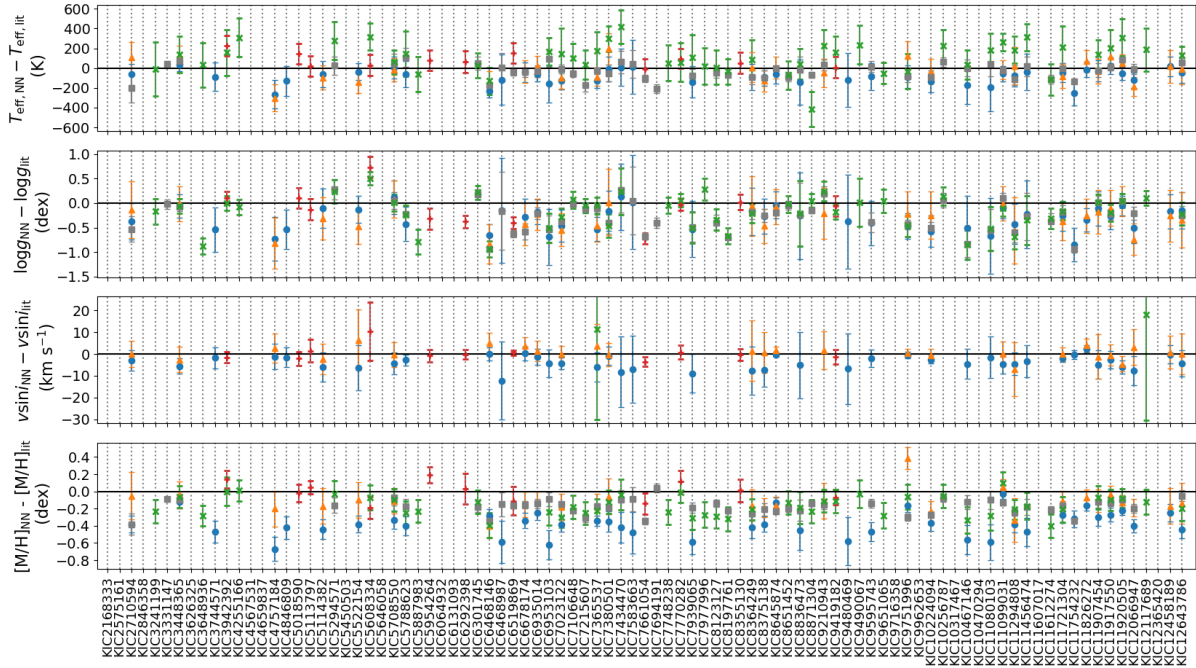


Fig. 6. Comparison of γ Dor stellar parameters from the NN with literature values. *From top to bottom:* the difference between the values in this paper and the ones from literature catalogues are shown for T_{eff} , $\log g$, $v \sin i$, and $[M/H]$. Both the errors obtained from the NN and those from the literature are propagated to obtain the plotted error bars. The different symbols correspond to Tkachenko et al. (2013; orange triangles), Van Reeth et al. (2015; blue circles), Niemczura et al. (2015; red pluses), Frasca et al. (2016; green crosses), and Qian et al. (2019; grey squares).

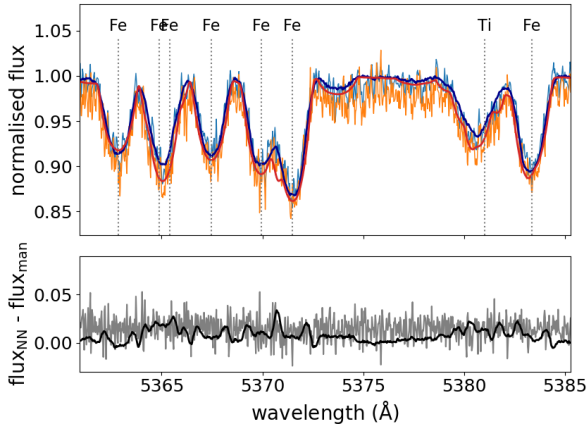


Fig. 7. Comparison of automated NN and manual normalisation for part of the spectrum of KIC 7023122. The NN normalisation and best fitting predicted spectrum are shown in blue and dark blue. The manually normalised spectrum and a synthetic spectrum computed for the corresponding parameters from Van Reeth et al. (2015) are plotted in orange and red. The lower panel shows the difference between the automated and manually normalised spectrum in grey, and the black line is the difference between the synthetic spectra. The most prominent element lines are indicated by dotted lines.

standard deviations are given in the headers of those tables. These differences give an estimate of how much normalisation can affect abundance determinations. The differences are around a few tenths of a dex for most elements and even reach 0.7 dex for Mn and Ba. This is normal for Mn and Ba since there are only a few lines of these elements present in the spectra and most of them are blended.

The mean abundance uncertainty is different for every element. Fe and Mg could be determined with a precision below 0.1 dex; C and Ti have uncertainties of about 0.15 dex; the errors

of Na, Ca, Sc, Cr, Mn, Ni and Ba lie around 0.2 dex; Y has a mean uncertainty of 0.3 dex, and that of Sr is ~ 0.6 dex. For the remaining elements, often only an upper limit could be found (this is indicated as such with the less than (<) symbol in Tables C.2 and C.3) or uncertainties larger than 2 dex were obtained. The largest abundance uncertainties correspond to spectra with low S/N values. The metal lines in these spectra disappear into the noise, making it impossible to determine lower bounds on the abundances.

The abundances in Tables C.2 and C.3 are given with respect to the Sun and the average values over the whole sample are shown in Fig. 8. As expected from the $[M/H]$ values, most of the γ Dor stars have negative abundances, and thus a sub-solar composition, except for Ba, which is over-abundant in the majority of stars. There are only two Ba lines present in the wavelength range used in the analysis and both are heavily blended with other spectral lines. On top of that, one of the Ba lines (next to the H_{β} hydrogen line) is a resonant one, so the results for Ba should be taken with caution. The average abundances of O and Co are also metal-rich. These elements only have a few weak lines in the F-type temperature range, and for most of the stars only an upper bound or large errors on the abundance could be found. KIC 4757184, KIC 6292398, KIC 9751996, and KIC 11099031 have systematically lower or higher abundances than the rest of the sample. These are also the stars with metallicities that deviate the most from the sample distribution, with KIC 4757184 being metal poor ($[M/H] = -0.65$ dex). The other three are the only γ Dor stars with positive $[M/H]$. We checked the abundance patterns of all stars for chemical peculiarities. Most of the stars have near-solar composition within the (sometimes large) error bars. Only one star, KIC 6292398, is found to be a metallic line A star (Am star). It has under-abundances of C, Ca, and Sc, while the heavy metals are enhanced (Preston 1974). This star had already been classified as an Am star by Niemczura et al. (2015). By ordering the elements according to their mean

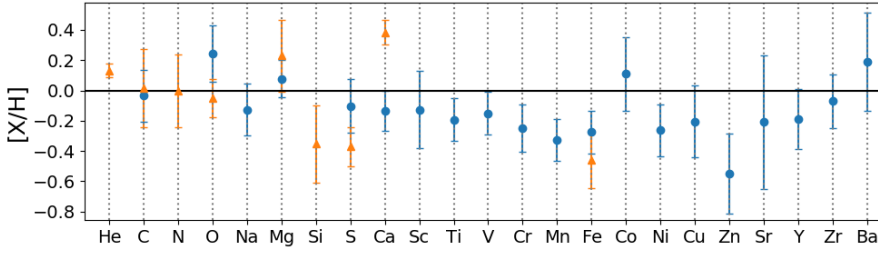


Fig. 8. Average surface abundances with standard deviation of the γ Dor (blue circles) and SPB (orange triangles) samples with respect to the solar composition of [Asplund et al. \(2005\)](#).

uncertainties, it follows that Fe, Mg, C, Ti, and to lesser extent Na, Ca, Sc, Cr, Mn, Ni, and Ba are the best candidates to study and constrain interior physical processes.

4.2. SPB stars

The distributions of the final SPB parameters and a few abundances are shown in Fig. 9. The temperatures are scattered over the full range typical for SPB stars, which is 11 000–22 000 K ([Aerts et al. 2010](#)). Most of the stars have $\log g$ values around 3.8 dex, but there are a few with lower values and KIC 8766405 especially seems to be more evolved. Just as for the γ Dor stars, the $[M/H]$ distribution is centred around -0.2 dex. The SPB stars have projected rotational velocities over a wide range of values from 20 to 300 km s^{-1} . It is difficult to determine ξ as these stars only have a few metal lines and these are broadened by the fast rotation. For four SPB stars, it was difficult to constrain ξ . In that case, the value was fixed at 2 km s^{-1} , which is a typical value for unevolved, core-hydrogen burning stars of intermediate mass ([Gray 2005](#), Chap. 17), and which is also adopted in many model atmosphere codes (e.g. [Kurucz 1992](#); [Lanz & Hubeny 2007](#)). This value agrees with the NN determinations within the 1σ uncertainties that, for these stars, reach over 60% of the ξ values themselves.

We compare our NN results to values in the literature in Fig. 10. There are far fewer SPB stars than γ Dor stars known and fewer catalogue studies are available. Therefore, we also included papers that only studied one or just a few SPB stars. [Lehmann et al. \(2011\)](#) used spectra obtained with the Coude-Echelle spectrograph attached to the 2 m telescope at Thüringer Landessternwarte that has a resolution of 32 000. The data were analysed with an early version of GSSP, and apart from the stellar parameters, the surface abundances were also determined. In [Balona et al. \(2011b\)](#), low-resolution ($R \sim 550$) spectra taken with the B&C spectrograph on the Bok telescope at Kitt Peak observatory were analysed with LTE models. The largest SPB samples are found in [Frasca et al. \(2016\)](#) and [Zhang et al. \(2018\)](#), which exploit LAMOST data. Two stars were studied in [Pápics et al. \(2015, 2017\)](#) using HERMES data and the GSSP code. Only six SPB stars, with spectra from the RC spectrograph at KPNO 4 m Mayall telescope ($R \sim 7200$), were analysed with a non-LTE method by [Hanes et al. \(2019\)](#). Most of the parameters are consistent with these literature values, especially considering the large uncertainties for these hotter stars and the different methods used in all of the studies. We compare the $[M/H]$ distribution of our sample with that of another sample of SPB stars ([Niemczura et al. 2009](#)). The mean and standard deviation of both samples are -0.21 ± 0.12 dex and -0.21 ± 0.46 dex respectively, so the SPB $[M/H]$ values in this paper are typical for this kind of stars.

The SPB sample contains spectra that in general have low S/N for this kind of stars. Therefore, the abundance determination of the SPB stars is more difficult than that of the γ Dor sample. The SPB stars are hotter and therefore have fewer metal

lines. Most of them are also fast rotators, which means that the few lines that are present are often largely broadened and sometimes disappear into the noise. This is reflected in the precision of the abundances that were estimated. For many elements, such as Ne and Ca, only an upper limit could be determined, or only estimated values with very large errors are obtained. Only He has an uncertainty below 0.1 dex. C, Mg, Si, and S have precisions between 0.15 and 0.25 dex, and the typical uncertainty on O, N, and Fe is around 0.45 dex. This is partially caused by the low S/N of the spectra, given that the *Kepler* SPB stars are faint for the 1.2 m Mercator telescope. Because of the large uncertainties, it is difficult to find trends in the abundances. As expected from the metallicities and illustrated in Fig. 8, Fe, Si, and S are generally below the solar value. We also find that the SPB stars are somewhat helium rich. However, this result should be taken with caution since non-LTE effects will strengthen the cores of He lines ([Nieva & Przybilla 2007](#)), leading to lower He abundances closer to solar value. Most of the abundances are also comparable with those of the cosmic B-star standard ([Przybilla et al. 2008](#); [Nieva & Przybilla 2012](#)), except for Si and Fe, which have lower abundances.

5. Discussion

5.1. Location in the Hertzsprung-Russell diagram

In Fig. 11, the whole sample is plotted in an HRD, based on our T_{eff} , $\log g$ and $[M/H]$ determination. We computed luminosities with

$$\log \frac{L}{L_{\odot}} = -0.4 (M_{S,i} + \text{BC}_{S,i} - M_{\text{bol},\odot}) \quad (4)$$

and

$$M_{S,i} = m_{S,i} - 5 \log \frac{d}{10 \text{ pc}} - R_{S,i} E(B - V), \quad (5)$$

with $m_{S,i}$ the apparent magnitudes from SIMBAD in the Johnson V-band or in the *Gaia* G-band when the V-band is not available. There are three γ Dor stars with neither V- nor G-band magnitudes available, for which we used their *Kepler* (K) magnitudes from the MAST archive. d are *Gaia* eDR3 distances from [Bailer-Jones et al. \(2021\)](#), and $E(B - V)$ are reddening values obtained with the 3D reddening map (Bayestar19) from [Green et al. \(2019\)](#). The reddening vector $R_{S,i}$ is equal to 3.089 (V- or K-band) or 3.002 (G-band) ([Pedersen et al. 2020](#)). For the γ Dor stars with V- or -band magnitudes, we computed bolometric corrections ($\text{BC}_{S,i}$) with prescriptions from [Flower \(1996\)](#) with $3.7 < \log T_{\text{eff}} < 3.9$, and we used $M_{\text{bol},\odot} = 4.73$ ([Torres 2010](#)). The BC_G values for the γ Dor stars with G-band magnitudes were obtained with coefficients from [Andrae et al. \(2018\)](#), which has a corresponding $M_{\text{bol},\odot} = 4.74$. For the SPB stars, the prescriptions from [Pedersen et al. \(2020\)](#) (model 3, LTE+non-LTE)

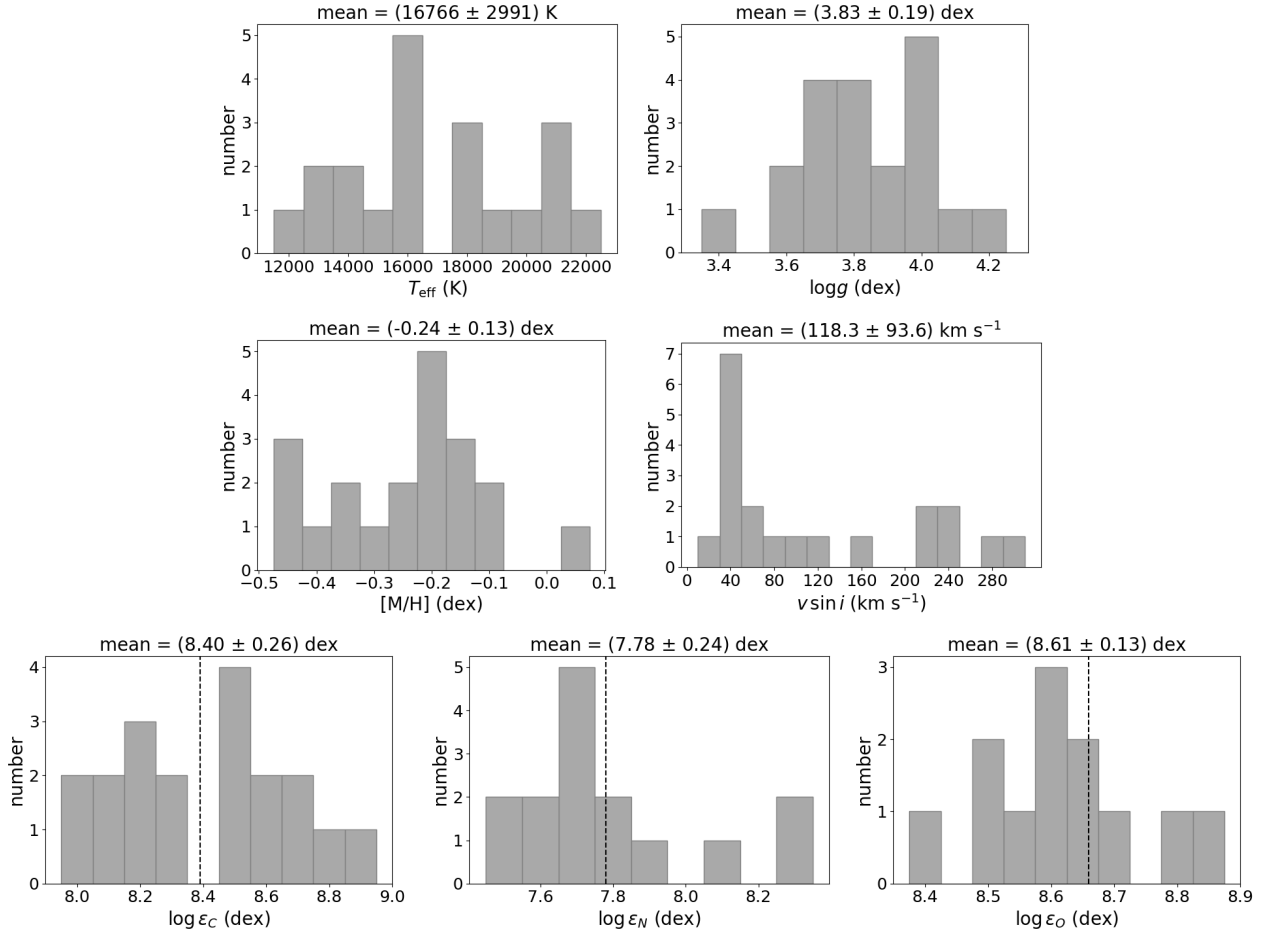


Fig. 9. Histograms of T_{eff} , $\log g$, $[M/H]$, $v \sin i$, and C, N, and O abundances in 12 scale for the sample of SPB stars. The $[M/H]$ and $v \sin i$ values are the results from the NN, while T_{eff} , $\log g$, and the C, N, and O abundances are those obtained with GSSP. Solar values of the abundances are indicated with a black dashed line.

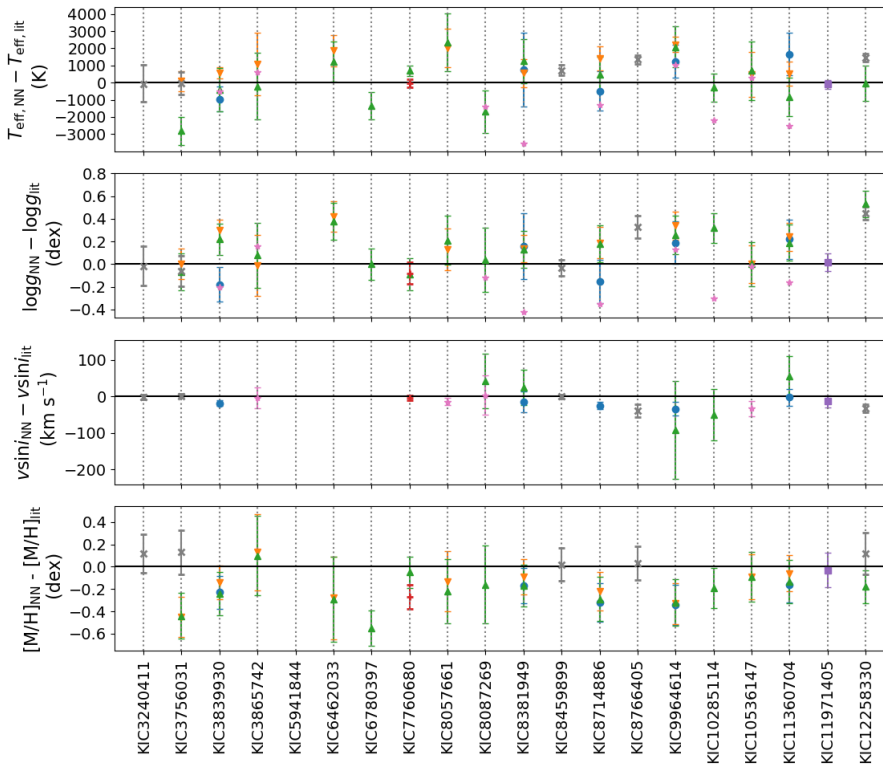


Fig. 10. Comparison of SPB stellar parameters from the NN with literature values. *From top to bottom*, the difference between the values in this paper and the ones from literature catalogues are shown for T_{eff} , $\log g$, $v \sin i$, and $[M/H]$. Both the errors obtained from the NN and those from the literature are propagated to get the shown error bars. The different symbols correspond to [Lehmann et al. \(2011\)](#); grey crosses), [Balona et al. \(2011b\)](#); pink stars), [Pápics et al. \(2015\)](#); red pluses), [Frasca et al. \(2016\)](#); green triangles), [Pápics et al. \(2017\)](#); purple squares), [Zhang et al. \(2018\)](#); orange reversed triangles), and [Hanes et al. \(2019\)](#); blue circles).

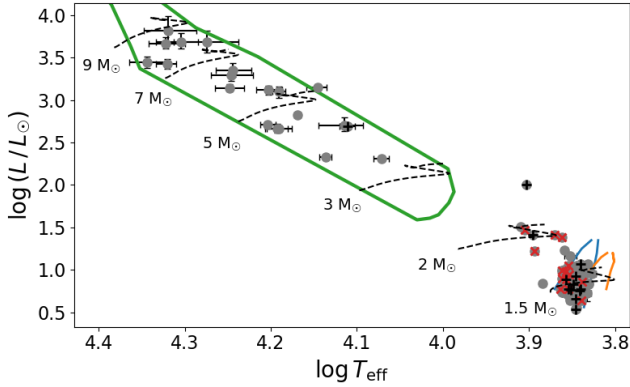


Fig. 11. Hertzsprung-Russell diagram containing the γ Dor and SPB stars studied in this work. The γ Dor instability strips are from Dupret et al. (2005), for $\alpha_{\text{mlt}} = 1.5$ (orange) and $\alpha_{\text{mlt}} = 2.0$ (blue), while the SPB instability strip (green) is taken from Szewczuk & Daszyńska-Daszkiewicz (2017). All these strips were computed for solar metallicity. The red crosses are hybrid γ Dor - δ Sct stars, and the black pluses are SB1 stars. Evolutionary tracks for different masses taken from (Johnston et al. 2019) and covering from zero age- to the terminal-age main sequence are plotted as black dashed lines to guide the eye.

were adopted, and $M_{\text{bol},\odot} = 4.74$. The luminosity values are given in the last columns of Tables C.1 and D.1.

The orange and blue lines in Fig. 11 are the theoretical γ Dor instability strips from Dupret et al. (2005) for a mixing length parameter (α_{mlt}) of 1.5 and 2.0, respectively. The parameter α_{mlt} determines the length scale over which convective blobs move in MLT (Böhm-Vitense 1958) before they dissolve in their surroundings, and hence it affects the size of the convective envelope in low- and intermediate-mass stars (Viani et al. 2018). Higher values of α_{mlt} lead to larger convective envelopes and shift the red edge of the instability strip based on the flux-blocking excitation mechanism towards higher T_{eff} (Dupret et al. 2005). Almost all objects in our legacy sample fall within the instability region for $\alpha_{\text{mlt}} = 2.0$. There are ten stars, including five hybrid γ Dor - δ Sct pulsators and two SB1 systems, that have a higher temperature and luminosity than theoretically predicted by excitation models. These hot γ Dor ($-\delta$ Sct) stars have been discussed in other studies as well, including the instability study based on the flux-blocking mechanism based on time-dependent convection by Dupret et al. (2005). Stars with such high temperatures do not have sufficiently deep convective envelopes for this mechanism to be effective. Different explanations have been given in the literature, such as binarity, where the γ Dor star has a hotter non-pulsating A- or B-type companion (Balona et al. 2011a), or rapidly rotating SPB stars appearing to be cooler due to gravity darkening (Salmon et al. 2014; Balona et al. 2015). Antoci et al. (2014) showed that high-order non-radial pulsations might also be excited stochastically by turbulent pressure in the hydrogen ionisation zone. Grassitelli et al. (2015) included turbulent pressure in stellar evolution calculations and found that the region in the HRD that contains models with a high fraction of turbulent pressure coincides with the observational γ Dor instability strip, such that these stars can excite stochastic gravito-inertial modes. However, Fig. 1 in that paper reveals that the turbulent pressure fraction of the five hottest γ Dor stars is small (<0.02) implying that this excitation mechanism is not efficient for these hotter stars. Only two of the outliers are found to be in a spectroscopic binary based upon the RV measurements of their spectra (KIC 7694191, which has the highest luminosity of the sample, and KIC 6292398). None of the hot γ Dor ($-\delta$ Sct)

stars have a large value of $v \sin i$ that suggests either slow to moderate rotation or low inclination angle i . In both those cases, we can reject the hypothesis of rapidly rotating SPB stars because gravity darkening is negligible in the former case, whereas the star is observed nearly pole-on in the latter case, and the T_{eff} determination is not subject to the gravity darkening effect either. Similar conclusions were found by Balona et al. (2016) and Kahraman Aliçavuş et al. (2020), who did not find signs of binarity or rapidly rotating SPB stars in hot γ Dor samples either. The existence of such hot γ Dor stars suggests that the mode excitation in F-type stars is not yet fully understood. The problem of the pulsation mode excitation is beyond the scope of this observational spectroscopy paper.

For the SPB stars, we used the theoretical instability strip from Szewczuk & Daszyńska-Daszkiewicz (2017). All the B-type targets in our legacy sample lie within the theoretically predicted region.

5.2. Signatures of mixing processes

Mixing processes in the envelopes of stars can reveal themselves by changing element abundances at the stellar surface. All the stars in our legacy sample burn hydrogen into helium via the CNO cycle, although the pp-chain is also active in γ Dor stars. During the initial phase of the CNO cycle, most of the C is transformed into N, creating an excess of N, while C is depleted and the O level stays almost constant. Efficient mixing processes can transport the elements. Hence, surface abundances of C, N, and O and their ratios can be used as tracers of mixing (Maeder & Meynet 2000; Langer 2012). Several studies have looked at N abundances as a function of $v \sin i$ (Hunter et al. 2008, 2009; Brott et al. 2011) and found a positive correlation. These studies also reported a group of slowly rotating stars that are nevertheless N enriched. This cannot be explained by the current theory of rotational mixing and is attributed to magnetic fields (e.g. Morel et al. 2008). However, Aerts et al. (2014) delivered an alternative explanation in terms of pulsational wave mixing, in view of the absence of any correlation between the surface N abundance and the rotation frequency in a sample of OB-type dwarfs studied from ground-based photometry, spectro-polarimetry, and high-precision spectroscopy. This study was based on direct measurements of the rotation frequency at the surface or in the envelope of stars, rather than using projected rotation velocities from spectroscopy, which are subject to uncertainty due to the unknown inclination angle.

Przybilla et al. (2010), Maeder et al. (2014), and Martins et al. (2015) used the relations between N/C and N/O and between N/C and $\log g$ to study the mixing in OB-type stars. N/C and N/O track the evolution in terms of nucleosynthesis, while $\log g$ is a proxy for the evolution in the HRD. From the theory of nucleosynthesis, it follows that N/C and N/O should be tightly correlated, and the different studies find various theoretical limits depending on the mass of the star and the adopted solar abundances. A correlation between N/C and $\log g$ is also expected since the N abundance should increase with age, or decrease with $\log g$.

The CNO cycle becomes more important with temperature. F-type stars have few N lines and we were not able to determine the N abundance in any of the γ Dor stars. We did constrain the abundances of C and O, and these can also be used as tracers of the CNO cycle, although to a lesser extent. In Figs. 12 and 13, the ratio between C and O is plotted as a function of $\log g$ and $v \sin i$, respectively. Since nucleosynthesis theory predicts that C is depleted with time while O stays constant, we expect to see

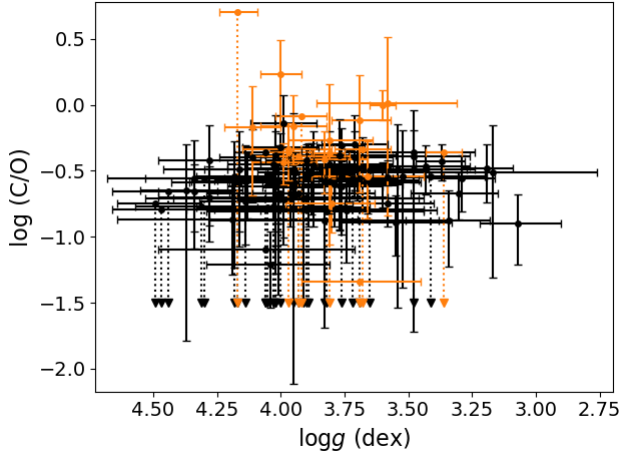


Fig. 12. Log (C/O) as a function of $\log g$ for the sample of γ Dor stars in black and for the SPB stars in orange.

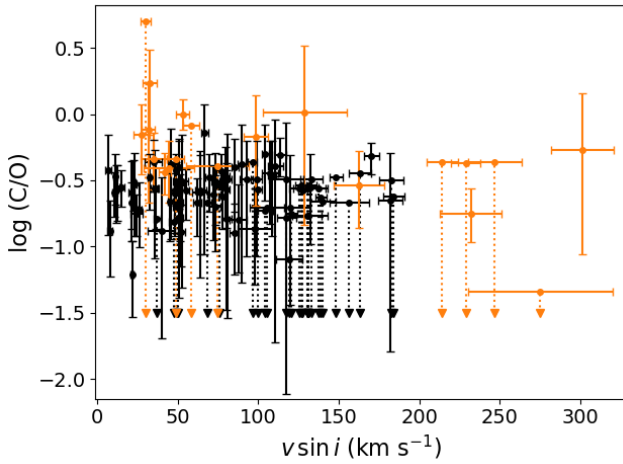


Fig. 13. Log (C/O) as a function of $v \sin i$ for the sample of γ Dor stars in black and for the SPB stars in orange.

a correlation with $\log g$. For faster rotating stars, mixing should be more efficient, thus stars with a higher $v \sin i$ should have lower C/O ratios. We do not detect this from visual inspection nor from Pearson correlation coefficients, which are equal to -0.12 for $\log g$ and 0.12 for $v \sin i$ and imply the absence of a linear correlation between C/O and $\log g$ and between C/O and $v \sin i$. We do point out that for some stars the O abundance could not be determined precisely, and this could be the reason why no correlation is found.

Microscopic atomic diffusion can also alter surface abundances in stars (Michaud et al. 2015). It influences the Mg/Fe ratio in such a way that it becomes higher when gravitational settling is dominant, because Mg, with its lower atomic mass, settles slower than Fe. For fast rotators, it is assumed that the atomic diffusion process is counteracted by rotational mixing, but this assumption has been questioned lately, particularly for stars in the γ Dor mass regime. Indeed, for the hottest F-type dwarfs, radiative levitation comes into play as dominant mixing effect (Deal et al. 2020). This atomic diffusion process already occurs early during the main sequence and affects the surface abundances at later evolutionary phases. This is important for the chemical tagging of evolved stars, where surface abundances are used to identify members of dispersed clusters by assuming they were formed from the same cloud (Freeman & Bland-Hawthorn 2002; Dotter et al. 2017). Without internal mixing

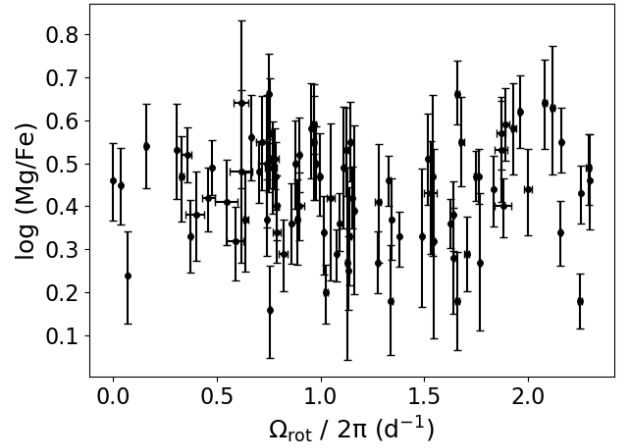


Fig. 14. Log (Mg/Fe) as a function of $\Omega_{\text{rot}}/2\pi$ for the sample of γ Dor stars.

of the chemical elements, these stars must have the same composition. However, this is not the case if atomic diffusion or other mixing processes have occurred in the stellar interior since they were born. As shown by Dotter et al. (2017), the mixing processes due to atomic diffusion must be included in stellar evolution models and calibrated with observed abundances to obtain the initial bulk abundances of evolved stars. Such a calibration can be done from abundance studies of their progenitors, among which F-type dwarfs.

Mombarg et al. (2020) compared measured asteroseismic parameters and surface abundances of two slowly rotating F-type dwarfs by means of models with and without atomic diffusion including radiative levitation. They found that precise abundance values with uncertainties below 0.1 dex are needed to assess internal mixing due to atomic diffusion. Only our values of Fe and Mg (and for some stars C and Ti) comply with this requirement. In Fig. 14, we plot the Mg/Fe ratio of the γ Dor stars as a function of $\Omega_{\text{rot}}/2\pi$, with Ω_{rot} the near-core angular rotation frequency determined from asteroseismic modelling by Van Reeth et al. (2018, 2016) and Li et al. (2020). This quantity is not dependent on the unknown inclination angle nor on the radius of the star. It offers a direct measurement of the internal rotation rate in the near-core convective boundary layer as estimated from high-order g modes (Aerts et al. 2019). We expect to see an enhancement of Mg/Fe for slow rotators in the absence of rotational mixing, but this is not observed. We thus do not find any observational evidence of mixing due to gravitational settling in our spectroscopic analysis of the γ Dor stars. This is in agreement with the low levels of deep mixing at the bottom of the radiative envelope, adjacent to the overshoot zone (hereafter called bottom envelope mixing), with values below $10 \text{ cm}^2 \text{ s}^{-1}$ found from asteroseismology for these pulsators, which cover a wide range of rotational velocities (Van Reeth et al. 2016).

For the SPB stars, we determined N abundances. In Fig. 15, we show the N abundance in 12 scale plotted as a function of $v \sin i$, and in Fig. 16 $v \sin i$ is replaced by the asteroseismic value of $\Omega_{\text{rot}}/2\pi$. These asteroseismic estimates are taken from Pedersen et al. (2021). The Pearson correlation coefficients for both diagrams are 0.26 and -0.05 for $v \sin i$ and $\Omega_{\text{rot}}/2\pi$, respectively. This confirms what can be seen by eye, namely there is no correlation between the N abundance at the stellar surface and the rotation frequency of the stars, which is in line with the earlier findings by Aerts et al. (2014). However, we do find evidence that deep mixing is active in the SPB stars from abundance ratios. As can be seen in Fig. 17, there is a positive trend

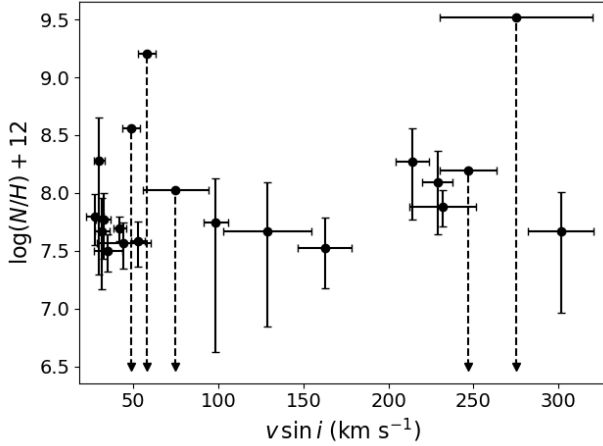


Fig. 15. N abundance of SPB stars in 12 scale plotted as a function of $v \sin i$.

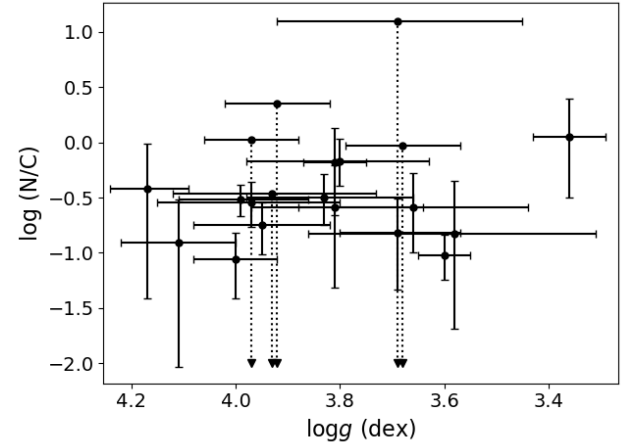


Fig. 18. Log (N/C) as a function of log g for the sample of SPB stars.

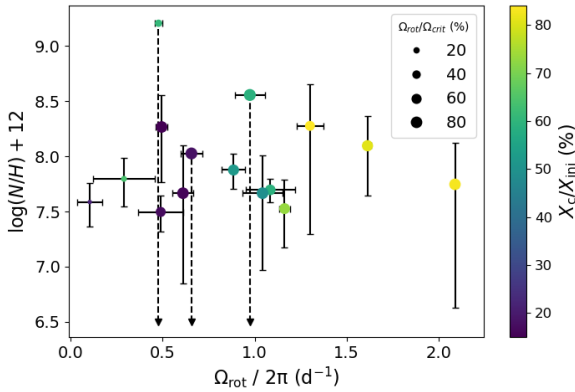


Fig. 16. N abundance of SPB stars in 12 scale plotted as a function of the asteroseismic $\Omega_{\text{rot}}/2\pi$. The stars are coloured according to their ratio of central-to-initial hydrogen mass fraction, which is a proxy for their age. The size of the points depends on the fraction of the rotation rate with respect to the critical rate.

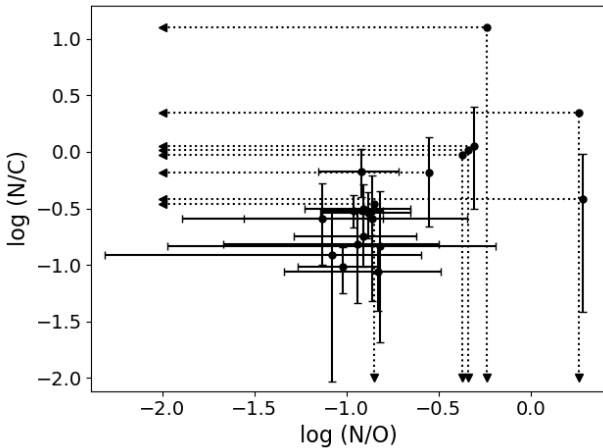


Fig. 17. Log (N/C) as a function of log (N/O) for the sample of SPB stars.

between N/C and N/O. This is confirmed by the Pearson correlation coefficient of 0.66. This is compatible with nucleosynthesis and element transportation of the resulting CNO products to the surface. The correlation with evolutionary state in Fig. 18 is also present but less clear, with a Pearson correlation coefficient of 0.19. Our spectroscopic findings are in good agreement

with the asteroseismic results of Pedersen et al. (2021), who find a correlation between the level of mixing at the bottom of the radiative envelope and the star's $\Omega_{\text{rot}}/\Omega_{\text{crit}}$ at that position, with Ω_{crit} being the critical rotation rate. The correlation coefficient between these two quantities measured from asteroseismology amounts to 0.60.

We also compared the abundances of the pulsating γ Dor and SPB stars with values for non-pulsating F- and B-type stars in Fig. 19, where all the sources of the literature data are listed in the figure caption. Except for Si and Fe, which appear to be less abundant in the SPB stars, the abundances of non-pulsators and pulsators are in agreement within the uncertainties. Thus from their surface abundances, there is no evidence that pulsating stars experience more mixing than non-pulsating stars. This was also found by Kahraman Aliçavuş et al. (2016).

In conclusion, we find that F-type g -mode pulsators do not reveal any evidence of a connection between rotation and bottom envelope internal mixing, nor any sign of gravitational settling in their envelope. On the other hand, the surface abundances of B-type g -mode pulsators are compatible with CNO processed matter being transported to the surface via mixing process(es) that are mildly correlated with the internal rotation.

6. Conclusion

We determined stellar parameters and surface abundances for a sample of 91 γ Dor stars, among which 14 are hybrid γ Dor - δ Sct pulsators, and 20 SPB stars that were selected based on their asteroseismic properties. To analyse all the stars in a homogeneous way, we relied on spectra assembled with a single high-resolution spectrograph (HERMES, Raskin et al. 2011), and we used a machine-learning tool (The Payne, Ting et al. 2019) for stellar parameter determination, which includes the pseudo-continuum normalisation of spectra. We performed tests for this method, and it was the first time it was applied to high-resolution spectroscopic data ($R \sim 85\,000$). It was found that the size of the training sample is dependent on the parameter ranges that have to be covered, but it is still reasonably small for 5D grids for γ Dor and SPB stars. Ideally, abundances must be optimised alongside stellar parameters to account for correlations between them, but this requires larger training samples that have almost impossibly long computation times. In future work, we will explore ways to circumvent this and analyse stellar parameters and surface abundances simultaneously. The performance of the NN method was tested against artificial data and benchmark stars for which

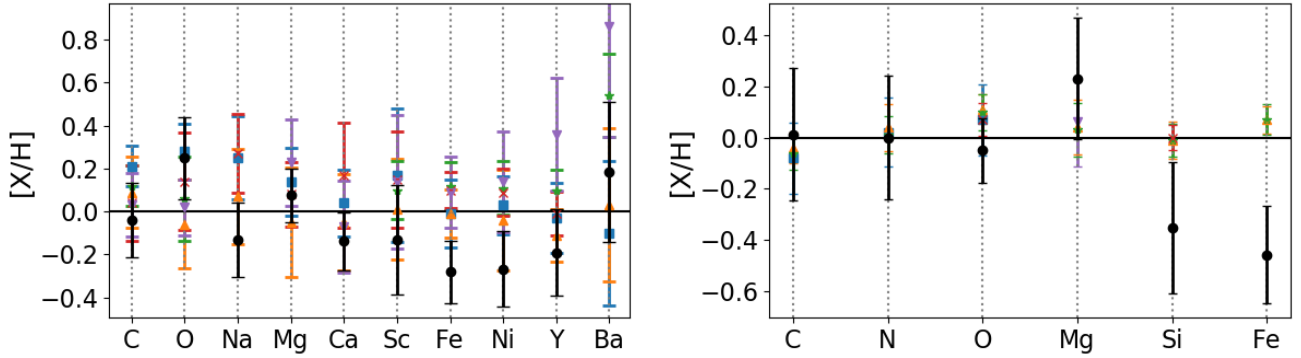


Fig. 19. *Left:* comparison of the mean element abundances from the γ Dor sample (black dots) with abundance values for non-pulsating stars from Varenne & Monier (1999; blue squares), Monier (2005; orange triangles), Gebran et al. (2008; green stars), Gebran et al. (2010; red crosses), and Kılıçoğlu et al. (2016; purple reversed triangles). *Right:* comparison of the mean element abundances from the SPB sample (black dots) with abundance values for non-pulsating stars from Lyubimkov et al. (2005; purple reversed triangles), Simón-Díaz (2010; red crosses), Nieva & Simón-Díaz (2011; orange triangles), Nieva & Przybilla (2012; green stars), and Lyubimkov et al. (2013; blue squares).

it determined accurate and precise stellar parameters that agree with the synthetic parameters and literature values. We applied the tested NN routine to the sample of γ Dor and SPB stars. $v \sin i$ was found to be consistent with values from literature studies, but T_{eff} and $\log g$ deviate a little, and $[M/H]$ is even systematically offset by ~ 0.2 dex for the F-type stars. We attribute the differences between values in this work and those in the literature for the F-type dwarfs to the differing normalisation of the spectra. Normalisation in literature studies is typically done manually and therefore depends on the continuum points that are selected, while in this work normalisation was integrated into the fitting routine as additional coefficients that were optimised alongside the stellar parameters. The $[M/H] \sim 0.2$ dex difference is likely a manifestation of the degeneracy between (T_{eff} , $\log g$, $[M/H]$) and normalisation, making it impossible to say with certainty which solution is correct. This must be investigated further for a large sample of F-type stars for which literature values from non-spectroscopic studies, such as interferometry, are available.

The surface abundances were determined individually with the LTE code GSSP (Tkachenko 2015). The blending of lines was accounted for by iterating the elements with the most lines twice. The uncertainties obtained for the abundances depend on the S/N of the spectra. Results for spectra with $S/N < 50$ should be taken with caution when studied individually, but they are reasonable in sample studies since they did not appear as outliers in the sample. Our analysis does not take non-LTE effects into account. This becomes increasingly important for the stellar parameters of hotter B-type stars, but it was omitted here in order to achieve an analogous analysis for the F- and B-type pulsators. In future work, we will increase the sample sizes and analyse the spectra based on a non-LTE approach.

We found no signatures of internal mixing from the CNO abundances for the F-type stars, nor did we detect consequences of gravitational settling. For the B-type stars, we did find consequences of internal mixing in the N/C and N/O ratios, but the abundance errors of N are too large to reveal effects of internal mixing. We also know from the asteroseismology of a sample of 26 SPB stars, 20 of which were included here, that the level of internal mixing at the bottom of the radiative envelope is mildly correlated with the near-core rotation of the stars (Pedersen et al. 2021). This correlation provides observational evidence that B stars have deep envelope mixing related to their rotation. Pedersen et al. (2021) further investigated the internal mixing profiles and concluded that the envelope mixing profiles

are stratified for the majority of stars, and they are of a diverse nature for the 26 stars in their sample. Combining g -mode asteroseismic quantities that probe the bottom of the radiative envelope with high-precision surface abundances at the level of 0.1 dex or better constitutes a viable and promising route towards the better probing of internal mixing in intermediate- and high-mass stars. It would also be a great asset for better distinguishing among various candidate envelope mixing theories of B-type stars. This requires higher S/N spectra to increase the abundance precision of as many chemical elements as possible to exploit the maximum power of joint g -mode asteroseismology and high-resolution spectroscopy.

Acknowledgement. This work is based on observations obtained with the HERMES spectrograph, which is supported by the Research Foundation – Flanders (FWO), Belgium, the Research Council of KU Leuven, Belgium, the Fonds National de la Recherche Scientifique (F.R.S.-FNRS), Belgium, the Royal Observatory of Belgium, the Observatoire de Genève, Switzerland and the Thüringer Landessternwarte Tautenburg, Germany. The computational resources and services used in this work were provided by the VSC (Flemish Supercomputer Centre), funded by the Research Foundation – Flanders (FWO) and the Flemish Government. Part of the research leading to these results has received funding from the European Research Council (ERC) under the European Union’s Horizon 2020 research and innovation programme (grant agreement N°670519: MAM-SIE), from the KU Leuven Research Council (grant C16/18/005: PARADISE) and from the Research Foundation Flanders (FWO) under grant agreement G0H5416N (ERC Runner Up Project). S.G., T.V.R., and D.M.B. gratefully acknowledge support from the Research Foundation Flanders (FWO) by means of a PhD Aspirant mandate and a Junior and Senior Postdoctoral Fellowship, under contracts No. 11E5620N, No. 12ZB620N, and No. 1286521N, respectively. MGP acknowledges support from the National Science Foundation under Grant No. NSF PHY-1748958. J.B. acknowledges support from the FWO Odysseus program under project No. G0F8H6N. We acknowledge the efforts of all observers who contributed to the gathering of the HERMES spectroscopy used in this paper and we are particularly grateful to have been given access to unpublished spectra of KIC 6292398, KIC 7748238, KIC 7770282 and KIC 2168333 from HERMES programs 52 and 86 prior to publication.

References

- Aerts, C. 2021, *Rev. Mod. Phys.*, **93**, 015001
- Aerts, C., Christensen-Dalsgaard, J., & Kurtz, D. W. 2010, *Asteroseismology* (Springer Netherlands)
- Aerts, C., Molenberghs, G., Kenward, M. G., & Neiner, C. 2014, *ApJ*, **781**, 88
- Aerts, C., Van Reeth, T., & Tkachenko, A. 2017, *ApJ*, **847**, L7
- Aerts, C., Molenberghs, G., Michielsen, M., et al. 2018, *ApJS*, **237**, 15
- Aerts, C., Mathis, S., & Rogers, T. M. 2019, *ARA&A*, **57**, 35
- Aguilera-Gómez, C., Ramírez, I., & Chanamé, J. 2018, *A&A*, **614**, A55
- Andrae, R., Fouesneau, M., Creevey, O., et al. 2018, *A&A*, **616**, A8
- Angelou, G. C., Bellinger, E. P., Hekker, S., et al. 2020, *MNRAS*, **493**, 4987

- Antoci, V., Cunha, M., Houdek, G., et al. 2014, *ApJ*, **796**, 118
- Asplund, M., Grevesse, N., & Sauval, A. J. 2005, in *Cosmic Abundances as Records of Stellar Evolution and Nucleosynthesis*, eds. I. Barnes, G. Thomas & F. N. Bash, Astronomical Society of the Pacific Conference Series, 336, 25
- Auvergne, M., Bodin, P., Boisdard, L., et al. 2009, *A&A*, **506**, 411
- Bailer-Jones, C. A. L., Rybizki, J., Fournesneau, M., Demleitner, M., & Andrae, R. 2021, *AJ*, **161**, 147
- Balona, L. A., Guzik, J. A., Uytterhoeven, K., et al. 2011a, *MNRAS*, **415**, 3531
- Balona, L. A., Pigulski, A., De Cat, P., et al. 2011b, *MNRAS*, **413**, 2403
- Balona, L. A., Baran, A. S., Daszyńska-Daszkiewicz, J., & De Cat, P. 2015, *MNRAS*, **451**, 1445
- Balona, L. A., Engelbrecht, C. A., Joshi, Y. C., et al. 2016, *MNRAS*, **460**, 1318
- Bellinger, E. P. 2019, *MNRAS*, **486**, 4612
- Bellinger, E. P. 2020, *MNRAS*, **492**, L50
- Bellinger, E. P., Angelou, G. C., Hekker, S., et al. 2016, *ApJ*, **830**, 31
- Blanco-Cuaresma, S., Soubiran, C., Heiter, U., et al. 2015, *A&A*, **577**, A47
- Boeche, C., & Grebel, E. K. 2016, *A&A*, **587**, A2
- Böhm-Vitense, E. 1958, *ZAp*, **46**, 108
- Bowman, D. M. 2020, *Front. Astron. Space Sci.*, **7**, 70
- Brott, I., Evans, C. J., Hunter, I., et al. 2011, *A&A*, **530**, A116
- Bruntt, H., De Cat, P., & Aerts, C. 2008, *A&A*, **478**, 487
- Christensen-Dalsgaard, J. 2002, *Rev. Mod. Phys.*, **74**, 1073
- Córsico, A. H., Althaus, L. G., Miller Bertolami, M. M., & Kepler, S. O. 2019, *Astron. Astrophys. Rev.*, **27**, 7
- Deal, M., Goupil, M. J., Marques, J. P., Reese, D. R., & Lebreton, Y. 2020, *A&A*, **633**, A23
- Degroote, P., Aerts, C., Baglin, A., et al. 2010, *Nature*, **464**, 259
- Dotter, A., Conroy, C., Cargile, P., & Asplund, M. 2017, *ApJ*, **840**, 99
- Dupret, M. A., Grigahcène, A., Garrido, R., Gabriel, M., & Scuflaire, R. 2005, *A&A*, **435**, 927
- Dziembowski, W. A., Moskalik, P., & Pamyatnykh, A. A. 1993, *MNRAS*, **265**, 588
- Flower, P. J. 1996, *ApJ*, **469**, 355
- Frasca, A., Molenda-Żakowicz, J., De Cat, P., et al. 2016, *A&A*, **594**, A39
- Freeman, K., & Bland-Hawthorn, J. 2002, *ARA&A*, **40**, 487
- García, R. A., & Ballot, J. 2019, *Living Rev. Solar Phys.*, **16**, 4
- Gebran, M., Monier, R., & Richard, O. 2008, *A&A*, **479**, 189
- Gebran, M., Vick, M., Monier, R., & Fossati, L. 2010, *A&A*, **523**, A71
- Giribaldi, R. E., Ubaldo-Melo, M. L., Porto de Mello, G. F., et al. 2019, *A&A*, **624**, A10
- Grassitelli, L., Fossati, L., Langer, N., et al. 2015, *A&A*, **584**, A2
- Gray, D. F. 2005, *The Observation and Analysis of Stellar Photospheres*
- Gray, R. O., Corbally, C. J., Garrison, R. F., McFadden, M. T., & Robinson, P. E. 2003, *AJ*, **126**, 2048
- Green, G. M., Schlafly, E., Zucker, C., Speagle, J. S., & Finkbeiner, D. 2019, *ApJ*, **887**, 93
- Guzik, J. A., Kaye, A. B., Bradley, P. A., Cox, A. N., & Neuforge, C. 2000, *ApJ*, **542**, L57
- Hanes, R. J., Waskie, S., Labadie-Bartz, J. M., et al. 2019, *AJ*, **157**, 129
- Hekker, S., & Christensen-Dalsgaard, J. 2017, *A&ARv*, **25**, 1
- Hunter, I., Brott, I., Lennon, D. J., et al. 2008, *ApJ*, **676**, L29
- Hunter, I., Brott, I., Langer, N., et al. 2009, *A&A*, **496**, 841
- Johnston, C., Tkachenko, A., Aerts, C., et al. 2019, *MNRAS*, **482**, 1231
- Kahraman Aliçavuş, F., Niemczura, E., De Cat, P., et al. 2016, *MNRAS*, **458**, 2307
- Kahraman Aliçavuş, F., Poretti, E., Catanzaro, G., et al. 2020, *MNRAS*, **493**, 4518
- Kılıçoğlu, T., Monier, R., Richer, J., Fossati, L., & Albayrak, B. 2016, *AJ*, **151**, 49
- Kobulnicky, H. A., Kiminki, D. C., Lundquist, M. J., et al. 2014, *ApJS*, **213**, 34
- Kovalev, M., Bergemann, M., Ting, Y.-S., & Rix, H.-W. 2019, *A&A*, **628**, A54
- Kurtz, D. W., Saio, H., Takata, M., et al. 2014, *MNRAS*, **444**, 102
- Kurucz, R. L. 1992, in *The Stellar Populations of Galaxies*, eds. B. Barbuy, & A. Renzini 149, 225
- Lampens, P., Frémat, Y., Vermeylen, L., et al. 2018, *A&A*, **610**, A17
- Langer, N. 2012, *ARA&A*, **50**, 107
- Lanz, T., & Hubeny, I. 2007, *ApJS*, **169**, 83
- Lebreton, Y., & Goupil, M. J. 2014, *A&A*, **569**, A21
- Lee, U., & Saio, H. 1987, *MNRAS*, **224**, 513
- Lehmann, H., Tkachenko, A., Semaan, T., et al. 2011, *A&A*, **526**, A124
- Li, G., Van Reeth, T., Bedding, T. R., et al. 2020, *MNRAS*, **491**, 3586
- Luck, R. E. 2017, *AJ*, **153**, 21
- Lyubimkov, L. S., Rostopchin, S. I., Rachkovskaya, T. M., Poklad, D. B., & Lambert, D. L. 2005, *MNRAS*, **358**, 193
- Lyubimkov, L. S., Lambert, D. L., Poklad, D. B., Rachkovskaya, T. M., & Rostopchin, S. I. 2013, *MNRAS*, **428**, 3497
- Maeder, A., & Meynet, G. 2000, *ARA&A*, **38**, 143
- Maeder, A., Przybilla, N., Nieva, M.-F., et al. 2014, *A&A*, **565**, A39
- Martins, F., Hervé, A., Bouret, J. C., et al. 2015, *A&A*, **575**, A34
- Mathis, S. 2009, *A&A*, **506**, 811
- Mazumdar, A., Monteiro, M. J. P. F. G., Ballot, J., et al. 2014, *ApJ*, **782**, 18
- Michaud, G., Alecian, G., & Richer, J. 2015, *Atomic Diffusion in Stars* (Springer International Publishing Switzerland)
- Mombarg, J. S. G., Van Reeth, T., Pedersen, M. G., et al. 2019, *MNRAS*, **485**, 3248
- Mombarg, J. S. G., Dotter, A., Van Reeth, T., et al. 2020, *ApJ*, **895**, 51
- Monier, R. 2005, *A&A*, **442**, 563
- Montgomery, M. H., & O'Donoghue, D. 1999, *Delta Scuti Star Newslett.*, **13**, 28
- Moravveji, E., Aerts, C., Pápics, P. I., Triana, S. A., & Vandoren, B. 2015, *A&A*, **580**, A27
- Moravveji, E., Townsend, R. H. D., Aerts, C., & Mathis, S. 2016, *ApJ*, **823**, 130
- Morel, T., Hubrig, S., & Briquet, M. 2008, *A&A*, **481**, 453
- Murphy, S. J., Fossati, L., Bedding, T. R., et al. 2016, *MNRAS*, **459**, 1201
- Murphy, S. J., Moe, M., Kurtz, D. W., et al. 2018, *MNRAS*, **474**, 4322
- Neiner, C., Floquet, M., Samadi, R., et al. 2012, *A&A*, **546**, A47
- Ness, M., Hogg, D. W., Rix, H. W., Ho, A. Y. Q., & Zasowski, G. 2015, *ApJ*, **808**, 16
- Niemczura, E., Morel, T., & Aerts, C. 2009, *A&A*, **506**, 213
- Niemczura, E., Murphy, S. J., Smalley, B., et al. 2015, *MNRAS*, **450**, 2764
- Niemczura, E., Políńska, M., Murphy, S. J., et al. 2017, *MNRAS*, **470**, 2870
- Nieva, M. F., & Przybilla, N. 2007, *A&A*, **467**, 295
- Nieva, M. F., & Przybilla, N. 2012, *A&A*, **539**, A143
- Nieva, M. F., & Simón-Díaz, S. 2011, *A&A*, **532**, A2
- Ouazzani, R.-M., Salmon, S. J. A. J., Antoci, V., et al. 2017, *MNRAS*, **465**, 2294
- Pápics, P. I., Briquet, M., Baglin, A., et al. 2012, *A&A*, **542**, A55
- Pápics, P. I., Tkachenko, A., Aerts, C., et al. 2013, *A&A*, **553**, A127
- Pápics, P. I., Tkachenko, A., Aerts, C., et al. 2015, *ApJ*, **803**, L25
- Pápics, P. I., Tkachenko, A., Van Reeth, T., et al. 2017, *A&A*, **598**, A74
- Pedersen, M. G., Aerts, C., Pápics, P. I., & Rogers, T. M. 2018, *A&A*, **614**, A128
- Pedersen, M. G., Escorza, A., Pápics, P. I., & Aerts, C. 2020, *MNRAS*, **495**, 2738
- Pedersen, M. G., Aerts, C., Pápics, P. I., et al. 2021, *Nat. Astron.*, in press
- Preston, G. W. 1974, *ARA&A*, **12**, 257
- Przybilla, N., Nieva, M.-F., & Butler, K. 2008, *ApJ*, **688**, L103
- Przybilla, N., Firnstein, M., Nieva, M. F., Meynet, G., & Maeder, A. 2010, *A&A*, **517**, A38
- Przybilla, N., Nieva, M.-F., & Butler, K. 2011, in *J. Phys. Conf. Ser.*, **328**, 012015
- Qian, S.-B., Li, L.-J., He, J.-J., et al. 2019, *Res. Astron. Astrophys.*, **19**, 001
- Raskin, G., van Winckel, H., Hensberger, H., et al. 2011, *A&A*, **526**, A69
- Saffe, C., & Levato, H. 2014, *A&A*, **562**, A128
- Saio, H., Kurtz, D. W., Takata, M., et al. 2015, *MNRAS*, **447**, 3264
- Salmon, S. J. A. J., Montalbán, J., Reese, D. R., Dupret, M. A., & Eggenberger, P. 2014, *A&A*, **569**, A18
- Shulyak, D., Tsymbal, V., Ryabchikova, T., Stütz, C., & Weiss, W. W. 2004, *A&A*, **428**, 993
- Silva Aguirre, V., Lund, M. N., Antia, H. M., et al. 2017, *ApJ*, **835**, 173
- Simón-Díaz, S. 2010, *A&A*, **510**, A22
- Simón-Díaz, S., Godart, M., Castro, N., et al. 2017, *A&A*, **597**, A22
- Sobol, I. M. 1967, *USSR Comp. Math. Math. Phys.*, **7**, 86
- Szewczuk, W., & Daszyńska-Daszkiewicz, J. 2017, *MNRAS*, **469**, 13
- Szewczuk, W., & Daszyńska-Daszkiewicz, J. 2018, *MNRAS*, **478**, 2243
- Ting, Y.-S., Conroy, C., Rix, H.-W., & Cargile, P. 2019, *ApJ*, **879**, 69
- Tkachenko, A. 2015, *A&A*, **581**, A129
- Tkachenko, A., Lehmann, H., Smalley, B., Debusscher, J., & Aerts, C. 2012, *MNRAS*, **422**, 2960
- Tkachenko, A., Aerts, C., Yakushechkin, A., et al. 2013, *A&A*, **556**, A52
- Tonry, J., & Davis, M. 1979, *AJ*, **84**, 1511
- Torres, G. 2010, *AJ*, **140**, 1158
- Townsend, R. H. D. 2003, *MNRAS*, **340**, 1020
- Tsymbal, V. 1996, in *M.A.S.S., Model Atmospheres and Spectrum Synthesis*, eds. S. J. Adelman, F. Kupka, & W. W. Weiss, Astronomical Society of the Pacific Conference Series, 108, 198
- Van Reeth, T., Tkachenko, A., Aerts, C., et al. 2015, *ApJS*, **218**, 27
- Van Reeth, T., Tkachenko, A., & Aerts, C. 2016, *A&A*, **593**, A120
- Van Reeth, T., Mombarg, J. S. G., Mathis, S., et al. 2018, *A&A*, **618**, A24
- Varenne, O., & Monier, R. 1999, *A&A*, **351**, 247
- Verma, K., Raodeo, K., Basu, S., et al. 2019, *MNRAS*, **483**, 4678
- Viani, L. S., Basu, S., Ong, J., M. J., Bonaca, A., & Chaplin, W. J. 2018, *ApJ*, **858**, 28
- Wu, T., & Li, Y. 2019, *ApJ*, **881**, 86
- Wu, T., Li, Y., Deng, Z.-m., et al. 2020, *ApJ*, **899**, 38
- Xiang, M., Ting, Y.-S., Rix, H.-W., et al. 2019, *ApJS*, **245**, 34
- Zhao, G., Zhao, Y.-H., Chu, Y.-Q., Jing, Y.-P., & Deng, L.-C. 2012, *Res. Astron. Astrophys.*, **12**, 723
- Zhang, C., Liu, C., Wu, Y., et al. 2018, *ApJ*, **854**, 168
- Zorec, J., & Royer, F. 2012, *A&A*, **537**, A120

Appendix A: Observational logs

Information about the observations of the γ Dor and SPB stars is given in Tables A.1 and A.2, including S/N values and RVs.

Table A.1. Observation log of the γ Dor stars.

KIC	N	Observation times	S/N	RV (km s ⁻¹)
2 575 161	3	2019	160	-9.3 ± 0.8
2 710 594	4	2011	80	-37 ± 2
2 846 358	4	2017	70	2.7 ± 0.8
3 331 147	3	2019	115	-20.0 ± 0.9
3 448 365	4	2011, 2014	205	-30 ± 2
3 626 325	3	2019	65	-24 ± 1
3 648 936	3	2019	110	2 ± 2
3 744 571	4	2013	35	-23 ± 1
3 942 392	3	2012	170	-28.8 ± 0.9
4 255 166	3	2019	80	-25.6 ± 0.8
4 567 531	3	2019	85	-29 ± 2
4 659 837	2	2019	40	SB1
4 757 184	4	2011	60	-24.7 ± 0.8
4 846 809	3	2013	25	0 ± 1
5 018 590	4	2012	150	-19 ± 2
5 113 797	2	2011	170	15 ± 3
5 114 382	4	2011	40	15 ± 2
5 450 503	3	2019	115	-23 ± 2
5 522 154	3	2011	105	-24 ± 3
5 646 058	3	2019	55	-10 ± 2
5 708 550	4	2011	75	-15 ± 2
5 788 623	4	2013	45	-4 ± 2
5 887 983	3	2019	60	-9 ± 3
5 954 264	2	2010	185	-33.0 ± 0.8
6 064 932	2	2019	60	-3.5 ± 0.8
6 131 093	4	2017	110	5.6 ± 0.7
6 292 398	8	2011–2020	105	SB1 ^(a)
6 301 745	3	2019	100	-39 ± 4
6 468 146	7	2011, 2014, 2019	225	SB1 ^(b)
6 468 987	4	2013, 2014	30	-27.6 ± 0.7
6 519 869	2	2011	85	2.5 ± 0.3
6 678 174	4	2011	60	-13.6 ± 0.9
6 935 014	5	2011	80	-9 ± 1
6 953 103	4	2013, 2014	30	7 ± 2
7 023 122	4	2011	100	-18.1 ± 0.8
7 215 607	2	2019	90	7.4 ± 0.3
7 365 537	3	2011	170	-30 ± 2
7 380 501	4	2011	40	-6 ± 1
7 434 470	4	2013	35	SB1 ^(c)
7 583 663	3	2013, 2014	30	-29 ± 4
7 661 054	4	2012	95	-17.8 ± 0.2
7 694 191	4	2019	80	SB1
7 939 065	4	2013	45	-22 ± 3
8 123 127	3	2019	60	2 ± 2
8 197 761	13	2015	100	SB1 ^(d)
8 355 130	2	2010	105	9.4 ± 0.6
8 364 249	4	2011	50	-23 ± 4
8 375 138	4	2011	90	-4 ± 2
8 651 452	3	2019	80	-16 ± 3
8 871 304	16	2010	195	SB1
9 210 943	5	2011, 2014	80	-28 ± 3
9 419 182	4	2011, 2019	115	0 ± 2
9 480 469	4	2013, 2014	30	-18 ± 3
9 490 067	2	2017	40	-0.6 ± 0.2
9 595 743	4	2013	50	-9 ± 1
9 716 358	4	2009	60	6.1 ± 0.4
9 962 653	19	2017, 2019	215	SB1

Table A.1. continued.

KIC	N	Observation times	S/N	RV (km s ⁻¹)
10 224 094	4	2011	50	-7.2 ± 0.5
10 256 787	13	2012, 2013, 2014	50	6 ± 1
10 317 467	3	2019	110	6.9 ± 0.4
10 467 146	4	2013, 2014	35	SB1 ^(b)
10 470 294	3	2019	70	-17 ± 7
11 080 103	4	2013, 2014	25	4 ± 1
11 099 031	4	2011	155	-17 ± 1
11 294 808	4	2011	55	-9 ± 2
11 456 474	4	2013, 2014	25	-11 ± 2
11 607 017	3	2019	40	-26 ± 4
11 612 274	2	2018	90	1 ± 2
11 721 304	4	2011	45	1.1 ± 0.7
11 826 272	11	2011, 2015, 2019	130	-9.6 ± 0.6
11 907 454	4	2011	70	SB1
11 917 550	4	2011	75	10 ± 2
11 920 505	13	2011, 2016, 2019	245	-25 ± 1
12 066 947	3	2011	115	9 ± 2
12 117 689	3	2019	95	-24 ± 6
12 458 189	4	2011	80	-35 ± 1
12 643 786	4	2011	55	1 ± 2
γ Dor- δ Sct hybrids				
2 168 333	8	2014–2020	150	-7 ± 6
3 241 199	3	2019	75	-6 ± 11
5 294 571	2	2017	50	-15 ± 10
5 608 334	3	2012	125	-17 ± 6
7 106 648	4	2018	135	-12 ± 4
7 748 238	6	2014	195	-23 ± 2
7 770 282	27	2011–2019	240	7 ± 1
7 977 996	4	2019, 2020	55	13 ± 11
8 645 874	5	2011, 2019	125	SB1
8 836 473	4	2013, 2014	25	-26 ± 1
9 651 065	2	2019	50	-22 ± 1
9 751 996	8	2011, 2019	50	-51.7 ± 0.2
11 754 232	12	2013, 2014	50	SB1 ^(b)
12 365 420	5	2019, 2020	35	7 ± 4
SB2, SB3 or higher order binaries				
3 222 854	10	2013, 2014, 2015		SB2 ^(b)
4 480 321	58	2011–2020		SB3 ^(e) (hybrid)
5 219 533	50	2010–2019		SB3 ^(e) (hybrid)
6 467 639	12	2013, 2014		SB3 ^(b) (hybrid)
6 764 812	3	2019		SB2
6 778 063	9	2013, 2014		SB3 ^(b) (hybrid)
7 385 783	3	2019		SB2
8 324 305	3	2011, 2019, 2020		SB2
8 975 515	32	2010–2020		SB2 ^(e)
10 080 943	25	2011, 2013, 2014		SB2 ^(f) (hybrid)
low S/N spectra				
5 254 203	4	2013, 2014	15	
7 746 984	2	2014	20	
9 533 489	3	2013, 2014	20	

Notes. *N* is the total number of spectra, and S/N is the combined signal-to-noise ratio in the continuum region between 5440 and 5442 Å. The last column contains the RV of single stars or the type of spectroscopic binary.

References. ^(a)Niemczura et al. (2015); ^(b)Van Reeth et al. (2015); ^(c)Li et al. (2020); ^(d)Murphy et al. (2018); ^(e)Lampens et al. (2018); ^(f)Tkachenko et al. (2013).

Table A.2. Observation log of the SPB stars.

KIC	N	Observation times	S/N	RV (km s ⁻¹)
3 240 411	6	2012, 2016, 2018	145	-37 ± 8
3 756 031	5	2012, 2016	90	11 ± 4
3 839 930	3	2010	175	-29 ± 1
3 865 742	3	2019	55	-12 ± 12
5 941 844	1	2016	110	-11 ± 2
6 462 033	1	2019	65	3.7 ± 0.7
6 780 397	10	2012	135	SB1
7 760 680	4	2012, 2014	140	-50 ± 2
8 057 661	6	2019	65	-36 ± 10
8 087 269	4	2013	50	96 ± 46
8 381 949	3	2010	100	-111 ± 10
8 459 899	122	2010	720	-10 ± 3
8 714 886	3	2010	90	25.0 ± 0.8
8 766 405	2	2010	180	43 ± 17
9 964 614	6	2010, 2016, 2017	80	-137 ± 4
10 285 114	4	2009, 2012	135	37 ± 19
10 536 147	5	2019	70	-18 ± 11
11 360 704	3	2010, 2012	105	-24 ± 13
11 971 405	5	2010, 2015	245	-27 ± 7
12 258 330	4	2010, 2017, 2018	170	-37 ± 7
SB2				
4 930 889	27	2010–2015		SB2 ^(a)
6 352 430	29	2010, 2011, 2012		SB2 ^(b)
low S/N spectra				
9 715 425	3	2019	20	

Notes. N is the total number of spectra, and S/N is the combined signal-to-noise ratio in the continuum region between 4960 and 4962 Å. The last column contains the RV of single stars or the type of spectroscopic binary.

References. ^(a)Pápics et al. (2017); ^(b)Pápics et al. (2013).

Appendix B: Test of the performance of the neural network

B.1. Size of the training sample

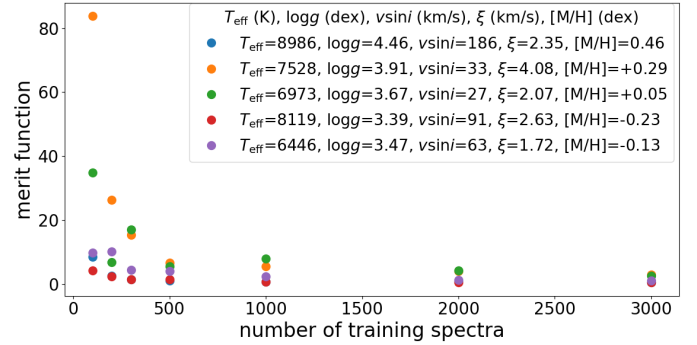


Fig. B.1. Difference between the spectrum predicted by the NN and the synthetic spectrum from GSSP as a function of the number of training spectra for γ Dor stars.

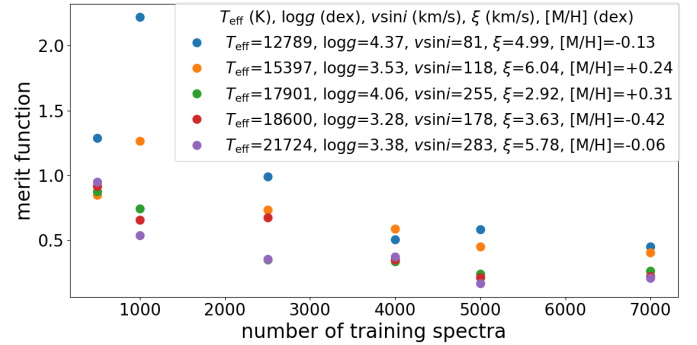


Fig. B.2. Difference between the spectrum predicted by the NN and the synthetic spectrum from GSSP as function of the number of training spectra for SPB stars.

In Figs. B.1 and B.2, we plot the difference between spectra predicted with the NN and synthetic spectra from GSSP for the same stellar parameters in function of the number of spectra used to train the NN. The start of the plateau indicates the optimal training size, which is 1000 and 5000 for γ Dor and SPB stars, respectively.

B.2. Comparison between three methods for parameter determination

Table B.1 summarises the results of the NN performance tests. It contains parameter values for ten synthetic spectra, four with parameters specific to SPB stars and six with typical γ Dor parameters. For each synthetic spectrum, we report the real values and values obtained with the three methods described in Sect. 3.2.3. Parameter values that deviate from the real value by more than the estimated uncertainties are shown in bold. But for most of them the difference is minimal.

Table B.1. Results of the NN performance tests.

Method	T_{eff} (K)	$\log g$ (dex)	[M/H] (dex)	$v \sin i$ (km s ⁻¹)	ξ (km s ⁻¹)
Real	16 500	4.0	-0.2	70	4.0
method 1	16728 ± 130	4.02 ± 0.03	-0.19 ± 0.06	72 ± 4	5 ± 1
method 2	16 521 ± 108	4.00 ± 0.02	-0.21 ± 0.02	69.8 ± 1.9	3.9 ± 0.5
method 3	16 424 ⁺¹³⁹ ₋₁₃₆	4.00 ± 0.04	-0.09^{+0.05} -0.06	71 ± 3	3.3 ^{+0.8} -0.7
Real	16 500	4.0	-0.2	170	4.0
method 1	16631 ± 110	4.00 ± 0.03	-0.22 ± 0.04	174 ± 7	4.6 ± 0.8
method 2	16 622 ⁺¹⁴² ⁻¹⁵⁶	4.00 ± 0.04	-0.24 ^{+0.06} -0.07	170 ± 5	4.0 ^{+1.3} -1.1
method 3	16 574 ⁺¹⁴⁹ ⁻¹⁷⁰	3.96 ± 0.05	-0.20 ± 0.06	171 ± 6	5.0 ^{+1.0} -1.1
Real	16 500	4.0	+0.4	70	4.0
method 1	16 485 ± 72	3.98 ± 0.02	+0.42 ± 0.02	75 ± 4	3.7 ± 0.4
method 2	16 503 ± 80	3.98 ± 0.02	+0.37 ± 0.03	69.6 ± 1.4	3.8 ± 0.3
method 3	16 493 ⁺¹⁵⁸ ⁻¹⁸⁴	3.95 ± 0.05	+0.42 ± 0.04	70.5 ± 1.8	4.3 ± 0.4
Real	16 500	4.0	+0.4	170	4.0
method 1	16 564 ± 84	3.99 ± 0.02	+0.38 ± 0.03	170 ± 5	4.2 ± 0.6
method 2	16 495 ⁺⁸⁸ ⁻⁸⁶	3.99 ± 0.03	+0.38 ± 0.04	170 ± 4	3.4 ^{+0.8} -0.3
method 3	16 539 ± 128	3.98 ± 0.04	+0.39 ^{+0.04} -0.05	170 ± 5	4.1 ^{+0.6} -0.5
Real	7100	4.0	-0.4	20	3.0
method 1	7144 ± 30	4.17 ± 0.02	-0.30 ± 0.03	19.6 ± 0.5	3.06 ± 0.09
method 2	7107 ± 15	3.93 ± 0.05	-0.38 ± 0.03	20.3 ± 0.7	3.15 ± 0.06
method 3	7065 ± 37	4.07 ± 0.04	-0.42 ± 0.02	20 ± 1	3.07^{+0.05} -0.06
Real	7100	4.0	-0.4	60	3.0
method 1	7117 ± 33	4.08 ± 0.03	-0.39 ± 0.02	59 ± 4	2.87 ± 0.07
method 2	7090 ± 13	4.07 ± 0.04	-0.42 ± 0.01	60.1 ± 0.4	3.03 ^{+0.05} -0.06
method 3	7097 ⁺¹⁴ ⁻¹⁵	4.11 ± 0.05	-0.41 ± 0.02	59.5 ± 0.4	2.88^{+0.06} -0.07
Real	7100	4.0	-0.4	120	3.0
method 1	7077 ± 37	3.97 ± 0.03	-0.40 ± 0.02	120 ± 1	2.9 ± 0.1
method 2	7094 ± 25	4.05 ± 0.06	-0.40 ± 0.02	119.8 ± 1.0	3.00 ^{+0.05} -0.06
method 3	7077 ± 28	4.17 ± 0.07	-0.48 ± 0.02	117 ± 3	2.96 ± 0.10
Real	7100	4.0	+0.2	20	3.0
method 1	7090 ± 19	4.09 ± 0.03	+0.17 ± 0.02	21.5 ± 0.5	3.3 ± 0.1
method 2	7100 ⁺⁹ ⁻¹⁰	4.04 ± 0.04	+0.19 ± 0.03	20.1 ± 0.9	3.05 ^{+0.05} -0.06
method 3	7112 ⁺¹⁴ ⁻¹⁵	3.99 ± 0.03	+0.19 ± 0.01	20.1 ± 0.2	2.97 ± 0.08
Real	7100	4.0	+0.2	60	3.0
method 1	7100 ± 14	3.96 ± 0.04	+0.20 ± 0.01	60 ± 2	2.99 ± 0.07
method 2	7102 ± 7	4.02 ± 0.03	+0.20 ± 0.01	60.1 ± 0.3	3.00 ^{+0.03} -0.04
method 3	7037 ⁺⁴¹ ⁻⁴⁰	3.97 ± 0.06	+0.10 ± 0.03	59.0 ± 1.2	3.09 ^{+0.14} -0.15
Real	7100	4.0	+0.2	120	3.0
method 1	7116 ± 25	4.07 ± 0.04	+0.19 ± 0.02	120 ± 1	3.14 ± 0.05
method 2	7089 ⁺¹⁴ ⁻¹⁵	4.15^{+0.05} -0.06	+0.17 ± 0.04	119.8 ^{+0.6} -0.7	3.09 ± 0.1
method 3	7097 ⁺¹⁵ ⁻¹⁶	4.11 ± 0.04	+0.11^{+0.04} -0.05	118 ± 2	3.07 ± 0.08

Notes. For ten synthetic spectra the real stellar parameter values are given together with the results from methods (1), (2) and (3) (see Sect. 3.2.3 for more information). Values that deviate from the actual value with (little) more than the uncertainty are marked in bold. The errors are approximately symmetric except when a different upper and lower bound are given.

Appendix C: Stellar parameters and surface abundances of the gamma Dor stars

The stellar parameters of the γ Dor stars are listed in Table C.1 while the surface abundances can be found in Tables C.2 and C.3.

Table C.1. Stellar parameters of the γ Dor stars.

KIC	$T_{\text{eff,NN}}$ (K)	$\log g_{\text{NN}}$ (dex)	$[M/H]_{\text{NN}}$ (dex)	$v \sin i_{\text{NN}}$ (km s ⁻¹)	ξ_{NN} (km s ⁻¹)	$T_{\text{eff,GSSP}}$ (K)	$\log g_{\text{GSSP}}$ (dex)	ξ_{GSSP} (km s ⁻¹)	$\log(L/L_{\odot})$
2 575 161	7019 ± 35	3.76 ± 0.10	-0.23 ± 0.04	78 ± 3	2.69 ± 0.19	7011 ⁺⁴⁷ ₋₄₉	3.76 ^{+0.16} _{-0.16}	2.64 ^{+0.15} _{-0.15}	0.93 ^{+0.02} _{-0.02}
2 710 594	6937 ± 40	3.41 ± 0.18	-0.27 ± 0.04	76 ± 2	3.06 ± 0.19	6916 ⁺⁵⁴ ₋₅₄	3.41 ^{+0.23} _{-0.22}	3.19 ^{+0.26} _{-0.23}	0.893 ^{+0.008} _{-0.006}
2 846 358	6880 ± 48	4.60 ± 0.11	-0.18 ± 0.04	37 ± 2	1.87 ± 0.23	6797 ⁺⁷⁴ ₋₇₆	4.47 ^{+0.19} _{-0.21}	1.63 ^{+0.23} _{-0.25}	0.73 ^{+0.13} _{-0.09}
3 331 147	7130 ± 32	4.07 ± 0.10	-0.16 ± 0.03	62 ± 2	2.75 ± 0.16	7123 ⁺⁴⁸ ₋₄₉	3.96 ^{+0.17} _{-0.17}	2.83 ^{+0.17} _{-0.15}	0.660 ^{+0.004} _{-0.006}
3 448 365	7065 ± 30	3.98 ± 0.08	-0.07 ± 0.04	86 ± 2	2.96 ± 0.17	7079 ⁺⁴² ₋₄₁	4.11 ^{+0.13} _{-0.15}	3.01 ^{+0.12} _{-0.13}	0.767 ^{+0.002} _{-0.003}
3 626 325	7036 ± 49	3.94 ± 0.13	-0.11 ± 0.05	51 ± 2	2.78 ± 0.24	7006 ⁺⁶¹ ₋₆₁	4.01 ^{+0.19} _{-0.22}	2.71 ^{+0.20} _{-0.20}	0.763 ^{+0.006} _{-0.005}
3 648 936	6870 ± 40	3.20 ± 0.12	-0.35 ± 0.04	85 ± 3	3.34 ± 0.16	6791 ⁺⁴⁰ ₋₃₉	3.07 ^{+0.15} _{-0.17}	3.48 ^{+0.18} _{-0.18}	1.066 ^{+0.003} _{-0.003}
3 744 571	6987 ± 63	3.40 ± 0.21	-0.36 ± 0.06	51 ± 3	2.98 ± 0.31	6938 ⁺⁸² ₋₈₄	3.52 ^{+0.30} _{-0.32}	3.03 ^{+0.43} _{-0.33}	0.912^{+0.007}_{-0.006}
3 942 392	7025 ± 29	4.11 ± 0.08	-0.13 ± 0.03	80 ± 2	2.74 ± 0.15	7010 ⁺³⁴ ₋₃₆	4.13 ^{+0.12} _{-0.13}	2.58 ^{+0.12} _{-0.12}	0.677 ^{+0.003} _{-0.004}
4 255 166	7003 ± 44	3.98 ± 0.10	-0.06 ± 0.04	36 ± 2	2.64 ± 0.23	6980 ⁺⁵⁸ ₋₅₇	4.03 ^{+0.19} _{-0.19}	2.62 ^{+0.15} _{-0.18}	0.795 ^{+0.003} _{-0.004}
4 567 531	6802 ± 54	3.87 ± 0.13	-0.13 ± 0.07	93 ± 4	2.67 ± 0.35	6764 ⁺⁶² ₋₅₄	4.02 ^{+0.19} _{-0.22}	2.62 ^{+0.18} _{-0.24}	0.839 ^{+0.005} _{-0.005}
4 659 837	6903 ± 40	3.97 ± 0.09	-0.16 ± 0.04	7 ± 2	2.40 ± 0.15	6915 ⁺⁷³ ₋₇₂	4.28 ^{+0.20} _{-0.20}	2.45 ^{+0.26} _{-0.23}	0.777 ^{+0.01} _{-0.008}
4 757 184	7019 ± 51	3.43 ± 0.14	-0.65 ± 0.05	35 ± 5	2.70 ± 0.24	7031 ⁺⁶⁵ ₋₆₇	3.48 ^{+0.27} _{-0.24}	2.80 ^{+0.32} _{-0.22}	0.945 ^{+0.009} _{-0.008}
4 846 809	7151 ± 71	3.53 ± 0.25	-0.24 ± 0.07	50 ± 3	3.26 ± 0.35	7180 ⁺⁸⁶ ₋₈₈	3.90 ^{+0.27} _{-0.32}	3.53 ^{+0.35} _{-0.45}	0.718 ^{+0.008} _{-0.01}
5 018 590	7048 ± 28	4.00 ± 0.06	-0.20 ± 0.03	100 ± 3	2.74 ± 0.16	7073 ⁺³⁹ ₋₃₉	4.17 ^{+0.09} _{-0.10}	2.84 ^{+0.08} _{-0.09}	0.690 ^{+0.002} _{-0.003}
5 113 797	8118 ± 22	3.87 ± 0.07	-0.30 ± 0.03	114 ± 4	2.46 ± 0.18	8121 ⁺³⁸ ₋₃₈	3.76 ^{+0.10} _{-0.09}	2.83 ^{+0.19} _{-0.19}	1.51 ^{+0.02} _{-0.02}
5 114 382	7105 ± 53	4.13 ± 0.16	-0.25 ± 0.06	64 ± 5	2.65 ± 0.28	7094 ⁺⁷² ₋₇₂	4.18 ^{+0.25} _{-0.25}	2.61 ^{+0.30} _{-0.27}	0.966 ^{+0.009} _{-0.008}
5 450 503	6883 ± 40	4.05 ± 0.09	-0.21 ± 0.05	99 ± 4	2.72 ± 0.22	6868 ⁺⁵⁰ ₋₄₅	4.16 ^{+0.14} _{-0.15}	2.65 ^{+0.14} _{-0.15}	0.725 ^{+0.003} _{-0.002}
5 522 154	7054 ± 48	4.05 ± 0.08	-0.30 ± 0.05	163 ± 7	3.06 ± 0.22	7123 ⁺⁵⁰ ₋₅₆	4.03 ^{+0.18} _{-0.20}	2.96 ^{+0.23} _{-0.20}	0.637 ^{+0.003} _{-0.003}
5 646 058	7195 ± 61	3.76 ± 0.20	-0.13 ± 0.06	107 ± 5	3.65 ± 0.28	7217 ⁺⁶² ₋₆₅	3.81 ^{+0.27} _{-0.25}	3.81 ^{+0.34} _{-0.29}	1.001 ^{+0.006} _{-0.006}
5 708 550	6996 ± 43	4.09 ± 0.13	-0.18 ± 0.05	64 ± 4	2.59 ± 0.24	6980 ⁺⁶⁴ ₋₆₂	4.14 ^{+0.21} _{-0.21}	2.49 ^{+0.18} _{-0.22}	0.814 ^{+0.007} _{-0.006}
5 788 623	7151 ± 64	3.80 ± 0.14	-0.31 ± 0.06	21 ± 2	2.74 ± 0.26	7177 ⁺⁶⁹ ₋₆₇	4.16 ^{+0.20} _{-0.22}	2.90 ^{+0.21} _{-0.27}	0.832 ^{+0.007} _{-0.008}
5 887 983	6894 ± 48	3.20 ± 0.21	-0.24 ± 0.05	111 ± 5	3.29 ± 0.23	6879 ⁺⁵⁴ ₋₅₁	3.48 ^{+0.22} _{-0.22}	3.43 ^{+0.23} _{-0.26}	1.012 ^{+0.004} _{-0.004}
5 954 264	7079 ± 34	3.68 ± 0.09	-0.07 ± 0.03	104 ± 2	3.52 ± 0.15	7079 ⁺³⁵ ₋₃₃	3.71 ^{+0.13} _{-0.13}	3.65 ^{+0.14} _{-0.13}	1.05 ^{+0.03} _{-0.02}
6 064 932	6967 ± 45	3.47 ± 0.17	-0.43 ± 0.04	52 ± 2	2.87 ± 0.22	6929 ⁺⁶⁰ ₋₆₁	3.55 ^{+0.22} _{-0.22}	2.87 ^{+0.26} _{-0.23}	0.831 ^{+0.004} _{-0.004}
6 131 093	6936 ± 33	4.35 ± 0.11	-0.12 ± 0.06	45 ± 2	2.31 ± 0.26	6875 ⁺⁵⁴ ₋₅₄	4.34 ^{+0.14} _{-0.16}	1.94 ^{+0.13} _{-0.15}	0.908 ^{+0.007} _{-0.008}
6 292 398	7865 ± 42	3.52 ± 0.08	+0.07 ± 0.05	8 ± 2	3.38 ± 0.26	7864 ⁺³⁹ ₋₃₉	3.34 ^{+0.17} _{-0.16}	2.76 ^{+0.22} _{-0.22}	1.416 ^{+0.009} _{-0.008}
6 301 745	6968 ± 60	4.31 ± 0.10	-0.26 ± 0.06	182 ± 8	3.02 ± 0.30	6993 ⁺⁶³ ₋₆₀	4.37 ^{+0.18} _{-0.22}	3.14 ^{+0.28} _{-0.27}	0.552 ^{+0.004} _{-0.005}
6 468 146	7009 ± 23	3.05 ± 0.05	-0.33 ± 0.04	70 ± 2	3.94 ± 0.18	7014 ⁺²⁸ ₋₂₉	3.19 ^{+0.10} _{-0.10}	4.26 ^{+0.13} _{-0.13}	0.927 ^{+0.008} _{-0.007}
6 468 987	7036 ± 143	3.86 ± 0.80	-0.21 ± 0.14	120 ± 12	3.14 ± 0.83	7029 ⁺¹²⁵ ₋₁₂₇	4.01 ^{+0.52} _{-0.57}	3.03 ^{+0.72} _{-0.66}	0.967^{+0.008}_{-0.007}
6 519 869	7054 ± 26	3.40 ± 0.07	-0.30 ± 0.03	23 ± 1	2.87 ± 0.13	7085 ⁺⁴⁴ ₋₄₂	3.73 ^{+0.15} _{-0.15}	3.13 ^{+0.15} _{-0.16}	0.751 ^{+0.003} _{-0.003}
6 678 174	7064 ± 47	3.49 ± 0.16	-0.32 ± 0.04	46 ± 2	3.20 ± 0.23	7068 ⁺⁶⁰ ₋₆₂	3.77 ^{+0.20} _{-0.22}	3.38 ^{+0.23} _{-0.27}	0.928 ^{+0.006} _{-0.006}
6 935 014	7028 ± 33	3.83 ± 0.11	-0.11 ± 0.04	67 ± 2	2.94 ± 0.17	6996 ⁺⁴⁷ ₋₄₇	3.99 ^{+0.13} _{-0.13}	2.82 ^{+0.13} _{-0.12}	0.778 ^{+0.004} _{-0.003}
6 953 103	7135 ± 80	3.58 ± 0.28	-0.37 ± 0.08	48 ± 4	2.73 ± 0.42	7135 ⁺¹⁰¹ ₋₁₀₂	3.82 ^{+0.47} _{-0.38}	2.74 ^{+0.50} _{-0.41}	0.759^{+0.008}_{-0.007}
7 023 122	7209 ± 31	3.72 ± 0.13	-0.34 ± 0.03	51 ± 2	3.22 ± 0.16	7224 ⁺⁴⁴ ₋₄₅	3.71 ^{+0.16} _{-0.15}	3.30 ^{+0.17} _{-0.15}	0.755 ^{+0.004} _{-0.004}
7 215 607	6676 ± 57	4.01 ± 0.09	-0.26 ± 0.05	22 ± 1	0.51 ± 0.16	6705 ⁺⁷⁷ ₋₇₁	4.04 ^{+0.25} _{-0.23}	< 0.67	0.96 ^{+0.02} _{-0.02}
7 365 537	7233 ± 29	3.95 ± 0.08	-0.23 ± 0.03	148 ± 4	3.51 ± 0.15	7274 ⁺³⁹ ₋₃₈	4.02 ^{+0.12} _{-0.13}	3.59 ^{+0.15} _{-0.15}	0.734 ^{+0.002} _{-0.002}
7 380 501	6919 ± 58	3.64 ± 0.21	-0.21 ± 0.06	50 ± 3	2.77 ± 0.30	6880 ⁺⁶⁷ ₋₆₉	3.89 ^{+0.20} _{-0.24}	2.75 ^{+0.20} _{-0.27}	0.700 ^{+0.007} _{-0.007}
7 434 470	7012 ± 113	4.35 ± 0.46	-0.17 ± 0.11	131 ± 11	2.60 ± 0.59	7009 ⁺⁹⁷ ₋₉₆	4.30 ^{+0.38} _{-0.65}	2.59 ^{+0.48} _{-0.44}	0.661 ^{+0.008} _{-0.009}

Notes. The last column contains the luminosities computed from *V*-band magnitudes or, when indicated, using *G*-band (bold) or *Kepler* (italic) magnitudes.

Table C.1. continued.

KIC	$T_{\text{eff,NN}}$ (K)	$\log g_{\text{NN}}$ (dex)	$[M/H]_{\text{NN}}$ (dex)	$v \sin i_{\text{NN}}$ (km s ⁻¹)	ξ_{NN} (km s ⁻¹)	$T_{\text{eff,GSSP}}$ (K)	$\log g_{\text{GSSP}}$ (dex)	ξ_{GSSP} (km s ⁻¹)	$\log(L/L_{\odot})$
7 583 663	7042 ± 143	4.08 ± 0.69	-0.06 ± 0.14	98 ± 11	2.90 ± 0.74	7027 ⁺¹²⁰ ₋₁₂₈	4.19 ^{+0.45} _{-0.49}	2.86 ^{+0.61} _{-0.58}	0.80^{+0.02} _{-0.01}
7 661 054	6889 ± 25	3.27 ± 0.05	-0.21 ± 0.03	13 ± 2	3.08 ± 0.10	6874 ⁺⁵² ₋₅₃	3.29 ^{+0.13} _{-0.13}	3.15 ^{+0.11} _{-0.14}	0.84 ^{+0.03} _{-0.04}
7 694 191	7934 ± 44	3.39 ± 0.10	-0.10 ± 0.05	77 ± 3	2.81 ± 0.22	7997 ⁺⁵⁵ ₋₅₂	3.37 ^{+0.10} _{-0.09}	3.16 ^{+0.23} _{-0.21}	2.01 ^{+0.02} _{-0.02}
7 939 065	7125 ± 64	3.56 ± 0.30	-0.35 ± 0.06	88 ± 5	3.04 ± 0.27	7134 ⁺⁸³ ₋₈₂	3.74 ^{+0.34} _{-0.35}	3.09 ^{+0.47} _{-0.37}	0.934 ^{+0.007} _{-0.006}
8 123 127	7181 ± 45	3.63 ± 0.16	-0.25 ± 0.04	80 ± 3	3.43 ± 0.22	7192 ⁺⁵⁵ ₋₅₃	3.68 ^{+0.19} _{-0.21}	3.78 ^{+0.24} _{-0.25}	0.860 ^{+0.004} _{-0.005}
8 197 761	7070 ± 26	3.30 ± 0.05	-0.28 ± 0.03	11 ± 1	3.11 ± 0.11	7048 ⁺⁶² ₋₆₂	3.43 ^{+0.17} _{-0.17}	2.96 ^{+0.23} _{-0.19}	0.836 ^{+0.008} _{-0.007}
8 355 130	7151 ± 34	3.62 ± 0.12	-0.26 ± 0.03	49 ± 2	3.08 ± 0.16	7212 ⁺⁴¹ ₋₄₃	3.94 ^{+0.15} _{-0.16}	3.15 ^{+0.17} _{-0.17}	0.791 ^{+0.005} _{-0.004}
8 364 249	6958 ± 66	3.83 ± 0.14	-0.25 ± 0.06	133 ± 7	3.30 ± 0.30	6931 ⁺⁶² ₋₆₄	3.48 ^{+0.29} _{-0.24}	3.23 ^{+0.33} _{-0.23}	0.979^{+0.007} _{-0.006}
8 375 138	6979 ± 44	3.78 ± 0.11	-0.30 ± 0.04	131 ± 5	3.15 ± 0.20	6995 ⁺⁵⁰ ₋₅₀	3.76 ^{+0.15} _{-0.17}	3.16 ^{+0.18} _{-0.18}	0.787 ^{+0.004} _{-0.005}
8 651 452	7042 ± 48	3.96 ± 0.09	-0.14 ± 0.04	138 ± 5	3.10 ± 0.21	7026 ⁺⁴⁵ ₋₄₉	3.72 ^{+0.19} _{-0.18}	3.12 ^{+0.19} _{-0.19}	0.765 ^{+0.004} _{-0.003}
8 871 304	6945 ± 29	3.95 ± 0.06	-0.24 ± 0.04	90 ± 3	2.67 ± 0.18	6936 ⁺⁴⁷ ₋₄₇	4.02 ^{+0.12} _{-0.12}	2.45 ^{+0.09} _{-0.08}	0.752 ^{+0.005} _{-0.004}
9 210 943	7021 ± 58	4.28 ± 0.15	-0.14 ± 0.05	73 ± 3	2.96 ± 0.28	6992 ⁺⁶⁶ ₋₆₆	4.28 ^{+0.20} _{-0.22}	2.69 ^{+0.22} _{-0.23}	1.045 ^{+0.01} _{-0.009}
9 419 182	6906 ± 36	3.84 ± 0.07	-0.10 ± 0.04	109 ± 3	2.99 ± 0.16	6882 ⁺³⁹ ₋₃₈	3.87 ^{+0.13} _{-0.13}	3.02 ^{+0.12} _{-0.14}	0.813 ^{+0.005} _{-0.006}
9 480 469	7130 ± 133	3.78 ± 0.66	+0.01 ± 0.13	106 ± 11	2.93 ± 0.73	7112 ⁺¹¹⁸ ₋₁₁₈	3.91 ^{+0.51} _{-0.45}	3.00 ^{+0.60} _{-0.57}	1.166 ^{+0.009} _{-0.008}
9 490 067	6942 ± 111	4.11 ± 0.47	-0.06 ± 0.11	119 ± 8	2.83 ± 0.56	6918 ⁺¹⁰⁰ ₋₉₈	4.06 ^{+0.42} _{-0.35}	2.75 ^{+0.49} _{-0.46}	0.779 ^{+0.004} _{-0.004}
9 595 743	7146 ± 53	3.67 ± 0.20	-0.33 ± 0.05	48 ± 3	3.08 ± 0.27	7192 ⁺⁶⁰ ₋₆₀	4.01 ^{+0.19} _{-0.21}	3.03 ^{+0.24} _{-0.21}	0.745 ^{+0.006} _{-0.005}
9 716 358	7915 ± 33	3.99 ± 0.07	-0.10 ± 0.03	15 ± 2	3.66 ± 0.16	7664 ⁺⁶⁴ ₋₆₅	3.58 ^{+0.20} _{-0.22}	2.88 ^{+0.27} _{-0.26}	0.84^{+0.01} _{-0.01}
9 962 653	7092 ± 31	4.00 ± 0.06	-0.24 ± 0.03	139 ± 4	3.07 ± 0.14	7105 ⁺⁴⁵ ₋₄₅	3.95 ^{+0.12} _{-0.12}	3.14 ^{+0.13} _{-0.14}	0.767 ^{+0.003} _{-0.003}
10 224 094	6996 ± 40	3.57 ± 0.11	-0.30 ± 0.04	23 ± 1	2.89 ± 0.21	7009 ⁺⁵¹ ₋₅₂	3.89 ^{+0.17} _{-0.18}	2.90 ^{+0.18} _{-0.17}	0.54 ^{+0.03} _{-0.03}
10 256 787	7031 ± 45	4.24 ± 0.15	-0.14 ± 0.04	35 ± 2	2.79 ± 0.22	6995 ⁺⁶⁴ ₋₆₅	4.34 ^{+0.19} _{-0.20}	2.51 ^{+0.22} _{-0.20}	0.65 ^{+0.05} _{-0.06}
10 317 467	7133 ± 21	3.20 ± 0.04	-0.27 ± 0.02	25 ± 4	3.00 ± 0.10	7218 ⁺⁴⁷ ₋₄₉	3.58 ^{+0.17} _{-0.18}	3.38 ^{+0.21} _{-0.19}	1.23 ^{+0.02} _{-0.03}
10 467 146	6982 ± 82	3.24 ± 0.27	-0.44 ± 0.08	53 ± 4	2.72 ± 0.39	6913 ⁺⁹⁴ ₋₉₅	3.17 ^{+0.41} _{-0.41}	2.90 ^{+0.48} _{-0.45}	1.07^{+0.03} _{-0.02}
10 470 294	6972 ± 57	4.61 ± 0.13	-0.12 ± 0.05	140 ± 8	2.83 ± 0.25	6915 ⁺⁶⁴ ₋₆₅	4.44 ^{+0.22} _{-0.19}	2.73 ^{+0.29} _{-0.23}	0.729 ^{+0.007} _{-0.005}
11 080 103	7149 ± 113	3.56 ± 0.43	-0.41 ± 0.10	40 ± 8	3.08 ± 0.62	7096 ⁺¹¹⁹ ₋₁₁₇	3.83 ^{+0.45} _{-0.45}	3.10 ^{+0.62} _{-0.55}	0.82^{+0.01} _{-0.01}
11 099 031	6779 ± 30	3.96 ± 0.11	+0.17 ± 0.03	96 ± 3	2.43 ± 0.14	6777 ⁺⁴⁵ ₋₄₆	4.06 ^{+0.12} _{-0.14}	2.47 ^{+0.08} _{-0.09}	0.828 ^{+0.004} _{-0.004}
11 294 808	6898 ± 48	3.37 ± 0.21	-0.26 ± 0.04	81 ± 3	3.13 ± 0.23	6878 ⁺⁶⁴ ₋₆₆	3.54 ^{+0.23} _{-0.27}	3.20 ^{+0.25} _{-0.31}	0.978 ^{+0.006} _{-0.007}
11 456 474	7002 ± 95	3.77 ± 0.48	-0.27 ± 0.09	80 ± 3	2.99 ± 0.45	6964 ⁺¹¹⁴ ₋₁₀₆	3.91 ^{+0.46} _{-0.47}	2.92 ^{+0.53} _{-0.53}	0.892^{+0.007} _{-0.006}
11 607 017	7066 ± 78	4.02 ± 0.17	-0.19 ± 0.08	157 ± 12	3.42 ± 0.45	7084 ⁺⁷⁹ ₋₈₃	4.00 ^{+0.29} _{-0.37}	3.63 ^{+0.42} _{-0.48}	0.875^{+0.008} _{-0.005}
11 612 274	7063 ± 41	3.70 ± 0.16	-0.43 ± 0.04	132 ± 5	3.55 ± 0.20	7078 ⁺⁴⁵ ₋₄₂	3.76 ^{+0.17} _{-0.17}	3.83 ^{+0.21} _{-0.22}	0.943 ^{+0.006} _{-0.007}
11 721 304	7115 ± 48	3.87 ± 0.13	-0.19 ± 0.05	26 ± 1	2.73 ± 0.21	7100 ⁺⁵⁶ ₋₅₆	3.99 ^{+0.17} _{-0.19}	2.70 ^{+0.20} _{-0.17}	0.719^{+0.005} _{-0.005}
11 826 272	7015 ± 31	3.53 ± 0.11	-0.07 ± 0.03	32 ± 1	2.84 ± 0.16	6992 ⁺⁴¹ ₋₄₀	3.70 ^{+0.16} _{-0.13}	2.89 ^{+0.15} _{-0.15}	0.903 ^{+0.005} _{-0.005}
11 907 454	7009 ± 57	4.09 ± 0.13	-0.14 ± 0.06	104 ± 5	2.79 ± 0.29	7008 ⁺⁵³ ₋₅₅	4.14 ^{+0.18} _{-0.19}	2.63 ^{+0.19} _{-0.20}	0.536 ^{+0.005} _{-0.006}
11 917 550	7103 ± 34	3.83 ± 0.11	-0.13 ± 0.04	73 ± 2	3.01 ± 0.18	7107 ⁺⁵⁵ ₋₅₆	3.88 ^{+0.17} _{-0.18}	2.96 ^{+0.16} _{-0.18}	0.766 ^{+0.005} _{-0.005}
11 920 505	7146 ± 24	4.08 ± 0.07	-0.12 ± 0.02	55 ± 2	2.78 ± 0.11	7110 ⁺⁴⁶ ₋₄₆	3.81 ^{+0.15} _{-0.15}	2.92 ^{+0.14} _{-0.13}	0.694 ^{+0.002} _{-0.002}
12 066 947	7208 ± 34	3.85 ± 0.12	-0.31 ± 0.03	126 ± 4	3.58 ± 0.17	7233 ⁺⁴⁴ ₋₄₆	3.69 ^{+0.14} _{-0.13}	3.66 ^{+0.17} _{-0.17}	0.812 ^{+0.005} _{-0.004}
12 117 689	6918 ± 57	4.22 ± 0.10	-0.25 ± 0.04	184 ± 7	3.04 ± 0.27	6890 ⁺⁵⁹ ₋₅₈	4.02 ^{+0.19} _{-0.23}	3.08 ^{+0.22} _{-0.24}	0.749 ^{+0.006} _{-0.006}
12 458 189	6914 ± 44	3.73 ± 0.17	-0.09 ± 0.05	68 ± 3	3.08 ± 0.22	6865 ⁺⁵⁹ ₋₆₂	3.93 ^{+0.18} _{-0.19}	2.92 ^{+0.18} _{-0.20}	0.936 ^{+0.005} _{-0.005}
12 643 786	7154 ± 49	3.85 ± 0.20	-0.33 ± 0.06	72 ± 4	2.99 ± 0.29	7134 ⁺⁶³ ₋₆₅	3.77 ^{+0.25} _{-0.23}	2.98 ^{+0.33} _{-0.23}	0.768 ^{+0.007} _{-0.007}
γ Dor- δ Sct hybrids									
2 168 333	8059 ± 23	4.04 ± 0.06	-0.11 ± 0.02	170 ± 5	1.96 ± 0.12	8026 ⁺³⁶ ₋₃₅	4.00 ^{+0.15} _{-0.15}	2.28 ^{+0.16} _{-0.16}	1.47 ^{+0.01} _{-0.01}
3 241 199	7278 ± 52	3.73 ± 0.22	-0.18 ± 0.04	183 ± 8	3.42 ± 0.26	7269 ⁺⁵⁴ ₋₅₁	3.65 ^{+0.20} _{-0.23}	3.54 ^{+0.24} _{-0.26}	1.383 ^{+0.007} _{-0.007}
5 294 571	6934 ± 89	4.34 ± 0.21	-0.12 ± 0.09	131 ± 12	2.90 ± 0.61	6902 ⁺⁷⁸ ₋₈₁	4.31 ^{+0.26} _{-0.29}	2.72 ^{+0.29} _{-0.36}	0.643 ^{+0.004} _{-0.004}
5 608 334	6928 ± 39	4.63 ± 0.08	-0.24 ± 0.04	120 ± 4	2.38 ± 0.19	6885 ⁺⁵⁹ ₋₅₉	4.49 ^{+0.15} _{-0.18}	2.04 ^{+0.17} _{-0.20}	0.856 ^{+0.007} _{-0.007}

Table C.1. continued.

KIC	$T_{\text{eff,NN}}$ (K)	$\log g_{\text{NN}}$ (dex)	$[\text{M/H}]_{\text{NN}}$ (dex)	$v \sin i_{\text{NN}}$ (km s ⁻¹)	ξ_{NN} (km s ⁻¹)	$T_{\text{eff,GSSP}}$ (K)	$\log g_{\text{GSSP}}$ (dex)	ξ_{GSSP} (km s ⁻¹)	$\log(L/L_{\odot})$
7 106 648	7234 ± 31	4.03 ± 0.10	-0.19 ± 0.03	127 ± 3	3.84 ± 0.15	7272 ⁺⁴⁴ ₋₄₀	4.18 ^{+0.15} _{-0.15}	4.06 ^{+0.20} _{-0.18}	0.902 ^{+0.006} _{-0.007}
7 748 238	7288 ± 35	3.87 ± 0.10	-0.19 ± 0.02	128 ± 3	3.69 ± 0.15	7300 ⁺³⁸ ₋₃₈	3.83 ^{+0.13} _{-0.13}	3.80 ^{+0.15} _{-0.15}	0.778 ^{+0.002} _{-0.002}
7 770 282	7797 ± 19	3.97 ± 0.06	-0.09 ± 0.03	49 ± 1	3.02 ± 0.15	7820 ⁺⁴⁴ ₋₄₄	3.90 ^{+0.16} _{-0.16}	3.10 ^{+0.16} _{-0.17}	1.22 ^{+0.04} _{-0.04}
7 977 996	7218 ± 63	4.26 ± 0.18	-0.28 ± 0.07	118 ± 6	3.73 ± 0.33	7200 ⁺⁶⁷ ₋₇₃	4.05 ^{+0.28} _{-0.30}	3.93 ^{+0.38} _{-0.40}	0.99 ^{+0.01} _{-0.01}
8 645 874	7176 ± 25	3.78 ± 0.07	-0.18 ± 0.02	21 ± 1	3.63 ± 0.13	7143 ⁺⁶⁰ ₋₆₁	3.30 ^{+0.19} _{-0.15}	3.74 ^{+0.25} _{-0.21}	0.772 ^{+0.01} _{-0.009}
8 836 473	7115 ± 127	3.67 ± 0.65	-0.08 ± 0.12	117 ± 11	3.71 ± 0.73	7132 ⁺¹²¹ ₋₁₂₉	3.95 ^{+0.51} _{-0.53}	3.62 ^{+0.74} _{-0.67}	0.949^{+0.008}_{-0.008}
9 651 065	7257 ± 72	4.01 ± 0.21	-0.29 ± 0.07	130 ± 9	3.70 ± 0.41	7276 ⁺⁷⁶ ₋₇₃	4.03 ^{+0.30} _{-0.31}	4.02 ^{+0.36} _{-0.50}	0.99 ^{+0.01} _{-0.01}
9 751 996	7058 ± 57	3.38 ± 0.09	+0.12 ± 0.04	12 ± 1	3.45 ± 0.13	7139 ⁺⁶⁸ ₋₇₁	3.66 ^{+0.19} _{-0.20}	3.38 ^{+0.09} _{-0.09}	1.052 ^{+0.005} _{-0.006}
11 754 232	7108 ± 27	3.18 ± 0.06	-0.37 ± 0.03	11 ± 2	3.05 ± 0.13	7190 ⁺⁴⁶ ₋₄₆	3.60 ^{+0.14} _{-0.15}	2.93 ^{+0.16} _{-0.15}	0.89 ^{+0.03} _{-0.03}
12 365 420	7436 ± 54	3.86 ± 0.17	-0.24 ± 0.06	48 ± 3	2.95 ± 0.29	7414 ⁺⁷¹ ₋₇₁	3.79 ^{+0.27} _{-0.27}	3.07 ^{+0.32} _{-0.30}	1.41 ^{+0.01} _{-0.01}

Table C.2. Surface abundances of the γ Dor stars with respect to solar values ($[X/H] = \log_{10} \left(\frac{n_X}{n_{\text{tot}}} \right) - \log_{10} \left(\frac{n_X}{n_{\text{tot}}} \right)_{\odot}$).

KIC	C	O	Na	Mg	Al	Si	S	Ca	Sc	Ti	V
$NN - \text{man}$	+0.05 ± 0.09		-0.05 ± 0.12	-0.05 ± 0.10			-0.44 ± 0.06	-0.22 ± 0.09	-0.31 ± 0.17	-0.16 ± 0.16	
2 575 161	+0.08 ^{+0.11} _{-0.13}	+0.43 ^{+0.17} _{-0.23}	-0.11 ^{+0.11} _{-0.12}	+0.09 ^{+0.11} _{-0.11}	<-0.13	<-0.12	<-0.07	+0.03 ^{+0.15} _{-0.16}	-0.18 ^{+0.15} _{-0.15}	-0.18 ^{+0.10} _{-0.12}	-0.17 ^{+0.25} _{-0.43}
2 710 594	-0.20 ^{+0.15} _{-0.17}	<+0.07	-0.43 ^{+0.17} _{-0.21}	+0.09 ^{+0.11} _{-0.11}	<+0.27	<+0.19	<-0.14	-0.23 ^{+0.18} _{-0.19}	-0.32 ^{+0.16} _{-0.17}	-0.25 ^{+0.13} _{-0.13}	-0.42 ^{+0.33} _{-0.97}
2 846 358	-0.06 ^{+0.19} _{-0.25}	<+0.46	-0.26 ^{+0.16} _{-0.17}	+0.19 ^{+0.10} _{-0.10}	<+0.44	<+0.18	<+0.14	-0.19 ^{+0.20} _{-0.22}	-0.06 ^{+0.23} _{-0.25}	-0.16 ^{+0.17} _{-0.15}	-0.16 ^{+0.39} _{-0.78}
3 331 147	-0.04 ^{+0.12} _{-0.13}	+0.36 ^{+0.16} _{-0.23}	-0.08 ^{+0.13} _{-0.15}	+0.19 ^{+0.10} _{-0.10}	<-0.18	<+0.12	+0.01 ^{+0.23} _{-0.36}	-0.04 ^{+0.15} _{-0.16}	+0.01 ^{+0.14} _{-0.14}	-0.20 ^{+0.13} _{-0.10}	-0.07 ^{+0.22} _{-0.35}
3 448 365	+0.24 ^{+0.09} _{-0.09}	+0.37 ^{+0.21} _{-0.34}	+0.05 ^{+0.11} _{-0.12}	+0.18 ^{+0.10} _{-0.10}	<-0.03	<+0.21	+0.08 ^{+0.20} _{-0.32}	-0.01 ^{+0.14} _{-0.13}	+0.24 ^{+0.13} _{-0.10}	+0.06 ^{+0.10} _{-0.10}	-0.03 ^{+0.21} _{-0.31}
3 626 325	+0.04 ^{+0.14} _{-0.16}	+0.44 ^{+0.18} _{-0.25}	+0.03 ^{+0.14} _{-0.15}	+0.20 ^{+0.10} _{-0.10}	<-0.05	<+0.20	-0.06 ^{+0.27} _{-0.71}	+0.05 ^{+0.16} _{-0.17}	+0.08 ^{+0.16} _{-0.17}	-0.10 ^{+0.14} _{-0.15}	-0.09 ^{+0.28} _{-0.49}
3 648 936	-0.39 ^{+0.14} _{-0.17}	+0.24 ^{+0.19} _{-0.27}	-0.06 ^{+0.12} _{-0.13}	+0.06 ^{+0.12} _{-0.13}	<-0.37	<+0.04	-0.11 ^{+0.22} _{-0.35}	-0.19 ^{+0.15} _{-0.15}	-0.20 ^{+0.12} _{-0.13}	-0.37 ^{+0.10} _{-0.11}	-0.28 ^{+0.20} _{-0.29}
3 744 571	-0.20 ^{+0.19} _{-0.23}	+0.07 ^{+0.30} _{-0.82}	-0.35 ^{+0.19} _{-0.23}	+0.00 ^{+0.12} _{-0.13}	<+0.24	<+0.35	<-0.05	-0.25 ^{+0.24} _{-0.26}	-0.32 ^{+0.22} _{-0.23}	-0.34 ^{+0.18} _{-0.18}	<+0.04
3 942 392	+0.11 ^{+0.10} _{-0.12}	+0.41 ^{+0.19} _{-0.27}	-0.05 ^{+0.12} _{-0.13}	+0.11 ^{+0.10} _{-0.10}	<-0.21	<+0.14	-0.15 ^{+0.25} _{-0.50}	-0.06 ^{+0.13} _{-0.13}	+0.02 ^{+0.14} _{-0.14}	-0.15 ^{+0.10} _{-0.09}	-0.07 ^{+0.20} _{-0.27}
4 255 166	+0.04 ^{+0.13} _{-0.14}	+0.33 ^{+0.19} _{-0.28}	+0.06 ^{+0.12} _{-0.12}	+0.21 ^{+0.10} _{-0.10}	<+0.05	<+0.03	<+0.12	+0.06 ^{+0.16} _{-0.16}	+0.05 ^{+0.15} _{-0.16}	-0.05 ^{+0.12} _{-0.13}	-0.06 ^{+0.26} _{-0.41}
4 567 531	+0.16 ^{+0.16} _{-0.16}	+0.38 ^{+0.26} _{-0.56}	-0.09 ^{+0.15} _{-0.16}	+0.07 ^{+0.11} _{-0.11}	<+0.16	<-0.06	<+0.15	+0.05 ^{+0.16} _{-0.18}	+0.01 ^{+0.15} _{-0.19}	-0.05 ^{+0.15} _{-0.15}	-0.06 ^{+0.28} _{-0.46}
4 659 837	+0.13 ^{+0.12} _{-0.13}	+0.28 ^{+0.25} _{-0.48}	-0.06 ^{+0.11} _{-0.12}	+0.01 ^{+0.11} _{-0.11}	<+0.40	<+0.06	<+0.09	-0.19 ^{+0.17} _{-0.18}	-0.07 ^{+0.15} _{-0.16}	-0.17 ^{+0.13} _{-0.13}	-0.14 ^{+0.26} _{-0.40}
4 757 184	+0.12 ^{+0.09} _{-0.09}	+0.21 ^{+0.16} _{-0.22}	-0.42 ^{+0.14} _{-0.16}	-0.26 ^{+0.11} _{-0.12}	<+0.31	<+0.06	<-0.18	-0.60 ^{+0.18} _{-0.20}	-0.65 ^{+0.17} _{-0.18}	-0.72 ^{+0.17} _{-0.16}	<-0.28
4 846 809	-0.08 ^{+0.18} _{-0.23}	<+0.35	-0.19 ^{+0.20} _{-0.25}	+0.03 ^{+0.13} _{-0.13}	<+0.66	<+0.37	<-0.02	-0.16 ^{+0.25} _{-0.28}	+0.00 ^{+0.21} _{-0.22}	-0.12 ^{+0.17} _{-0.20}	<+0.22
5 018 590	+0.04 ^{+0.09} _{-0.10}	<+0.34	-0.14 ^{+0.12} _{-0.13}	+0.02 ^{+0.10} _{-0.10}	<-0.13	<-0.03	-0.31 ^{+0.27} _{-0.84}	-0.12 ^{+0.12} _{-0.13}	-0.04 ^{+0.12} _{-0.13}	-0.15 ^{+0.09} _{-0.09}	-0.22 ^{+0.22} _{-0.37}
5 113 797	-0.21 ^{+0.09} _{-0.10}	-0.17 ^{+0.11} _{-0.11}	<-0.46	+0.10 ^{+0.11} _{-0.11}	<-1.83	<+0.43	<-0.30	-0.38 ^{+0.14} _{-0.14}	-0.37 ^{+0.14} _{-0.12}	-0.45 ^{+0.12} _{-0.12}	<+0.03
5 114 382	-0.05 ^{+0.18} _{-0.22}	+0.27 ^{+0.26} _{-0.61}	-0.33 ^{+0.20} _{-0.26}	-0.08 ^{+0.11} _{-0.11}	<+0.07	<+0.34	+0.00 ^{+0.31} _{-1.42}	-0.19 ^{+0.24} _{-0.26}	-0.14 ^{+0.24} _{-0.26}	-0.22 ^{+0.18} _{-0.20}	-0.07 ^{+0.39} _{-1.27}
5 450 503	+0.10 ^{+0.13} _{-0.14}	+0.32 ^{+0.26} _{-0.57}	-0.12 ^{+0.13} _{-0.14}	-0.07 ^{+0.10} _{-0.10}	<+0.04	<-0.09	<+0.00	-0.13 ^{+0.15} _{-0.16}	-0.10 ^{+0.15} _{-0.16}	-0.16 ^{+0.10} _{-0.12}	-0.23 ^{+0.27} _{-0.48}
5 522 154	+0.17 ^{+0.11} _{-0.12}	<+0.35	-0.03 ^{+0.13} _{-0.15}	+0.05 ^{+0.10} _{-0.10}	<+0.00	<+0.35	+0.16 ^{+0.19} _{-0.27}	-0.29 ^{+0.19} _{-0.21}	-0.06 ^{+0.17} _{-0.18}	-0.26 ^{+0.16} _{-0.15}	<-0.11
5 646 058	+0.14 ^{+0.14} _{-0.15}	+0.32 ^{+0.25} _{-0.35}	+0.11 ^{+0.16} _{-0.17}	+0.28 ^{+0.11} _{-0.12}	<+0.14	<+0.14	-0.07 ^{+0.32} _{-1.52}	+0.05 ^{+0.20} _{-0.22}	-0.04 ^{+0.21} _{-0.22}	-0.14 ^{+0.16} _{-0.17}	-0.06 ^{+0.37} _{-1.62}
5 708 550	+0.00 ^{+0.15} _{-0.17}	+0.31 ^{+0.24} _{-0.45}	-0.14 ^{+0.16} _{-0.17}	+0.00 ^{+0.10} _{-0.10}	<+0.13	<+0.29	<+0.18	-0.12 ^{+0.19} _{-0.21}	-0.04 ^{+0.19} _{-0.21}	-0.11 ^{+0.13} _{-0.16}	-0.18 ^{+0.33} _{-0.76}
5 788 623	-0.08 ^{+0.13} _{-0.15}	+0.24 ^{+0.21} _{-0.34}	-0.22 ^{+0.13} _{-0.14}	+0.00 ^{+0.11} _{-0.11}	<+0.55	<+0.18	<+0.13	-0.17 ^{+0.17} _{-0.18}	-0.03 ^{+0.16} _{-0.16}	-0.16 ^{+0.13} _{-0.16}	-0.16 ^{+0.33} _{-0.85}
5 887 983	-0.04 ^{+0.15} _{-0.17}	+0.08 ^{+0.32} _{-1.32}	-0.12 ^{+0.16} _{-0.17}	+0.17 ^{+0.11} _{-0.11}	<+0.33	<-0.11	<-0.01	+0.02 ^{+0.17} _{-0.18}	-0.20 ^{+0.17} _{-0.19}	-0.17 ^{+0.14} _{-0.14}	-0.15 ^{+0.28} _{-0.52}
5 954 264	+0.21 ^{+0.09} _{-0.09}	+0.24 ^{+0.22} _{-0.34}	+0.12 ^{+0.12} _{-0.13}	+0.27 ^{+0.10} _{-0.10}	<-0.08	<+0.11	+0.11 ^{+0.15} _{-0.20}	-0.01 ^{+0.12} _{-0.13}	+0.10 ^{+0.11} _{-0.11}	-0.02 ^{+0.08} _{-0.08}	-0.07 ^{+0.18} _{-0.27}
6 064 932	-0.20 ^{+0.15} _{-0.17}	+0.42 ^{+0.16} _{-0.21}	-0.40 ^{+0.15} _{-0.17}	-0.03 ^{+0.11} _{-0.11}	<-0.04	<-0.03	<-0.18	-0.24 ^{+0.17} _{-0.18}	-0.36 ^{+0.16} _{-0.17}	-0.42 ^{+0.14} _{-0.13}	-0.37 ^{+0.31} _{-0.68}
6 131 093	+0.03 ^{+0.12} _{-0.14}	+0.42 ^{+0.19} _{-0.27}	-0.08 ^{+0.12} _{-0.13}	+0.01 ^{+0.10} _{-0.10}	<-0.03	<+0.11	-0.16 ^{+0.29} _{-0.14}	-0.01 ^{+0.15} _{-0.16}	+0.10 ^{+0.15} _{-0.16}	-0.06 ^{+0.11} _{-0.12}	-0.04 ^{+0.24} _{-0.35}
6 292 398	-0.90 ^{+0.19} _{-0.19}	-0.29 ^{+0.15} _{-0.12}	+0.22 ^{+0.11} _{-0.12}	+0.17 ^{+0.14} _{-0.14}	<+0.82	<+0.44	-0.07 ^{+0.23} _{-0.45}	-0.57 ^{+0.19} _{-0.22}	-1.95 ^{+0.30} _{-0.51}	-0.29 ^{+0.13} _{-0.14}	+0.17 ^{+0.22} _{-0.31}
6 301 745	+0.07 ^{+0.18} _{-0.23}	+0.45 ^{+0.31} _{-1.12}	+0.05 ^{+0.17} _{-0.19}	+0.06 ^{+0.11} _{-0.11}	<-0.25	<+0.02	+0.26 ^{+0.22} _{-0.37}	-0.14 ^{+0.19} _{-0.22}	+0.15 ^{+0.22} _{-0.24}	-0.19 ^{+0.16} _{-0.18}	-0.18 ^{+0.37} _{-2.18}
6 468 146	-0.14 ^{+0.08} _{-0.08}	+0.07 ^{+0.15} _{-0.25}	-0.34 ^{+0.09} _{-0.10}	+0.08 ^{+0.11} _{-0.11}	<-0.32	<-0.30	-0.33 ^{+0.21} _{-0.34}	-0.09 ^{+0.09} _{-0.09}	-0.19 ^{+0.10} _{-0.10}	-0.35 ^{+0.08} _{-0.08}	-0.31 ^{+0.17} _{-0.25}
6 468 987	+0.08 ^{+0.29} _{-0.41}	+0.52 ^{+0.28} _{-0.60}	-0.12 ^{+0.30} _{-0.39}	-0.08 ^{+0.16} _{-0.17}	<+0.67	<+1.00	<+0.38	-0.19 ^{+0.42} _{-0.52}	-0.19 ^{+0.47} _{-0.58}	-0.13 ^{+0.34} _{-0.36}	<+0.42
6 519 869	-0.16 ^{+0.09} _{-0.10}	+0.08 ^{+0.15} _{-0.21}	-0.23 ^{+0.10} _{-0.11}	+0.09 ^{+0.10} _{-0.10}	<+0.10	<+0.09	-0.25 ^{+0.25} _{-0.57}	-0.13 ^{+0.13} _{-0.13}	-0.22 ^{+0.11} _{-0.11}	-0.25 ^{+0.10} _{-0.10}	-0.33 ^{+0.24} _{-0.44}
6 678 174	-0.09 ^{+0.12} _{-0.14}	+0.02 ^{+0.25} _{-0.55}	-0.34 ^{+0.14} _{-0.16}	-0.06 ^{+0.11} _{-0.11}	<+0.18	<+0.29	<+0.01	-0.13 ^{+0.16} _{-0.16}	-0.12 ^{+0.14} _{-0.15}	-0.18 ^{+0.13} _{-0.14}	-0.20 ^{+0.29} _{-0.60}
6 935 014	+0.19 ^{+0.11} _{-0.12}	+0.06 ^{+0.20} _{-0.91}	-0.06 ^{+0.12} _{-0.13}	+0.12 ^{+0.10} _{-0.10}	<-0.04	<+0.27	-0.13 ^{+0.26} _{-0.61}	+0.00 ^{+0.16} _{-0.16}	-0.02 ^{+0.13} _{-0.14}	-0.05 ^{+0.10} _{-0.11}	-0.03 ^{+0.25} _{-0.39}
6 953 103	-0.14 ^{+0.20} _{-0.25}	<+0.40	-0.18 ^{+0.20} _{-0.26}	-0.03 ^{+0.13} _{-0.13}	<+0.66	<+0.42	<+0.16	-0.31 ^{+0.30} _{-0.33}	-0.23 ^{+0.26} _{-0.29}	-0.29 ^{+0.26} _{-0.25}	<+0.20

Notes. The second row in the header contains for the most important elements the mean difference between the NN abundances and the abundances from manual normalisation and its standard deviation for the 37 stars in the sample by [Van Reeth et al. \(2015\)](#) (see Sect. 4.1 for more information).

Table C.2. continued.

KIC	C	O	Na	Mg	Al	Si	S	Ca	Sc	Ti	V
7 023 122	$-0.11^{+0.09}_{-0.10}$	$+0.02^{+0.19}_{-0.30}$	$-0.28^{+0.12}_{-0.14}$	$+0.04^{+0.11}_{-0.11}$	<-0.21	$<+0.05$	<-0.12	$-0.22^{+0.14}_{-0.15}$	$-0.25^{+0.13}_{-0.13}$	$-0.39^{+0.11}_{-0.12}$	<-0.11
7 215 607	$-0.24^{+0.19}_{-0.24}$	$+0.70^{+0.18}_{-0.24}$	$-0.15^{+0.15}_{-0.16}$	$-0.21^{+0.12}_{-0.12}$	<-0.13	$<+0.00$	<-0.11	$-0.13^{+0.22}_{-0.25}$	$-0.10^{+0.24}_{-0.25}$	$-0.19^{+0.20}_{-0.20}$	$-0.19^{+0.37}_{-0.63}$
7 365 537	$+0.08^{+0.09}_{-0.09}$	$<+0.29$	$-0.18^{+0.13}_{-0.16}$	$+0.17^{+0.10}_{-0.10}$	$<+0.00$	$<+0.02$	$-0.29^{+0.27}_{-0.78}$	$-0.16^{+0.13}_{-0.13}$	$-0.12^{+0.12}_{-0.13}$	$-0.23^{+0.11}_{-0.10}$	-0.09
7 380 501	$-0.13^{+0.18}_{-0.22}$	$<+0.38$	$-0.14^{+0.15}_{-0.16}$	$+0.03^{+0.11}_{-0.11}$	$<+0.35$	$<+0.28$	$<+0.04$	$-0.14^{+0.21}_{-0.23}$	$-0.03^{+0.19}_{-0.20}$	$-0.14^{+0.14}_{-0.16}$	$-0.05^{+0.31}_{-0.54}$
7 434 470	$+0.24^{+0.21}_{-0.26}$	$<+0.53$	$-0.02^{+0.23}_{-0.28}$	$-0.04^{+0.12}_{-0.13}$	$<+0.77$	$<+0.46$	$<+0.35$	$-0.21^{+0.33}_{-0.40}$	$-0.02^{+0.37}_{-0.45}$	$-0.13^{+0.27}_{-0.29}$	$<+0.28$
7 583 663	$+0.28^{+0.25}_{-0.32}$	$+0.88^{+0.20}_{-0.27}$	$+0.35^{+0.28}_{-0.34}$	$+0.13^{+0.13}_{-0.14}$	$<+0.43$	$<+0.86$	$<+0.45$	$-0.16^{+0.42}_{-0.51}$	$+0.17^{+0.40}_{-0.47}$	$+0.01^{+0.32}_{-0.32}$	$<+0.47$
7 661 054	$-0.23^{+0.10}_{-0.12}$	$+0.06^{+0.16}_{-0.23}$	$+0.01^{+0.10}_{-0.10}$	$+0.13^{+0.11}_{-0.11}$	$<+0.33$	$<+0.01$	$-0.29^{+0.25}_{-0.53}$	$-0.10^{+0.13}_{-0.13}$	$-0.14^{+0.11}_{-0.11}$	$-0.33^{+0.10}_{-0.10}$	$-0.28^{+0.20}_{-0.30}$
7 694 191	$+0.07^{+0.10}_{-0.11}$	$+0.23^{+0.10}_{-0.11}$	$-0.07^{+0.16}_{-0.21}$	$+0.35^{+0.12}_{-0.12}$	$<+0.42$	$<+0.28$	$+0.02^{+0.25}_{-0.59}$	$-0.03^{+0.16}_{-0.17}$	$-0.09^{+0.14}_{-0.15}$	$-0.05^{+0.12}_{-0.12}$	$-0.03^{+0.33}_{-1.15}$
7 939 065	$-0.17^{+0.20}_{-0.25}$	$+0.36^{+0.20}_{-0.31}$	$-0.30^{+0.21}_{-0.28}$	$+0.04^{+0.13}_{-0.13}$	$<+0.26$	$<+0.27$	$<+0.11$	$-0.29^{+0.28}_{-0.31}$	$-0.22^{+0.25}_{-0.28}$	$-0.23^{+0.21}_{-0.21}$	$<+0.12$
8 123 127	$-0.01^{+0.13}_{-0.15}$	$+0.19^{+0.20}_{-0.30}$	$-0.13^{+0.15}_{-0.17}$	$+0.16^{+0.12}_{-0.13}$	<-0.01	$<+0.21$	$-0.11^{+0.27}_{-0.72}$	$-0.07^{+0.17}_{-0.18}$	$-0.04^{+0.16}_{-0.17}$	$-0.27^{+0.13}_{-0.14}$	$<+0.13$
8 197 761	$-0.22^{+0.10}_{-0.18}$	$-0.02^{+0.15}_{-0.20}$	$-0.21^{+0.09}_{-0.09}$	$+0.04^{+0.11}_{-0.11}$	$<+0.30$	<-0.10	$-0.38^{+0.25}_{-0.53}$	$-0.14^{+0.11}_{-0.12}$	$-0.24^{+0.11}_{-0.11}$	$-0.29^{+0.11}_{-0.12}$	$-0.34^{+0.19}_{-0.28}$
8 355 130	$+0.05^{+0.09}_{-0.09}$	$+0.29^{+0.14}_{-0.18}$	$-0.10^{+0.12}_{-0.14}$	$+0.10^{+0.11}_{-0.11}$	<-0.03	$<+0.18$	$-0.21^{+0.30}_{-1.50}$	$-0.09^{+0.14}_{-0.14}$	$-0.08^{+0.12}_{-0.12}$	$-0.16^{+0.11}_{-0.11}$	$-0.01^{+0.21}_{-0.31}$
8 364 249	$+0.01^{+0.15}_{-0.18}$	$<+0.23$	$-0.54^{+0.26}_{-0.36}$	$+0.12^{+0.11}_{-0.11}$	$<+0.81$	$<+0.14$	$<+0.01$	$-0.18^{+0.22}_{-0.24}$	$-0.17^{+0.21}_{-0.22}$	$-0.30^{+0.16}_{-0.16}$	$-0.31^{+0.38}_{-2.96}$
8 375 138	$-0.06^{+0.12}_{-0.14}$	$<+0.21$	$-0.24^{+0.16}_{-0.17}$	$+0.01^{+0.10}_{-0.11}$	$<+0.17$	$<+0.09$	<-0.02	$-0.21^{+0.16}_{-0.17}$	$-0.15^{+0.16}_{-0.16}$	$-0.27^{+0.12}_{-0.12}$	$-0.40^{+0.35}_{-1.57}$
8 651 452	$+0.09^{+0.13}_{-0.14}$	$<+0.38$	$-0.09^{+0.15}_{-0.16}$	$+0.27^{+0.11}_{-0.11}$	$<+0.38$	<-0.19	$-0.21^{+0.29}_{-0.97}$	$+0.09^{+0.16}_{-0.17}$	$-0.20^{+0.17}_{-0.19}$	$-0.20^{+0.14}_{-0.14}$	$-0.27^{+0.33}_{-0.97}$
8 871 304	$-0.01^{+0.10}_{-0.11}$	$+0.10^{+0.29}_{-0.89}$	$-0.30^{+0.12}_{-0.13}$	$-0.01^{+0.10}_{-0.10}$	<-0.12	<-0.17	$-0.37^{+0.28}_{-0.83}$	$-0.20^{+0.13}_{-0.13}$	$-0.14^{+0.12}_{-0.12}$	$-0.17^{+0.09}_{-0.09}$	$-0.18^{+0.20}_{-0.29}$
9 210 943	$+0.11^{+0.15}_{-0.18}$	$+0.54^{+0.20}_{-0.29}$	$-0.20^{+0.16}_{-0.19}$	$+0.02^{+0.10}_{-0.10}$	$<+0.04$	$<+0.42$	$<+0.15$	$-0.06^{+0.19}_{-0.21}$	$+0.05^{+0.20}_{-0.17}$	$-0.12^{+0.16}_{-0.17}$	$-0.14^{+0.36}_{-0.36}$
9 419 182	$+0.15^{+0.10}_{-0.10}$	$+0.34^{+0.25}_{-0.45}$	$+0.10^{+0.14}_{-0.15}$	$+0.19^{+0.10}_{-0.10}$	<-0.21	$<+0.04$	$+0.19^{+0.17}_{-0.24}$	$+0.05^{+0.13}_{-0.14}$	$+0.17^{+0.13}_{-0.14}$	$-0.06^{+0.10}_{-0.10}$	$-0.06^{+0.18}_{-0.25}$
9 480 469	$+0.21^{+0.25}_{-0.31}$	$<+0.65$	$+0.29^{+0.24}_{-0.28}$	$+0.30^{+0.13}_{-0.14}$	$<+1.05$	$<+0.81$	$<+0.43$	$-0.04^{+0.42}_{-0.50}$	$-0.02^{+0.43}_{-0.51}$	$+0.01^{+0.28}_{-0.31}$	$<+0.57$
9 490 067	$-0.14^{+0.32}_{-0.54}$	$<+0.69$	$+0.03^{+0.25}_{-0.30}$	$+0.08^{+0.13}_{-0.13}$	$<+0.28$	$<+0.55$	$+0.16^{+0.33}_{-1.40}$	$-0.11^{+0.34}_{-0.40}$	$+0.02^{+0.34}_{-0.41}$	$-0.06^{+0.24}_{-0.28}$	$<+0.36$
9 595 743	$+0.02^{+0.14}_{-0.16}$	$+0.33^{+0.18}_{-0.28}$	$-0.23^{+0.16}_{-0.17}$	$-0.04^{+0.11}_{-0.11}$	$<+0.61$	$<+0.29$	$<+0.14$	$-0.15^{+0.19}_{-0.20}$	$-0.11^{+0.18}_{-0.19}$	$-0.20^{+0.13}_{-0.14}$	$<+0.14$
9 716 358	$-0.09^{+0.10}_{-0.11}$	$+0.19^{+0.10}_{-0.12}$	$-0.09^{+0.11}_{-0.12}$	$+0.14^{+0.13}_{-0.13}$	$+0.71^{+0.25}_{-0.54}$	$<+0.30$	$-0.20^{+0.26}_{-0.75}$	$-0.15^{+0.14}_{-0.15}$	$-0.13^{+0.13}_{-0.14}$	$-0.20^{+0.11}_{-0.13}$	$+0.11^{+0.22}_{-0.33}$
9 962 653	$-0.02^{+0.10}_{-0.11}$	$<+0.34$	$-0.08^{+0.12}_{-0.13}$	$+0.12^{+0.10}_{-0.10}$	<-0.26	<-0.35	$-0.26^{+0.24}_{-0.46}$	$-0.09^{+0.11}_{-0.11}$	$-0.09^{+0.13}_{-0.13}$	$-0.21^{+0.11}_{-0.11}$	$-0.24^{+0.40}_{-0.40}$
10 224 094	$-0.14^{+0.12}_{-0.14}$	$+0.12^{+0.22}_{-0.37}$	$-0.18^{+0.13}_{-0.14}$	$+0.05^{+0.11}_{-0.12}$	$<+0.13$	$<+0.15$	<-0.05	$-0.14^{+0.16}_{-0.16}$	$-0.18^{+0.14}_{-0.15}$	$-0.24^{+0.12}_{-0.13}$	$-0.23^{+0.28}_{-0.53}$
10 256 787	$-0.04^{+0.16}_{-0.18}$	$+0.25^{+0.25}_{-0.50}$	$-0.19^{+0.15}_{-0.16}$	$+0.03^{+0.10}_{-0.11}$	$<+0.35$	$<+0.25$	$<+0.10$	$-0.11^{+0.18}_{-0.20}$	$+0.04^{+0.18}_{-0.19}$	$-0.08^{+0.14}_{-0.15}$	$-0.01^{+0.30}_{-0.53}$
10 317 467	$-0.17^{+0.10}_{-0.11}$	$+0.31^{+0.12}_{-0.15}$	$-0.22^{+0.09}_{-0.10}$	$+0.07^{+0.13}_{-0.13}$	$<+0.07$	$<+0.03$	<-0.12	$-0.19^{+0.13}_{-0.14}$	$-0.22^{+0.12}_{-0.12}$	$-0.27^{+0.11}_{-0.12}$	$-0.14^{+0.22}_{-0.36}$
10 467 146	$-0.20^{+0.21}_{-0.25}$	$+0.04^{+0.29}_{-0.76}$	$-0.15^{+0.23}_{-0.28}$	$-0.13^{+0.16}_{-0.17}$	$<+0.64$	$<+0.42$	<-0.12	$-0.44^{+0.31}_{-0.36}$	$-0.54^{+0.28}_{-0.31}$	$-0.56^{+0.26}_{-0.26}$	$<+0.03$
10 470 294	$+0.03^{+0.20}_{-0.28}$	$<+0.42$	$+0.07^{+0.16}_{-0.18}$	$+0.13^{+0.10}_{-0.11}$	<-0.10	<-0.09	$<+0.24$	$-0.07^{+0.20}_{-0.26}$	$+0.04^{+0.23}_{-0.23}$	$-0.11^{+0.17}_{-0.18}$	$<+0.22$
11 080 103	$-0.32^{+0.28}_{-0.44}$	$+0.29^{+0.29}_{-0.68}$	$-0.32^{+0.26}_{-0.38}$	$-0.19^{+0.16}_{-0.17}$	$<+0.64$	$<+0.47$	$<+0.15$	$-0.29^{+0.34}_{-0.39}$	$-0.44^{+0.31}_{-0.35}$	$-0.39^{+0.27}_{-0.29}$	$<+1.00$
11 099 031	$+0.31^{+0.13}_{-0.15}$	$<+0.40$	$+0.11^{+0.15}_{-0.16}$	$+0.26^{+0.10}_{-0.11}$	$<+0.62$	$<+0.23$	$+0.19^{+0.19}_{-0.29}$	$+0.23^{+0.14}_{-0.15}$	$+0.42^{+0.15}_{-0.15}$	$+0.28^{+0.11}_{-0.13}$	$+0.21^{+0.18}_{-0.23}$
11 294 808	$-0.17^{+0.18}_{-0.21}$	$+0.05^{+0.30}_{-1.03}$	$-0.31^{+0.18}_{-0.22}$	$+0.10^{+0.11}_{-0.11}$	$<+0.72$	$<+0.33$	$+0.01$	$-0.09^{+0.21}_{-0.23}$	$-0.20^{+0.19}_{-0.20}$	$-0.22^{+0.16}_{-0.17}$	$-0.21^{+0.34}_{-0.77}$
11 456 474	$-0.13^{+0.25}_{-0.36}$	$+0.39^{+0.27}_{-0.59}$	$+0.02^{+0.23}_{-0.28}$	$-0.04^{+0.13}_{-0.15}$	$<+0.96$	$<+0.67$	$+0.40$	$-0.18^{+0.34}_{-0.38}$	$-0.10^{+0.31}_{-0.35}$	$-0.21^{+0.25}_{-0.34}$	$<+0.27$
11 607 017	$+0.17^{+0.19}_{-0.23}$	$<+0.57$	$+0.23^{+0.20}_{-0.23}$	$+0.26^{+0.13}_{-0.13}$	$<+0.17$	$<+0.30$	$+0.18^{+0.27}_{-0.68}$	$-0.02^{+0.27}_{-0.31}$	$+0.10^{+0.28}_{-0.32}$	$-0.18^{+0.20}_{-0.24}$	$<+0.36$
11 612 274	$-0.06^{+0.12}_{-0.12}$	$+0.22^{+0.23}_{-0.41}$	$-0.27^{+0.15}_{-0.16}$	$+0.02^{+0.11}_{-0.11}$	<-0.11	<-0.33	$-0.26^{+0.31}_{-1.40}$	$-0.23^{+0.16}_{-0.16}$	$-0.36^{+0.15}_{-0.16}$	$-0.35^{+0.12}_{-0.13}$	$-0.32^{+0.31}_{-0.87}$
11 721 304	$-0.15^{+0.13}_{-0.15}$	$+0.30^{+0.18}_{-0.25}$	$-0.17^{+0.13}_{-0.14}$	$+0.15^{+0.10}_{-0.11}$	$<+0.09$	$<+0.23$	$<+0.07$	$-0.05^{+0.16}_{-0.17}$	$-0.01^{+0.14}_{-0.15}$	$-0.10^{+0.13}_{-0.13}$	$-0.12^{+0.28}_{-0.50}$
11 826 272	$+0.06^{+0.10}_{-0.11}$	$+0.27^{+0.16}_{-0.23}$	$+0.10^{+0.10}_{-0.11}$	$+0.33^{+0.10}_{-0.10}$	<-0.15	$<+0.19$	$+0.07^{+0.17}_{-0.24}$	$+0.07^{+0.14}_{-0.14}$	$+0.06^{+0.12}_{-0.12}$	$-0.02^{+0.10}_{-0.10}$	$-0.02^{+0.17}_{-0.23}$
11 907 454	$-0.07^{+0.16}_{-0.19}$	$<+0.39$	$-0.21^{+0.16}_{-0.18}$	$+0.12^{+0.10}_{-0.10}$	$<+0.43$	$<+0.19$	$<+0.09$	$-0.10^{+0.19}_{-0.21}$	$-0.04^{+0.19}_{-0.21}$	$-0.12^{+0.14}_{-0.16}$	$-0.25^{+0.38}_{-2.07}$
11 917 550	$+0.09^{+0.12}_{-0.13}$	$+0.33^{+0.20}_{-0.30}$	$-0.11^{+0.13}_{-0.14}$	$+0.14^{+0.10}_{-0.11}$	$<+0.04$	$<+0.22$	$-0.12^{+0.28}_{-0.79}$	$-0.08^{+0.16}_{-0.17}$	$+0.00^{+0.15}_{-0.15}$	$-0.11^{+0.15}_{-0.13}$	$-0.10^{+0.27}_{-0.49}$
11 920 505	$-0.01^{+0.09}_{-0.10}$	$+0.30^{+0.15}_{-0.21}$	$-0.01^{+0.10}_{-0.11}$	$+0.23^{+0.10}_{-0.10}$	$<+0.04$	$<+0.12$	$+0.01^{+0.18}_{-0.26}$	$+0.05^{+0.11}_{-0.12}$	$-0.01^{+0.11}_{-0.11}$	$-0.14^{+0.10}_{-0.11}$	$-0.14^{+0.26}_{-0.18}$
12 066 947	$-0.06^{+0.09}_{-0.10}$	$<+0.23$	$-0.30^{+0.14}_{-0.16}$	$+0.14^{+0.11}_{-0.11}$	<-0.06	$<+0.00$	$-0.30^{+0.27}_{-0.82}$	$-0.26^{+0.14}_{-0.14}$	$-0.30^{+0.14}_{-0.14}$	$-0.31^{+0.13}_{-0.13}$	<-0.21
12 117 689	$+0.15^{+0.15}_{-0.18}$	$<+0.50$	$-0.21^{+0.17}_{-0.20}$	$+0.11^{+0.10}_{-0.10}$	$<+0.42$	<-0.22	$+0.05^{+0.25}_{-0.49}$	$-0.09^{+0.18}_{-0.20}$	$-0.18^{+0.22}_{-0.24}$	$-0.21^{+0.15}_{-0.17}$	$<+0.07$
12 458 189	$+0.02^{+0.15}_{-0.17}$	$<+0.42$	$-0.25^{+0.16}_{-0.18}$	$+0.18^{+0.10}_{-0.10}$	$<+0.37$	$<+0.32$	$<+0.10$	$+0.08^{+0.18}_{-0.19}$	$+0.09^{+0.15}_{-0.16}$	$-0.01^{+0.13}_{-0.15}$	$-0.01^{+0.27}_{-0.42}$
12 643 786	$-0.06^{+0.13}_{-0.15}$	$+0.28^{+0.20}_{-0.31}$	$-0.46^{+0.17}_{-0.25}$	$+0.00^{+0.11}_{-0.11}$	$<+0.11$	$<+0.34$	<-0.04	$-0.25^{+0.19}_{-0.20}$	$-0.21^{+0.17}_{-0.18}$	$-0.33^{+0.17}_{-0.17}$	$<+0.04$
γ Dor- δ Sct hybrids											
2 168 333	$+0.05^{+0.09}_{-0.09}$	$+0.10^{+0.09}_{-0.12}$	$-0.28^{+0.16}_{-0.19}$	$+0.34^{+0.10}_{-0.10}$	$<+0.65$	$<+0.27$	$-0.11^{+0.23}_{-0.45}$	$-0.21^{+0.14}_{-0.15}$	$-0.16^{+0.14}_{-0.15}$	$-0.20^{+0.13}_{-0.13}$	$<+0.16$
3 241 199	$+0.07^{+0.12}_{-0.13}$	$<+0.30$	$-0.08^{+0.18}_{-0.22}$	$+0.25^{+0.12}_{-0.12}$	$<+0.35$	$<+0.24$	$<+0.11$	$+0.01^{+0.18}_{-0.19}$	$+0.00^{+0.18}_{-0.19}$	$-0.10^{+0.15}_{-0.15}$	$<+0.18$
5 294 571	$+0.02^{+0.24}_{-0.32}$	$<+0.52$	$-0.06^{+0.22}_{-0.27}$	$-0.01^{+0.11}_{-0.11}$	$<+0.43$	$<+0.44$	$<+0.24</$				

Table C.3. Surface abundances of the γ Dor stars with respect to solar values ($[X/H] = \log_{10} \left(\frac{n_x}{n_{\text{tot}}} \right) - \log_{10} \left(\frac{n_x}{n_{\text{tot}}} \right)_{\odot}$).

KIC	Cr	Mn	Fe	Co	Ni	Cu	Zn	Sr	Y	Zr	Ba
$NN - man$	-0.28 ± 0.14	-0.73 ± 0.39	-0.28 ± 0.16		-0.13 ± 0.15				-0.40 ± 0.20		-0.80 ± 0.33
2 575 161	$-0.22^{+0.14}_{-0.15}$	$-0.21^{+0.14}_{-0.16}$	$-0.27^{+0.07}_{-0.07}$	$+0.06^{+0.26}_{-0.44}$	$-0.20^{+0.12}_{-0.14}$	<-0.10	<-0.54	$-0.26^{+0.29}_{-0.42}$	$-0.45^{+0.22}_{-0.26}$	$-0.30^{+0.35}_{-0.85}$	$+0.13^{+0.17}_{-0.18}$
2 710 594	$-0.28^{+0.16}_{-0.17}$	$-0.49^{+0.18}_{-0.21}$	$-0.30^{+0.09}_{-0.09}$	<-0.07	$-0.35^{+0.17}_{-0.18}$	<-0.14	$-0.77^{+0.44}_{-1.33}$	$-0.36^{+0.42}_{-0.61}$	$-0.45^{+0.22}_{-0.25}$	$-0.33^{+0.34}_{-0.70}$	$+0.08^{+0.18}_{-0.19}$
2 846 358	$-0.23^{+0.18}_{-0.20}$	$-0.38^{+0.24}_{-0.28}$	$-0.27^{+0.10}_{-0.11}$	$-0.19^{+0.41}_{-1.86}$	$-0.32^{+0.18}_{-0.21}$	<-0.06	$-0.62^{+0.55}_{-0.91}$	$+0.09^{+0.25}_{-0.33}$	$-0.20^{+0.36}_{-0.44}$	$<+0.44$	$+0.44^{+0.15}_{-0.17}$
3 331 147	$-0.17^{+0.15}_{-0.15}$	$-0.31^{+0.14}_{-0.16}$	$-0.25^{+0.09}_{-0.09}$	$<+0.05$	$-0.29^{+0.16}_{-0.17}$	<-0.01	$-0.58^{+0.36}_{-0.63}$	$+0.23^{+0.19}_{-0.25}$	$-0.14^{+0.19}_{-0.21}$	$-0.04^{+0.27}_{-0.44}$	$+0.22^{+0.15}_{-0.16}$
3 448 365	$-0.10^{+0.14}_{-0.13}$	$-0.21^{+0.11}_{-0.12}$	$-0.03^{+0.06}_{-0.07}$	<-0.15	$+0.01^{+0.10}_{-0.11}$	$<-0.05^{+0.23}_{-0.34}$	$-0.57^{+0.32}_{-0.52}$	$+0.17^{+0.25}_{-0.33}$	$+0.09^{+0.15}_{-0.16}$	$+0.10^{+0.22}_{-0.33}$	$+0.30^{+0.14}_{-0.15}$
3 626 325	$-0.09^{+0.16}_{-0.19}$	$-0.21^{+0.16}_{-0.19}$	$-0.19^{+0.08}_{-0.08}$	$+0.07^{+0.30}_{-0.58}$	$-0.21^{+0.16}_{-0.17}$	$<+0.00$	$-0.54^{+0.43}_{-0.74}$	$+0.23^{+0.24}_{-0.33}$	$-0.16^{+0.23}_{-0.26}$	$-0.07^{+0.35}_{-0.72}$	$+0.25^{+0.17}_{-0.19}$
3 648 936	$-0.44^{+0.14}_{-0.16}$	$-0.57^{+0.14}_{-0.17}$	$-0.52^{+0.07}_{-0.07}$	<-0.01	$-0.43^{+0.13}_{-0.15}$	<-0.15	$-0.55^{+0.29}_{-0.38}$	$+0.01^{+0.21}_{-0.27}$	$-0.15^{+0.16}_{-0.16}$	$-0.21^{+0.21}_{-0.28}$	$+0.02^{+0.15}_{-0.16}$
3 744 571	$-0.44^{+0.22}_{-0.24}$	$-0.50^{+0.24}_{-0.32}$	$-0.49^{+0.11}_{-0.10}$	$<+0.05$	$-0.55^{+0.23}_{-0.28}$	$<+0.03$	<-0.22	$-0.22^{+0.51}_{-0.89}$	$-0.40^{+0.30}_{-0.35}$	$<+0.09$	$-0.14^{+0.22}_{-0.24}$
3 942 392	$-0.15^{+0.13}_{-0.14}$	$-0.25^{+0.11}_{-0.13}$	$-0.17^{+0.06}_{-0.06}$	$-0.14^{+0.29}_{-0.62}$	$-0.23^{+0.12}_{-0.13}$	<-0.21	$-0.63^{+0.33}_{-0.50}$	$+0.08^{+0.18}_{-0.23}$	$-0.18^{+0.17}_{-0.18}$	$-0.01^{+0.25}_{-0.38}$	$+0.32^{+0.14}_{-0.15}$
4 255 166	$-0.05^{+0.15}_{-0.16}$	$-0.15^{+0.15}_{-0.16}$	$-0.11^{+0.07}_{-0.08}$	$-0.06^{+0.31}_{-0.70}$	$-0.15^{+0.14}_{-0.15}$	<-0.05	$-0.57^{+0.43}_{-0.75}$	$+0.09^{+0.26}_{-0.40}$	$-0.24^{+0.22}_{-0.25}$	$-0.06^{+0.30}_{-0.52}$	$+0.42^{+0.16}_{-0.17}$
4 567 531	$-0.17^{+0.18}_{-0.18}$	$-0.19^{+0.17}_{-0.19}$	$-0.19^{+0.08}_{-0.09}$	$+0.25^{+0.23}_{-0.32}$	$-0.15^{+0.16}_{-0.16}$	<-0.07	<-0.45	$-0.36^{+0.41}_{-0.67}$	$-0.19^{+0.27}_{-0.31}$	$-0.11^{+0.36}_{-0.80}$	$+0.38^{+0.14}_{-0.16}$
4 659 837	$-0.18^{+0.15}_{-0.16}$	$-0.24^{+0.14}_{-0.16}$	$-0.28^{+0.09}_{-0.08}$	$-0.04^{+0.26}_{-0.42}$	$-0.26^{+0.13}_{-0.14}$	$-0.50^{+0.36}_{-1.47}$	$-0.59^{+0.33}_{-0.44}$	$+0.16^{+0.29}_{-0.47}$	$-0.32^{+0.20}_{-0.23}$	$+0.02^{+0.28}_{-0.44}$	$+0.12^{+0.23}_{-0.25}$
4 757 184	$-0.73^{+0.21}_{-0.22}$	$-0.78^{+0.22}_{-0.28}$	$-0.73^{+0.09}_{-0.09}$	<-0.18	$-0.77^{+0.19}_{-0.25}$	<-0.29	<-0.54	$-0.28^{+0.35}_{-0.49}$	$-0.84^{+0.25}_{-0.32}$	<-0.11	$-0.53^{+0.17}_{-0.18}$
4 846 809	$-0.31^{+0.22}_{-0.27}$	$-0.35^{+0.26}_{-0.35}$	$-0.30^{+0.11}_{-0.11}$	$<+0.12$	$-0.27^{+0.21}_{-0.26}$	$<+0.23$	$<+0.11$	$-0.77^{+0.86}_{-1.00}$	$-0.16^{+0.32}_{-0.38}$	$<+0.44$	$+0.23^{+0.25}_{-0.25}$
5 018 590	$-0.22^{+0.13}_{-0.13}$	$-0.30^{+0.11}_{-0.13}$	$-0.23^{+0.06}_{-0.07}$	$+0.17^{+0.19}_{-0.24}$	$-0.28^{+0.10}_{-0.11}$	<-0.17	$-0.72^{+0.32}_{-0.54}$	$+0.07^{+0.16}_{-0.20}$	$-0.10^{+0.16}_{-0.15}$	$-0.14^{+0.27}_{-0.48}$	$+0.39^{+0.13}_{-0.14}$
5 113 797	$-0.50^{+0.16}_{-0.16}$	$-0.27^{+0.17}_{-0.24}$	$-0.44^{+0.08}_{-0.08}$	$<+0.37$	$-0.36^{+0.17}_{-0.22}$	$<+0.27$	<-0.06	$-0.23^{+0.25}_{-0.25}$	$-0.30^{+0.19}_{-0.24}$	$-0.11^{+0.34}_{-1.50}$	$-0.05^{+0.13}_{-0.13}$
5 114 382	$-0.27^{+0.20}_{-0.20}$	$-0.37^{+0.25}_{-0.33}$	$-0.33^{+0.10}_{-0.10}$	$<+0.23$	$-0.34^{+0.21}_{-0.27}$	$<+0.08$	<-0.12	$+0.03^{+0.39}_{-0.48}$	$-0.34^{+0.36}_{-0.48}$	$<+0.45$	$+0.40^{+0.21}_{-0.23}$
5 450 503	$-0.24^{+0.14}_{-0.16}$	$-0.36^{+0.14}_{-0.17}$	$-0.26^{+0.07}_{-0.07}$	$+0.10^{+0.22}_{-0.32}$	$-0.26^{+0.13}_{-0.15}$	<-0.23	<-0.45	$-0.15^{+0.26}_{-0.37}$	$-0.24^{+0.22}_{-0.24}$	$-0.24^{+0.38}_{-1.25}$	$+0.17^{+0.14}_{-0.16}$
5 522 154	$-0.39^{+0.20}_{-0.22}$	$-0.52^{+0.21}_{-0.28}$	$-0.21^{+0.08}_{-0.08}$	<-0.24	$-0.30^{+0.16}_{-0.19}$	<-0.12	$-0.50^{+0.41}_{-0.73}$	$-0.98^{+0.56}_{-0.63}$	$-0.11^{+0.22}_{-0.25}$	$<+0.10$	$+0.04^{+0.18}_{-0.19}$
5 646 058	$-0.14^{+0.19}_{-0.21}$	$-0.21^{+0.20}_{-0.26}$	$-0.22^{+0.09}_{-0.09}$	$<+0.33$	$-0.23^{+0.19}_{-0.23}$	<-0.03	<-0.24	$-0.40^{+0.67}_{-0.89}$	$-0.13^{+0.30}_{-0.35}$	$<+0.37$	$-0.11^{+0.21}_{-0.21}$
5 708 550	$-0.15^{+0.16}_{-0.19}$	$-0.34^{+0.19}_{-0.22}$	$-0.21^{+0.08}_{-0.09}$	$<+0.00$	$-0.20^{+0.16}_{-0.19}$	$<+0.05$	$-0.58^{+0.44}_{-0.80}$	$+0.07^{+0.28}_{-0.45}$	$-0.25^{+0.27}_{-0.32}$	$+0.05^{+0.35}_{-0.65}$	$+0.33^{+0.17}_{-0.19}$
5 788 623	$-0.24^{+0.16}_{-0.18}$	$-0.36^{+0.18}_{-0.22}$	$-0.30^{+0.09}_{-0.09}$	$<+0.07$	$-0.32^{+0.16}_{-0.18}$	$<+0.02$	$-0.60^{+0.38}_{-0.82}$	$-0.18^{+0.46}_{-0.68}$	$-0.26^{+0.23}_{-0.27}$	$-0.05^{+0.37}_{-1.02}$	$+0.23^{+0.17}_{-0.18}$
5 887 983	$-0.30^{+0.18}_{-0.21}$	$-0.31^{+0.17}_{-0.21}$	$-0.30^{+0.08}_{-0.08}$	$+0.09^{+0.28}_{-0.50}$	$-0.32^{+0.17}_{-0.19}$	<-0.15	<-0.39	$-0.72^{+0.59}_{-0.77}$	$-0.22^{+0.24}_{-0.27}$	$-0.29^{+0.37}_{-0.77}$	$+0.14^{+0.18}_{-0.19}$
5 954 264	$-0.02^{+0.12}_{-0.12}$	$-0.16^{+0.10}_{-0.11}$	$-0.11^{+0.06}_{-0.06}$	$-0.16^{+0.31}_{-0.99}$	$-0.06^{+0.11}_{-0.12}$	$-0.31^{+0.30}_{-0.82}$	$-0.38^{+0.24}_{-0.31}$	$-0.19^{+0.26}_{-0.32}$	$-0.15^{+0.13}_{-0.14}$	$-0.07^{+0.22}_{-0.33}$	$-0.14^{+0.16}_{-0.17}$
6 064 932	$-0.46^{+0.16}_{-0.19}$	$-0.61^{+0.20}_{-0.24}$	$-0.51^{+0.09}_{-0.09}$	$<+0.00$	$-0.54^{+0.17}_{-0.20}$	<-0.25	<-0.40	$-0.06^{+0.29}_{-0.42}$	$-0.48^{+0.22}_{-0.25}$	$-0.29^{+0.33}_{-0.70}$	$+0.04^{+0.17}_{-0.17}$
6 131 093	$-0.05^{+0.14}_{-0.15}$	$-0.26^{+0.15}_{-0.16}$	$-0.16^{+0.09}_{-0.09}$	$-0.18^{+0.35}_{-0.88}$	$-0.17^{+0.12}_{-0.14}$	<-0.12	$-0.56^{+0.40}_{-0.55}$	$+0.06^{+0.18}_{-0.25}$	$-0.14^{+0.22}_{-0.24}$	$-0.06^{+0.34}_{-0.62}$	$+0.42^{+0.14}_{-0.16}$
6 292 398	$+0.10^{+0.15}_{-0.16}$	$+0.04^{+0.15}_{-0.19}$	$+0.07^{+0.09}_{-0.08}$	$+0.26^{+0.33}_{-1.47}$	$+0.36^{+0.13}_{-0.20}$	$+0.19^{+0.31}_{-0.86}$	$+0.77^{+0.17}_{-0.18}$	$+1.04^{+0.25}_{-0.36}$	$+0.71^{+0.15}_{-0.15}$	$+0.74^{+0.14}_{-0.15}$	$+1.85^{+0.13}_{-0.14}$
6 301 745	$-0.17^{+0.19}_{-0.21}$	$-0.32^{+0.20}_{-0.24}$	$-0.32^{+0.09}_{-0.10}$	$-0.13^{+0.33}_{-0.80}$	$-0.36^{+0.20}_{-0.26}$	$<+0.21$	$<+0.03$	$-0.71^{+0.65}_{-0.93}$	$+0.06^{+0.32}_{-0.38}$	$<+0.33$	$-0.12^{+0.21}_{-0.22}$
6 468 146	$-0.39^{+0.12}_{-0.12}$	$-0.45^{+0.11}_{-0.11}$	$-0.43^{+0.06}_{-0.06}$	$-0.20^{+0.23}_{-0.41}$	$-0.35^{+0.09}_{-0.10}$	<-0.37	$-0.77^{+0.26}_{-0.46}$	$-0.51^{+0.31}_{-0.34}$	$-0.34^{+0.10}_{-0.11}$	$-0.12^{+0.15}_{-0.18}$	$-0.27^{+0.11}_{-0.11}$
6 468 987	$-0.40^{+0.37}_{-0.50}$	$-0.28^{+0.39}_{-0.60}$	$-0.32^{+0.18}_{-0.18}$	$<+0.33$	$-0.20^{+0.34}_{-0.44}$	$<+0.17$	$<+0.69$	$-1.19^{+1.55}_{-2.21}$	$+0.02^{+0.61}_{-0.87}$	$<+0.39$	$+0.12^{+0.45}_{-0.51}$
6 519 869	$-0.27^{+0.13}_{-0.14}$	$-0.40^{+0.12}_{-0.14}$	$-0.34^{+0.07}_{-0.07}$	<-0.03	$-0.39^{+0.11}_{-0.12}$	<-0.26	$-0.63^{+0.28}_{-0.41}$	$+0.12^{+0.19}_{-0.23}$	$-0.38^{+0.12}_{-0.12}$	$-0.09^{+0.21}_{-0.29}$	$+0.21^{+0.15}_{-0.16}$
6 678 174	$-0.38^{+0.17}_{-0.18}$	$-0.41^{+0.16}_{-0.20}$	$-0.39^{+0.09}_{-0.09}$	<-0.17	$-0.39^{+0.15}_{-0.16}$	<-0.02	$-0.58^{+0.35}_{-0.61}$	$-0.09^{+0.33}_{-0.44}$	$-0.25^{+0.19}_{-0.21}$	$-0.05^{+0.30}_{-0.53}$	$+0.00^{+0.17}_{-0.17}$
6 935 014	$-0.06^{+0.13}_{-0.14}$	$-0.26^{+0.14}_{-0.16}$	$-0.14^{+0.07}_{-0.07}$	$<+0.02$	$-0.13^{+0.11}_{-0.12}$	<-0.11	$-0.69^{+0.39}_{-0.76}$	$+0.01^{+0.25}_{-0.33}$	$-0.19^{+0.18}_{-0.19}$	$-0.07^{+0.31}_{-0.57}$	$+0.16^{+0.15}_{-0.16}$
6 953 103	$-0.44^{+0.27}_{-0.32}$	$-0.41^{+0.29}_{-0.41}$	$-0.45^{+0.14}_{-0.14}$	$<+0.10$	$-0.41^{+0.26}_{-0.34}$	$<+0.02$	$<+0.12$	$-0.13^{+0.57}_{-1.12}$	$-0.32^{+0.39}_{-0.51}$	$<+0.26$	$+0.19^{+0.28}_{-0.31}$
7 023 122	$-0.40^{+0.15}_{-0.16}$	$-0.48^{+0.15}_{-0.18}$	$-0.38^{+0.08}_{-0.08}$	$<+0.08$	$-0.41^{+0.13}_{-0.15}$	<-0.09	$-0.76^{+0.32}_{-0.78}$	$-0.07^{+0.25}_{-0.30}$	$-0.43^{+0.16}_{-0.17}$	$-0.19^{+0.27}_{-0.49}$	$+0.10^{+0.13}_{-0.13}$
7 215 607	$-0.24^{+0.20}_{-0.22}$	$-0.29^{+0.26}_{-0.29}$	$-0.31^{+0.09}_{-0.09}$	$-0.25^{+0.43}_{-1.21}$	$-0.28^{+0.20}_{-0.24}$	<-0.17	$-0.77^{+0.67}_{-1.37}$	$-0.23^{+0.25}_{-0.33}$	$-0.39^{+0.17}_{-0.57}$	$<+0.22$	$+0.22^{+0.16}_{-0.18}$
7 365 537	$-0.24^{+0.13}_{-0.15}$	$-0.38^{+0.15}_{-0.18}$	$-0.18^{+0.06}_{-0.07}$	$+0.12^{+0.28}_{-0.60}$	$-0.35^{+0.13}_{-0.14}$	<-0.16	$-0.72^{+0.35}_{-1.07}$	$-0.26^{+0.25}_{-0.29}$	$-0.24^{+0.15}_{-0.16}$	$<+0.09$	$+0.12^{+0.14}_{-0.15}$
7 380 501	$-0.21^{+0.18}_{-0.19}$	$-0.27^{+0.20}_{-0.24}$	$-0.26^{+0.10}_{-0.11}$	$<+0.31$	$-0.28^{+0.17}_{-0.19}$	$<+0.03$	$-0.58^{+0.46}_{-0.92}$	$-0.03^{+0.37}_{-0.64}$	$-0.33^{+0.29}_{-0.35}$	$-0.06^{+0.39}_{-0.86}$	$+0.32^{+0.19}_{-0.22}$
7 434 470	$-0.29^{+0.28}_{-0.35}$	$-0.38^{+0.33}_{-0.47}$	$-0.23^{+0.15}_{-0.14}$	$<+0.31$	$-0.10^{+0.27}_{-0.33}$	$<+0.23$	$<+0.57$	$-1.70^{+1.56}_{-1.71}$	$+0.00^{+0.52}_{-0.71}$	$<+0.30$	$+0.26^{+0.28}_{-0.33}$
7 583 663	$-0.26^{+0.35}_{-0.42}$	$-0.30^{+0.41}_{-0.69}$	$-0.18^{+0.18}_{-0.18}$	$<+0.48$	$+0.07^{+0.31}_{-0.55}$	$<+0.74$	$<+0.76$	$-0.65^{+1.17}_{-0.76}$	$+0.10^{+0.58}_{-0.76}$	$<+0.75$	$+0.06^{+0.42}_{-0.49}$
7 661 054	$-0.27^{+0.13}_{-0.13}$	$-0.27^{+0.10}_{-0.11}$	$-0.24^{+0.07}_{-0.08}$	$-0.24^{+0.30}_{-0.68}$	$-0.14^{+0.10}_{-0.11}$	$-0.35^{+0.28}_{-0.62}$	$-0.30^{+0.23}_{-0.26}$	$+0.23^{+0.21}_{-0.28}$	$-0.25^{+0.12}_{-0.12}$	$-0.01^{+0.16}_{-0.19}$	$+0.21^{+0.17}_{-0.17}$
7 694 191	$-0.15^{+0.18}_{-0.18}$	$-0.05^{+0.18}_{-0.22}$	$-0.21^{+0.08}_{-0.09}$	$+0.42^{+0.33}_{-1.28}$	$-0.18^{+0.14}_{-0.18}$	$<+0.51$	<-0.12	$-0.28^{+0.50}_{-0.54}$	$-0.18^{+0.22}_{-0.28}$	$+0.09^{+0.30}_{-0.65}$	$-0.20^{+0.14}_{-0.14}$
7 939 065	$-0.37^{+0.24}_{-0.27}$	$-0.39^{+0.26}_{-0.35}$	$-0.37^{+0.12}_{-0.11}$	$<+0.02$	$-0.32^{+0.23}_{-0.28}$	$<+0.18$	$<+0.20$	$+0.03^{+0.46}_{-0.84}$	$-0.23^{+0.35}_{-0.44}$	$<+0.25$	$+0.09^{+0.25}_{-0.27}$
8 123 127	$-0.27^{+0.17}_{-0.18}$	$-0.29^{+0.17}_{-0.22}$	$-0.34^{+0.09}_{-0.09}$	$<+0.27$	$-0.26^{+0.16}_{-0.18}$	$<+0.11$	$-0.54^{+0.44}_{-1.57}$	$-0.17^{+0.47}_{-0.6$			

Table C.3. continued.

KIC	Cr	Mn	Fe	Co	Ni	Cu	Zn	Sr	Y	Zr	Ba
9 716 358	-0.25 ^{+0.16} _{-0.16}	-0.19 ^{+0.14} _{-0.17}	-0.31 ^{+0.08} _{-0.09}	+0.11 ^{+0.31} _{-1.03}	-0.28 ^{+0.16} _{-0.16}	<+0.23	-0.14 ^{+0.24} _{-0.32}	+0.46 ^{+0.26} _{-0.34}	+0.03 ^{+0.14} _{-0.16}	+0.18 ^{+0.22} _{-0.32}	+0.89 ^{+0.16} _{-0.16}
9 962 653	-0.28 ^{+0.13} _{-0.13}	-0.37 ^{+0.11} _{-0.12}	-0.27 ^{+0.06} _{-0.06}	+0.42 ^{+0.16} _{-0.20}	-0.33 ^{+0.12} _{-0.13}	<-0.26	-0.81 ^{+0.36} _{-0.87}	-0.34 ^{+0.29} _{-0.37}	-0.05 ^{+0.14} _{-0.16}	-0.16 ^{+0.25} _{-0.41}	+0.29 ^{+0.14} _{-0.15}
10 224 094	-0.28 ^{+0.15} _{-0.16}	-0.41 ^{+0.16} _{-0.19}	-0.34 ^{+0.08} _{-0.09}	<+0.06	-0.39 ^{+0.13} _{-0.16}	<-0.23	-0.67 ^{+0.33} _{-0.54}	+0.09 ^{+0.29} _{-0.41}	-0.35 ^{+0.19} _{-0.22}	-0.04 ^{+0.28} _{-0.45}	+0.29 ^{+0.17} _{-0.17}
10 256 787	-0.13 ^{+0.16} _{-0.17}	-0.27 ^{+0.18} _{-0.21}	-0.21 ^{+0.08} _{-0.09}	<+0.21	-0.29 ^{+0.16} _{-0.17}	<+0.07	-0.60 ^{+0.44} _{-0.86}	+0.20 ^{+0.27} _{-0.41}	-0.16 ^{+0.26} _{-0.29}	-0.03 ^{+0.39} _{-1.07}	+0.36 ^{+0.17} _{-0.18}
10 317 467	-0.32 ^{+0.15} _{-0.16}	-0.36 ^{+0.13} _{-0.15}	-0.40 ^{+0.07} _{-0.07}	<+0.12	-0.40 ^{+0.13} _{-0.14}	<-0.10	-0.77 ^{+0.30} _{-0.61}	+0.04 ^{+0.26} _{-0.32}	-0.42 ^{+0.16} _{-0.17}	-0.22 ^{+0.26} _{-0.47}	-0.19 ^{+0.17} _{-0.17}
10 467 146	-0.67 ^{+0.29} _{-0.37}	-0.59 ^{+0.31} _{-0.49}	-0.69 ^{+0.15} _{-0.15}	<-0.06	-0.63 ^{+0.30} _{-0.44}	<-0.23	<-0.06	+0.51 ^{+0.30} _{-0.48}	+0.34 ^{+0.33} _{-0.35}	+0.30 ^{+0.34} _{-0.44}	+0.47 ^{+0.21} _{-0.25}
10 470 294	-0.22 ^{+0.20} _{-0.21}	-0.28 ^{+0.21} _{-0.25}	-0.23 ^{+0.09} _{-0.10}	+0.49 ^{+0.23} _{-0.32}	-0.26 ^{+0.20} _{-0.22}	<+0.05	<-0.40	-0.48 ^{+0.55} _{-0.99}	+0.06 ^{+0.35} _{-0.41}	<+0.24	+0.37 ^{+0.18} _{-0.21}
11 080 103	-0.56 ^{+0.31} _{-0.41}	-0.52 ^{+0.37} _{-0.71}	-0.59 ^{+0.15} _{-0.16}	<+0.26	-0.60 ^{+0.35} _{-0.55}	<-0.02	<-0.19	-0.36 ^{+0.84} _{-1.55}	-0.53 ^{+0.47} _{-0.73}	<+0.39	-0.17 ^{+0.36} _{-0.38}
11 099 031	+0.19 ^{+0.12} _{-0.13}	+0.00 ^{+0.13} _{-0.14}	+0.14 ^{+0.06} _{-0.06}	+0.34 ^{+0.21} _{-0.27}	+0.20 ^{+0.10} _{-0.11}	-0.21 ^{+0.31} _{-0.58}	-0.68 ^{+0.47} _{-1.00}	-0.03 ^{+0.25} _{-0.38}	+0.10 ^{+0.20} _{-0.21}	+0.16 ^{+0.28} _{-0.38}	+0.57 ^{+0.14} _{-0.16}
11 294 808	-0.33 ^{+0.19} _{-0.21}	-0.45 ^{+0.21} _{-0.27}	-0.31 ^{+0.09} _{-0.09}	<+0.06	-0.36 ^{+0.23} _{-0.23}	<+0.07	<-0.30	-0.17 ^{+0.45} _{-0.75}	-0.39 ^{+0.28} _{-0.33}	-0.27 ^{+0.43} _{-1.64}	+0.00 ^{+0.23} _{-0.25}
11 456 474	-0.31 ^{+0.30} _{-0.35}	-0.36 ^{+0.31} _{-0.44}	-0.38 ^{+0.15} _{-0.16}	<+0.30	-0.33 ^{+0.29} _{-0.38}	<+0.05	<+0.44	+0.30 ^{+0.42} _{-0.61}	-0.22 ^{+0.46} _{-0.61}	<+0.45	+0.23 ^{+0.29} _{-0.35}
11 607 017	-0.12 ^{+0.22} _{-0.25}	-0.19 ^{+0.25} _{-0.34}	-0.29 ^{+0.12} _{-0.13}	+0.38 ^{+0.37} _{-0.92}	-0.18 ^{+0.28} _{-0.28}	<+0.38	<+0.39	-0.97 ^{+1.08} _{-1.18}	-0.11 ^{+0.42} _{-0.57}	<+0.43	-0.24 ^{+0.29} _{-0.30}
11 612 274	-0.50 ^{+0.17} _{-0.17}	-0.55 ^{+0.18} _{-0.22}	-0.49 ^{+0.08} _{-0.08}	+0.06 ^{+0.25} _{-0.45}	-0.50 ^{+0.16} _{-0.18}	<-0.41	<-0.51	-0.66 ^{+0.41} _{-0.46}	-0.36 ^{+0.21} _{-0.24}	<-0.01	-0.32 ^{+0.16} _{-0.16}
11 721 304	-0.15 ^{+0.16} _{-0.16}	-0.30 ^{+0.16} _{-0.18}	-0.19 ^{+0.07} _{-0.07}	<+0.11	-0.25 ^{+0.14} _{-0.15}	<+0.01	-0.62 ^{+0.37} _{-0.68}	+0.19 ^{+0.26} _{-0.38}	-0.20 ^{+0.20} _{-0.23}	-0.03 ^{+0.31} _{-0.55}	+0.47 ^{+0.17} _{-0.18}
11 826 272	+0.02 ^{+0.13} _{-0.13}	-0.12 ^{+0.10} _{-0.11}	-0.11 ^{+0.06} _{-0.06}	-0.19 ^{+0.31} _{-0.77}	-0.09 ^{+0.11} _{-0.12}	-0.23 ^{+0.27} _{-0.52}	-0.37 ^{+0.29} _{-0.36}	+0.22 ^{+0.19} _{-0.24}	-0.22 ^{+0.15} _{-0.16}	-0.03 ^{+0.20} _{-0.26}	+0.20 ^{+0.16} _{-0.17}
11 907 454	-0.19 ^{+0.16} _{-0.22}	-0.29 ^{+0.19} _{-0.22}	-0.17 ^{+0.09} _{-0.09}	<+0.19	-0.23 ^{+0.16} _{-0.18}	<+0.12	<-0.24	-0.65 ^{+0.59} _{-0.86}	-0.16 ^{+0.27} _{-0.30}	<+0.27	+0.46 ^{+0.17} _{-0.18}
11 917 550	-0.20 ^{+0.16} _{-0.16}	-0.27 ^{+0.15} _{-0.17}	-0.18 ^{+0.08} _{-0.07}	<-0.22	-0.11 ^{+0.16} _{-0.16}	-0.05 ^{+0.29} _{-0.54}	-0.72 ^{+0.41} _{-1.52}	-0.32 ^{+0.39} _{-0.54}	-0.16 ^{+0.20} _{-0.23}	-0.07 ^{+0.33} _{-0.64}	+0.13 ^{+0.18} _{-0.19}
11 920 505	-0.14 ^{+0.13} _{-0.14}	-0.26 ^{+0.10} _{-0.12}	-0.18 ^{+0.06} _{-0.06}	-0.30 ^{+0.32} _{-1.13}	-0.19 ^{+0.10} _{-0.11}	<-0.40	-0.58 ^{+0.29} _{-0.42}	+0.10 ^{+0.19} _{-0.23}	-0.18 ^{+0.14} _{-0.14}	-0.07 ^{+0.20} _{-0.26}	+0.29 ^{+0.14} _{-0.15}
12 066 947	-0.36 ^{+0.14} _{-0.16}	-0.48 ^{+0.15} _{-0.18}	-0.33 ^{+0.07} _{-0.06}	<-0.01	-0.39 ^{+0.13} _{-0.15}	<-0.12	-0.75 ^{+0.37} _{-1.33}	-0.53 ^{+0.34} _{-0.38}	-0.39 ^{+0.17} _{-0.19}	-0.35 ^{+0.34} _{-1.13}	-0.20 ^{+0.14} _{-0.14}
12 117 689	-0.34 ^{+0.18} _{-0.20}	-0.29 ^{+0.18} _{-0.21}	-0.30 ^{+0.08} _{-0.09}	+0.23 ^{+0.26} _{-0.42}	-0.27 ^{+0.17} _{-0.21}	<-0.09	<-0.38	-0.79 ^{+0.63} _{-0.87}	-0.27 ^{+0.30} _{-0.37}	<+0.17	+0.31 ^{+0.17} _{-0.19}
12 458 189	-0.01 ^{+0.15} _{-0.16}	-0.25 ^{+0.17} _{-0.20}	-0.10 ^{+0.09} _{-0.09}	<+0.10	-0.13 ^{+0.14} _{-0.16}	<-0.01	<-0.30	+0.15 ^{+0.26} _{-0.39}	-0.13 ^{+0.23} _{-0.25}	+0.03 ^{+0.33} _{-0.54}	+0.30 ^{+0.18} _{-0.20}
12 643 786	-0.42 ^{+0.19} _{-0.21}	-0.52 ^{+0.21} _{-0.27}	-0.42 ^{+0.09} _{-0.09}	<-0.27	-0.51 ^{+0.24} _{-0.25}	<-0.07	-0.63 ^{+0.43} _{-1.17}	+0.06 ^{+0.31} _{-0.47}	-0.29 ^{+0.24} _{-0.27}	-0.06 ^{+0.34} _{-0.68}	-0.02 ^{+0.19} _{-0.20}
γ Dor- δ Sct hybrids											
2 168 333	-0.19 ^{+0.15} _{-0.16}	-0.18 ^{+0.14} _{-0.19}	-0.24 ^{+0.08} _{-0.07}	<+0.21	-0.26 ^{+0.16} _{-0.18}	<+0.20	<+0.01	-0.40 ^{+0.38} _{-0.41}	-0.32 ^{+0.24} _{-0.33}	<+0.16	-0.04 ^{+0.15} _{-0.16}
3 241 199	-0.15 ^{+0.16} _{-0.19}	-0.25 ^{+0.17} _{-0.24}	-0.20 ^{+0.08} _{-0.09}	<+0.29	-0.20 ^{+0.16} _{-0.18}	<-0.10	<-0.09	-0.77 ^{+0.69} _{-0.77}	-0.01 ^{+0.26} _{-0.29}	<+0.16	-0.05 ^{+0.21} _{-0.21}
5 294 571	-0.22 ^{+0.24} _{-0.28}	-0.30 ^{+0.30} _{-0.32}	-0.21 ^{+0.11} _{-0.12}	+0.41 ^{+0.32} _{-0.53}	-0.20 ^{+0.25} _{-0.28}	<+0.33	<+0.17	+0.11 ^{+0.43} _{-1.02}	+0.06 ^{+0.45} _{-0.54}	<+0.41	+0.61 ^{+0.21} _{-0.26}
5 608 334	-0.36 ^{+0.19} _{-0.18}	-0.47 ^{+0.18} _{-0.21}	-0.29 ^{+0.08} _{-0.08}	+0.52 ^{+0.20} _{-0.20}	-0.39 ^{+0.19} _{-0.20}	<-0.21	<-0.56	-0.12 ^{+0.25} _{-0.37}	-0.01 ^{+0.27} _{-0.30}	<+0.20	+0.58 ^{+0.13} _{-0.15}
7 106 648	-0.17 ^{+0.15} _{-0.16}	-0.36 ^{+0.13} _{-0.17}	-0.20 ^{+0.06} _{-0.06}	+0.49 ^{+0.19} _{-0.23}	-0.28 ^{+0.14} _{-0.16}	<-0.10	<-0.34	-0.27 ^{+0.30} _{-0.34}	-0.08 ^{+0.16} _{-0.18}	-0.18 ^{+0.35} _{-1.59}	-0.18 ^{+0.18} _{-0.19}
7 748 238	-0.21 ^{+0.13} _{-0.13}	-0.30 ^{+0.11} _{-0.14}	-0.21 ^{+0.06} _{-0.06}	+0.09 ^{+0.34} _{-0.22}	-0.23 ^{+0.10} _{-0.11}	<-0.11	-0.56 ^{+0.29} _{-0.50}	-0.65 ^{+0.33} _{-0.35}	-0.14 ^{+0.13} _{-0.14}	-0.14 ^{+0.24} _{-0.41}	+0.21 ^{+0.16} _{-0.17}
7 770 282	-0.15 ^{+0.14} _{-0.14}	-0.19 ^{+0.12} _{-0.14}	-0.19 ^{+0.06} _{-0.06}	<+0.31	-0.14 ^{+0.12} _{-0.13}	<+0.12	-0.37 ^{+0.23} _{-0.38}	+0.32 ^{+0.19} _{-0.22}	+0.06 ^{+0.11} _{-0.12}	+0.26 ^{+0.17} _{-0.23}	+0.32 ^{+0.13} _{-0.14}
7 977 996	-0.37 ^{+0.22} _{-0.28}	-0.43 ^{+0.24} _{-0.37}	-0.37 ^{+0.10} _{-0.10}	+0.30 ^{+0.31} _{-0.63}	-0.31 ^{+0.21} _{-0.26}	<+0.18	<-0.04	-1.52 ^{+0.81} _{-0.66}	-0.21 ^{+0.32} _{-0.42}	<+0.25	-0.17 ^{+0.24} _{-0.24}
8 645 874	-0.26 ^{+0.14} _{-0.14}	-0.34 ^{+0.10} _{-0.11}	-0.25 ^{+0.08} _{-0.08}	<+0.02	-0.10 ^{+0.11} _{-0.12}	-0.33 ^{+0.27} _{-0.61}	-0.19 ^{+0.17} _{-0.19}	+0.37 ^{+0.19} _{-0.23}	-0.01 ^{+0.10} _{-0.11}	+0.06 ^{+0.15} _{-0.17}	+0.78 ^{+0.11} _{-0.11}
8 836 473	-0.26 ^{+0.34} _{-0.46}	-0.23 ^{+0.41} _{-0.74}	-0.16 ^{+0.18} _{-0.18}	<+0.40	+0.02 ^{+0.32} _{-0.40}	<+0.51	<+0.81	-0.20 ^{+1.05} _{-2.11}	+0.07 ^{+0.60} _{-0.80}	<+0.43	-0.12 ^{+0.45} _{-0.47}
9 651 065	-0.38 ^{+0.24} _{-0.29}	-0.45 ^{+0.28} _{-0.48}	-0.33 ^{+0.09} _{-0.11}	<+0.62	-0.26 ^{+0.20} _{-0.27}	<+0.11	<-0.02	-1.03 ^{+0.87} _{-0.85}	-0.23 ^{+0.35} _{-0.48}	<+0.21	-0.16 ^{+0.25} _{-0.25}
9 751 996	+0.23 ^{+0.13} _{-0.13}	+0.09 ^{+0.11} _{-0.13}	+0.09 ^{+0.07} _{-0.07}	+0.35 ^{+0.23} _{-0.29}	+0.29 ^{+0.10} _{-0.10}	+0.19 ^{+0.22} _{-0.28}	+0.29 ^{+0.27} _{-0.27}	+0.54 ^{+0.25} _{-0.36}	+0.05 ^{+0.15} _{-0.16}	-0.25 ^{+0.33} _{-0.77}	+1.23 ^{+0.14} _{-0.15}
11 754 232	-0.33 ^{+0.13} _{-0.14}	-0.39 ^{+0.13} _{-0.14}	-0.36 ^{+0.09} _{-0.09}	<+0.02	-0.39 ^{+0.11} _{-0.13}	<-0.22	-0.51 ^{+0.24} _{-0.33}	-0.03 ^{+0.30} _{-0.41}	-0.46 ^{+0.14} _{-0.16}	-0.19 ^{+0.22} _{-0.24}	+0.20 ^{+0.17} _{-0.17}
12 365 420	-0.39 ^{+0.21} _{-0.24}	-0.36 ^{+0.27} _{-0.35}	-0.41 ^{+0.10} _{-0.09}	<+0.39	-0.32 ^{+0.21} _{-0.26}	<+0.12	<-0.13	-0.27 ^{+0.65} _{-0.89}	-0.27 ^{+0.30} _{-0.38}	<+0.38	-0.03 ^{+0.23} _{-0.24}

Appendix D: Stellar parameters and surface abundances of the SPB stars

The stellar parameters of the SPB stars are listed in Table D.1 while the surface abundances can be found in Table D.2.

Table D.1. Stellar parameters of the SPB stars.

KIC	$T_{\text{eff,NN}}$ (K)	$\log g_{\text{NN}}$ (dex)	[M/H] _{NN} (dex)	$v \sin i_{\text{NN}}$ (km s ⁻¹)	ξ_{NN} (km s ⁻¹)	$T_{\text{eff,GSSP}}$ (K)	$\log g_{\text{GSSP}}$ (dex)	ξ_{GSSP} (km s ⁻¹)	$\log(L/L_{\odot})$
3 240 411	20 910 ⁺⁶⁴⁵ ₋₅₀₁	3.99 ^{+0.12} _{-0.13}	-0.18 ± 0.10	42 ± 4	3.6 ^{+2.1} _{-2.8}	20 910 ⁺⁶⁴⁵ ₋₅₀₁	3.99 ^{+0.12} _{-0.13}	3.6 ^{+2.1} _{-2.8}	3.43 ^{+0.06} _{-0.05}
3 756 031	15 947 ⁺⁵³² ₋₅₈₃	3.69 ^{+0.11} _{-0.12}	-0.44 ± 0.18	32 ± 4	<3.9	15 947 ⁺⁵³² ₋₅₈₃	3.69 ^{+0.11} _{-0.12}	<3.9	3.12 ^{+0.05} _{-0.05}
3 839 930	15 987 ⁺³¹⁹ ₋₃₃₃	4.00 ^{+0.08} _{-0.08}	-0.23 ± 0.15	33 ± 4	<3.2	15 987 ⁺³¹⁹ ₋₃₃₃	4.00 ^{+0.08} _{-0.08}	<3.2	2.71 ^{+0.04} _{-0.04}
3 865 742	20 108 ± 1820	3.86 ± 0.26	+0.07 ± 0.34	130 ± 27	4.2 ± 7.1	18 798 ⁺¹⁶⁸² ₋₁₅₈₄	3.58 ^{+0.28} _{-0.27}	2 (fixed)	3.68 ^{+0.14} _{-0.12}
5 941 844	14 025 ⁺²⁹³ ₋₃₀₅	4.24 ^{+0.08} _{-0.07}	-0.13 ^{+0.12} _{-0.14}	30 ± 3	<3.6	13 677 ⁺²³⁷ ₋₂₁₀	4.17 ^{+0.07} _{-0.08}	<1.6	2.34 ^{+0.03} _{-0.03}

Table D.1. continued.

KIC	$T_{\text{eff,NN}}$ (K)	$\log g_{\text{NN}}$ (dex)	$[M/H]_{\text{NN}}$ (dex)	$v \sin i_{\text{NN}}$ (km s ⁻¹)	ξ_{NN} (km s ⁻¹)	$T_{\text{eff,GSSP}}$ (K)	$\log g_{\text{GSSP}}$ (dex)	ξ_{GSSP} (km s ⁻¹)	$\log(L/L_{\odot})$
6 462 033	18 671 ± 907	4.15 ± 0.12	-0.32 ± 0.37	75 ± 21	2.2 ± 4.2	17 628 ⁺⁹⁵¹ ₋₁₀₂₁	3.93 ^{+0.19} _{-0.20}	<5.8	3.29 ^{+0.06} _{-0.06}
6 780 397	12 879 ± 190	3.74 ± 0.08	-0.45 ± 0.11	49 ± 5	5.0 ± 1.4	12 906 ⁺²⁸⁸ ₋₂₄₅	3.68 ^{+0.11} _{-0.11}	<2.4	2.69 ^{+0.04} _{-0.03}
7 760 680	11 602 ± 119	3.89 ± 0.05	-0.13 ± 0.06	58 ± 5	2.6 ± 0.6	11 791 ⁺²⁴⁶ ₋₂₄₉	3.92 ^{+0.10} _{-0.10}	2.0 ^{+0.5} _{-0.7}	2.31 ^{+0.03} _{-0.03}
8 057 661	22 087 ⁺¹⁰³⁹ ₋₁₁₀₅	3.97 ^{+0.18} _{-0.17}	-0.24 ± 0.27	35 ± 9	<8.2	22 087 ⁺¹⁰³⁹ ₋₁₁₀₅	3.97 ^{+0.18} _{-0.17}	<8.2	3.45 ^{+0.06} _{-0.07}
8 087 269	13 110 ± 765	3.78 ± 0.26	-0.09 ± 0.33	275 ± 54	4.5 ± 6.6	13 005 ⁺⁹¹³ ₋₆₄₆	3.69 ^{+0.23} _{-0.24}	<6.2	2.71 ^{+0.09} _{-0.07}
8 381 949	20 962 ± 820	3.88 ± 0.11	-0.17 ± 0.16	231 ± 20	5.5 ± 3.8	21 008 ⁺⁹⁴⁹ ₋₁₁₁₇	3.80 ^{+0.18} _{-0.17}	<7.2	3.66 ^{+0.07} _{-0.06}
8 459 899	16 478 ⁺¹⁶¹ ₋₁₉₄	3.78 ^{+0.05} _{-0.05}	-0.43 ^{+0.10} _{-0.08}	53 ± 4	5.0 ^{+1.6} _{-1.5}	15 512 ⁺²⁷³ ₋₂₆₁	3.60 ^{+0.05} _{-0.05}	3.7 ^{+1.0} _{-0.9}	3.10 ^{+0.07} _{-0.06}
8 714 886	17 703 ⁺⁶⁹⁴ ₋₆₈₃	3.95 ^{+0.13} _{-0.13}	-0.32 ± 0.17	28 ± 5	<4.9	17 703 ⁺⁶⁹⁴ ₋₆₈₃	3.95 ^{+0.13} _{-0.13}	<4.9	3.14 ^{+0.05} _{-0.04}
8 766 405	14 288 ± 157	3.49 ± 0.06	-0.38 ± 0.09	214 ± 10	6.4 ± 1.4	13 985 ⁺⁴²⁰ ₋₃₃₆	3.36 ^{+0.07} _{-0.07}	3.9 ^{+1.8} _{-1.5}	3.15 ^{+0.04} _{-0.04}
9 964 614	21 334 ± 449	4.03 ± 0.12	-0.34 ± 0.18	43 ± 13	2.6 ± 2.2	20 162 ⁺¹³⁴⁶ ₋₉₁₁	3.83 ^{+0.15} _{-0.17}	2 (fixed)	3.68 ^{+0.10} _{-0.08}
10 285 114	15 993 ± 328	4.10 ± 0.07	-0.21 ± 0.14	248 ± 18	3.0 ± 1.9	15 574 ⁺⁴⁵³ ₋₄₄₅	3.97 ^{+0.09} _{-0.09}	<5.1	2.67 ^{+0.06} _{-0.05}
10 536 147	21 097 ± 1302	3.78 ± 0.16	-0.12 ± 0.20	163 ± 18	4.5 ± 4.3	20 844 ⁺¹³⁷⁷ ₋₁₅₄₆	3.66 ^{+0.22} _{-0.22}	2 (fixed)	3.82 ^{+0.17} _{-0.14}
11 360 704	18 168 ± 682	3.94 ± 0.10	-0.16 ± 0.16	301 ± 20	6.4 ± 4.4	17 528 ⁺⁸²¹ ₋₈₆₆	3.81 ^{+0.16} _{-0.17}	<9.2	3.35 ^{+0.08} _{-0.07}
11 971 405	14 997 ± 146	3.96 ± 0.05	-0.18 ± 0.06	229 ± 9	4.9 ± 1.0	14 746 ⁺¹²⁸ ₋₁₂₉	3.81 ^{+0.06} _{-0.06}	3.9 ^{+1.3} _{-1.2}	2.83 ^{+0.02} _{-0.02}
12 258 330	16 167 ± 132	4.30 ± 0.04	-0.18 ± 0.10	99 ± 8	2.9 ± 1.3	15 513 ⁺⁵⁵¹ ₋₅₃₁	4.11 ^{+0.11} _{-0.11}	2 (fixed)	2.66 ^{+0.04} _{-0.04}

Table D.2. Surface abundances of the SPB stars with respect to solar values ($[X/H] = \log_{10} \left(\frac{n_X}{n_{\text{tot}}} \right) - \log_{10} \left(\frac{n_X}{n_{\text{tot}}} \right)_{\odot}$).

KIC	He	C	N	O	Ne	Mg	Si	S	Ca	Fe
3 240 411	+0.16 ^{+0.01} _{-0.01}	-0.17 ^{+0.10} _{-0.11}	-0.08 ^{+0.12} _{-0.13}	+0.00 ^{+0.13} _{-0.14}	<+1.37	+0.15 ^{+0.14} _{-0.15}	-0.45 ^{+0.14} _{-0.15}	-0.46 ^{+0.12} _{-0.13}	<+0.99	-0.29 ^{+0.24} _{-0.36}
3 756 031	+0.19 ^{+0.01} _{-0.01}	+0.10 ^{+0.12} _{-0.14}	-0.11 ^{+0.30} _{-0.50}	-0.05 ^{+0.33} _{-0.53}	<+1.42	+0.01 ^{+0.16} _{-0.17}	-0.59 ^{+0.16} _{-0.17}	-0.45 ^{+0.14} _{-0.15}	<+0.51	-0.77 ^{+0.28} _{-0.46}
3 839 930	+0.21 ^{+0.01} _{-0.01}	+0.44 ^{+0.09} _{-0.09}	-0.01 ^{+0.24} _{-0.35}	-0.06 ^{+0.25} _{-0.38}	<+1.56	+0.32 ^{+0.13} _{-0.13}	-0.38 ^{+0.10} _{-0.10}	-0.26 ^{+0.13} _{-0.15}	<+0.80	-0.57 ^{+0.23} _{-0.31}
3 865 742	+0.08 ^{+0.02} _{-0.02}	+0.11 ^{+0.22} _{-0.25}	-0.11 ^{+0.43} _{-0.82}	-0.17 ^{+0.46} _{-0.81}	<+2.44	+0.25 ^{+0.35} _{-0.46}	-0.47 ^{+0.47} _{-0.71}	-0.42 ^{+0.34} _{-0.52}	<+1.59	<+0.19
5 941 844	+0.14 ^{+0.01} _{-0.01}	+0.31 ^{+0.15} _{-0.17}	+0.50 ^{+0.38} _{-0.98}	<-0.66	<+1.45	+0.13 ^{+0.11} _{-0.11}	+0.05 ^{+0.09} _{-0.09}	-0.24 ^{+0.17} _{-0.20}	<+0.67	-0.26 ^{+0.09} _{-0.09}
6 462 033	+0.14 ^{+0.02} _{-0.02}	+0.10 ^{+0.19} _{-0.22}	<+0.25	<+0.22	<+1.84	-0.01 ^{+0.25} _{-0.30}	-0.72 ^{+0.34} _{-0.44}	-0.68 ^{+0.27} _{-0.41}	<+1.11	<-0.04
6 780 397	+0.17 ^{+0.01} _{-0.01}	+0.20 ^{+0.19} _{-0.21}	<+0.78	<+0.27	<+1.32	+0.04 ^{+0.11} _{-0.12}	-0.11 ^{+0.11} _{-0.12}	-0.32 ^{+0.19} _{-0.25}	+0.33 ^{+0.31} _{-0.81}	-0.46 ^{+0.14} _{-0.16}
7 760 680	+0.11 ^{+0.01} _{-0.01}	+0.47 ^{+0.22} _{-0.25}	<+1.43	<+0.29	<+1.39	+0.31 ^{+0.10} _{-0.11}	+0.12 ^{+0.09} _{-0.10}	-0.24 ^{+0.27} _{-0.44}	+0.33 ^{+0.24} _{-0.54}	-0.17 ^{+0.10} _{-0.11}
8 057 661	+0.15 ^{+0.02} _{-0.02}	-0.35 ^{+0.12} _{-0.14}	-0.28 ^{+0.16} _{-0.19}	-0.28 ^{+0.18} _{-0.20}	<+2.01	+0.03 ^{+0.25} _{-0.28}	-0.50 ^{+0.18} _{-0.20}	-0.49 ^{+0.20} _{-0.27}	<+1.08	<-0.03
8 087 269	+0.06 ^{+0.02} _{-0.02}	<+0.03	<+1.74	<+1.10	<+2.36	+0.17 ^{+0.32} _{-0.43}	+0.02 ^{+0.37} _{-0.58}	<+0.52	<+1.31	-0.31 ^{+0.38} _{-0.75}
8 381 949	+0.06 ^{+0.01} _{-0.01}	-0.34 ^{+0.14} _{-0.16}	+0.10 ^{+0.16} _{-0.18}	+0.14 ^{+0.15} _{-0.17}	<+1.84	+1.04 ^{+0.17} _{-0.20}	-0.27 ^{+0.24} _{-0.28}	-0.38 ^{+0.24} _{-0.31}	<+1.25	-0.24 ^{+0.37} _{-1.43}
8 459 899	+0.17 ^{+0.01} _{-0.01}	+0.22 ^{+0.08} _{-0.08}	-0.19 ^{+0.18} _{-0.23}	-0.05 ^{+0.10} _{-0.11}	<+1.71	+0.14 ^{+0.11} _{-0.11}	-0.81 ^{+0.07} _{-0.07}	-0.43 ^{+0.08} _{-0.09}	<+0.55	-0.74 ^{+0.14} _{-0.16}
8 714 886	+0.19 ^{+0.01} _{-0.01}	+0.16 ^{+0.09} _{-0.10}	+0.02 ^{+0.20} _{-0.26}	+0.05 ^{+0.23} _{-0.28}	<+1.43	+0.31 ^{+0.14} _{-0.15}	-0.58 ^{+0.16} _{-0.18}	-0.45 ^{+0.15} _{-0.17}	<+0.76	<-0.33
8 766 405	+0.11 ^{+0.01} _{-0.01}	-0.17 ^{+0.20} _{-0.24}	+0.49 ^{+0.30} _{-0.50}	<-0.08	<+1.83	+0.26 ^{+0.13} _{-0.14}	-0.34 ^{+0.14} _{-0.15}	-0.39 ^{+0.18} _{-0.22}	+0.50 ^{+0.33} _{-1.33}	-0.68 ^{+0.17} _{-0.21}
9 964 614	+0.09 ^{+0.01} _{-0.01}	-0.32 ^{+0.12} _{-0.13}	-0.21 ^{+0.19} _{-0.23}	-0.18 ^{+0.19} _{-0.24}	<+1.76	+0.07 ^{+0.19} _{-0.22}	-0.64 ^{+0.21} _{-0.24}	-0.54 ^{+0.17} _{-0.21}	<+1.07	-0.36 ^{+0.36} _{-1.01}
10 285 114	+0.14 ^{+0.01} _{-0.01}	-0.21 ^{+0.25} _{-0.31}	<+0.42	<-0.12	<+1.57	+0.14 ^{+0.17} _{-0.18}	-0.10 ^{+0.16} _{-0.19}	-0.11 ^{+0.19} _{-0.22}	<+0.66	-0.47 ^{+0.28} _{-0.48}
10 536 147	+0.07 ^{+0.01} _{-0.01}	-0.27 ^{+0.18} _{-0.22}	-0.25 ^{+0.27} _{-0.36}	+0.00 ^{+0.21} _{-0.25}	<+2.26	+0.41 ^{+0.26} _{-0.32}	-0.25 ^{+0.31} _{-0.38}	-0.32 ^{+0.26} _{-0.36}	<+1.54	<+0.10
11 360 704	+0.09 ^{+0.01} _{-0.01}	-0.13 ^{+0.18} _{-0.21}	-0.11 ^{+0.35} _{-0.70}	-0.13 ^{+0.39} _{-0.76}	<+2.19	+0.57 ^{+0.18} _{-0.21}	-0.26 ^{+0.20} _{-0.23}	-0.31 ^{+0.18} _{-0.22}	<+1.23	<-0.17
11 971 405	+0.12 ^{+0.01} _{-0.01}	-0.11 ^{+0.16} _{-0.18}	+0.32 ^{+0.28} _{-0.45}	<-0.01	<+1.88	+0.33 ^{+0.11} _{-0.11}	-0.17 ^{+0.09} _{-0.10}	-0.21 ^{+0.11} _{-0.12}	<+0.76	-0.40 ^{+0.12} _{-0.14}
12 258 330	+0.20 ^{+0.01} _{-0.01}	+0.27 ^{+0.10} _{-0.11}	-0.03 ^{+0.38} _{-1.12}	+0.17 ^{+0.30} _{-0.51}	<+1.48	+0.02 ^{+0.13} _{-0.13}	-0.53 ^{+0.14} _{-0.15}	-0.27 ^{+0.13} _{-0.15}	<+0.58	-0.64 ^{+0.22} _{-0.29}